UNIVERSITÄT PADERBORN
Die Universität der Informationsgesellschaft

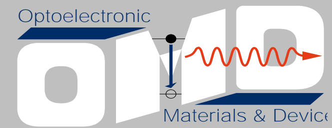

MBE-grown cubic GaN QDs integrated into 2D photonic crystal membranes

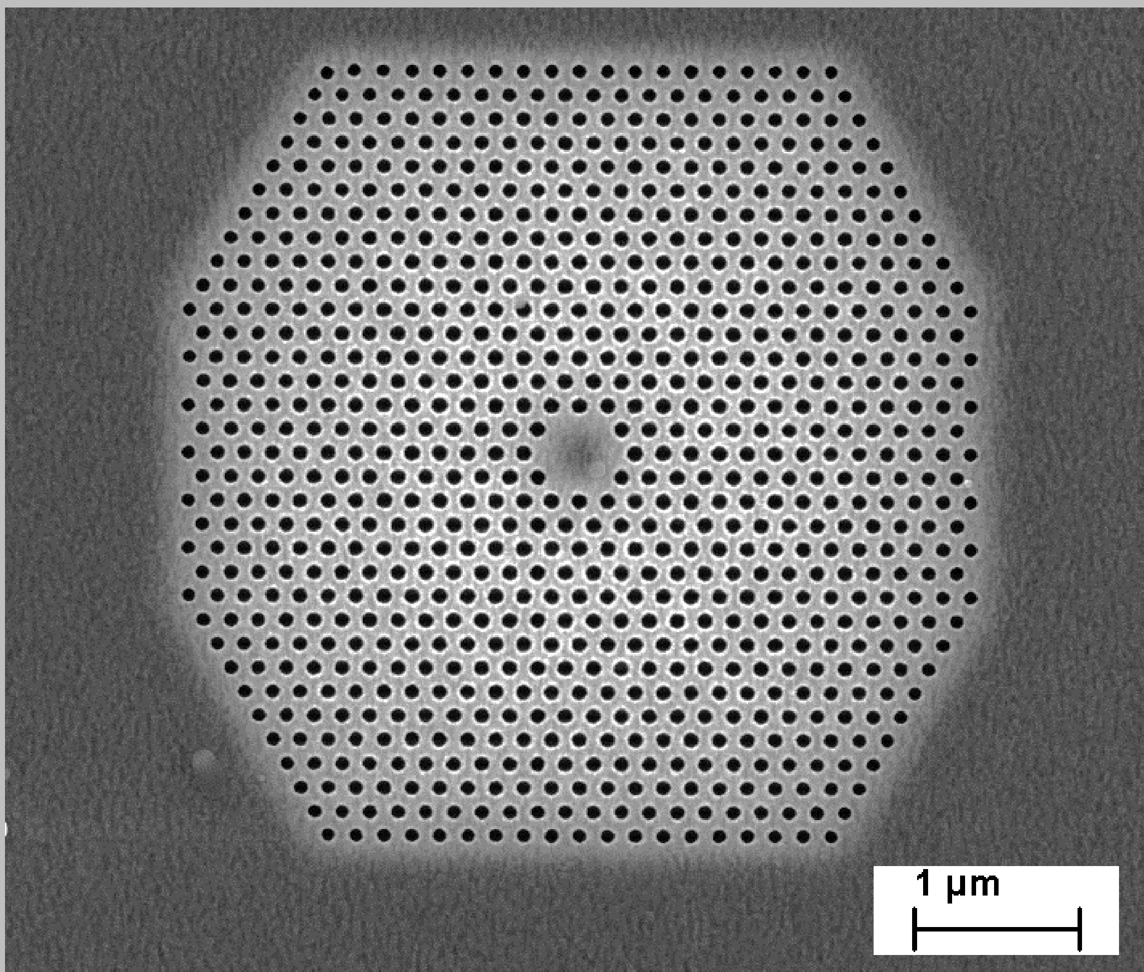

Sarah Blumenthal

MBE-grown cubic GaN QDs integrated into 2D photonic crystal membranes

Dem Department Physik

der Universität Paderborn

zur Erlangung des akademischen Grades eines

Doktors der Naturwissenschaften

-Dr. rer. nat.-

vorgelegte

Dissertation

von

Sarah Blumenthal

Paderborn, Dezember 2018

Erstgutachter: apl. Prof. Dr. Donat. J. As

Zweitgutachter: Prof. Dr. Cedrik Meier

Parts of this work have already been published in journals and conference proceedings.

Publications are listed on page XXXIX.

Abstract

Cubic group III-nitrides attracted much attention in the development of optical and quantum optical devices operating in the UV spectral range. Especially the implementation of quantum dots (QD) in optoelectronic devices is in the focus of interest. In contrast to hexagonal nitrides, cubic nitrides have the great advantage that there are no internal polarization fields that can lead to a reduced recombination probability.

In this work, cubic GaN (c-GaN) QDs are embedded in a cubic AlN (c-AlN) matrix realized by plasma-assisted molecular beam epitaxy on 3C-SiC substrates on top of Si (001). Single QD layers are examined structurally and optically showing high photoluminescence (PL) intensities and smooth surfaces, which are comparable to the roughness of the substrate. The high PL intensities originate from a superposition of Gaussian shaped emission bands of many individual QDs. Additionally, the influence of a second QD layer or several QD layers is observed by different sample series. Transmission electron microscopy images show a vertical stacking of the QDs if the spacer layer is thin and no stacking faults are present. In the vicinity of stacking faults the QDs are threated along the [111] direction of the stacking faults. Furthermore, based on photoluminescence measurements of two QD layers stacked on each other possessing different QD sizes, it can be assumed that the QDs are also coupled electrically. This could be investigated by varying the thickness of the spacer layer. With a thick spacer layer of 20 nm, a peak could be assigned to the lower and upper QDs in the emission spectrum. At a thin spacer layer of 2 nm only one peak could be observed. This can be assigned to the upper layer. If the number of stacked QD layers is increased, photoluminescence measurements show an increase in intensity with increasing number of stacked layers. The reason for such an increase is that with increasing number of layers an increase of excited QDs occurs, too. A blueshift of emission energy is also observable. The increase of emission energy with increasing number of stacked layers is based on a decrease in QD height of one or two monolayers.

Two-dimensional (2D) photonic crystal (PC) membranes are successfully realized from the previously described QD samples. A triangular lattice of air holes is implemented by electron-beam lithography and multiple steps of dry and wet etching. Thus, air holes diameters of about 110 nm are obtained. Different cavity designs are realized including L3 and H1 cavities. The optical as well as the structural properties of the PC membranes are investigated by scanning electron microscopy and μ-PL measurements. On that basis, high quality factors of 4400 for the H1 cavity and 5000 for the fundamental modes of the L3 cavity are estimated. Simulations of the mode energies show no significant differences to the experimentally determined mode energies.

Kurzfassung

Kubische Gruppe III-Nitride gewinnen für optische und quantenoptische Anwendungen im spektralen UV-Bereich immer mehr an Bedeutung. Vor allem die Implementierung von Quantenpunkten in optoelektronische Bauelemente steht im Fokus des Interesses. Kubische Nitride haben den großen Vorteil, dass keine internen Polarisationsfelder existieren, die zu einer reduzierten Rekombinationswahrscheinlichkeit führen können. Dies steht im Gegensatz zu der hexagonalen Phase.

In dieser Arbeit wurden kubische GaN (c-GaN) Quantenpunkte in eine kubische AlN (c-AlN) Matrix eingebettet. Die Herstellung erfolgte mittels plasmaunterstützer Molekularstrahlepiaxie auf 3C-SiC Substraten, die auf Si (001) Substraten abgeschieden wurden. Einzelne Quantenpunktlagen sind sowohl strukturell als auch optisch untersucht worden. Diese Proben weisen eine glatte Oberfläche, die vergleichbar mit der Rauigkeit des Substrates ist, und hohe Photolumineszenzintensitäten auf. Diese hohen Intensitäten existieren auf Grund einer Superposition von vielen gaußförmigen Emissionen einzelner Quantenpunkte. Im Rahmen dieser Arbeit ist außerdem der Einfluss einer zweiten und einer Vielzahl von gestapelten Quantenpunktlagen untersucht worden. Dabei zeigten Transmissionselektronenmikroskop-Aufnahmen vertikal gestapelte Quantenpunkte für den Fall, dass die Zwischenschicht dünn genug und keine Stapelfehler vorhanden sind. Wenn Stapelfehler vorliegen, sind die Quantenpunkte in [111]-Richtung entlang dieser Stapelfehler angeordnet. Aus den Photolumineszenz-Messungen von zwei übereinander gestapelten Quantenpunkten unterschiedlicher Größe kann außerdem geschlossen werden, dass eine elektrische Kopplung zwischen den Quantenpunkten auftritt, wenn die Zwischenschicht dünn ist. Dies konnte anhand einer Variation der Dicke der Zwischenschicht von 2 und 20 nm untersucht werden. Bei einer dicken Zwischenschicht ist jeweils ein Emissionspeak für die unteren und die oberen Quantenpunkte zu sehen. Für die die dünne Zwischenschicht konnte nur noch ein Emissionspeak beobachtet werden, der der oberen Lage Quantenpunkte zugeordnet werden kann. Erhöht man die Anzahl der übereinander gestapelten Quantenpunktlagen, zeigen Photolumineszenz-Messungen eine Erhöhung der Intensität mit ansteigender Zahl an Quantenpunktlagen. Dies war zu erwarten, da die Gesamtanzahl der Quantenpunkte ebenfalls zunimmt. Außerdem ist eine Blauverschiebung der Emissionsenergie zu erkennen. Die Zunahme der Emissionsenergie mit ansteigender Anzahl an Quantenpunktlagen ist mit einer Abnahme der Quantenpunkthöhe um ein bis zwei Monolagen zu erklären.

Zwei-Dimensionale photonische Kristall (PC)-Membranen sind erfolgreich aus den zuvor beschriebenen Quantenpunktproben hergestellt worden. Dabei wurde ein trianguläres Gitter aus Luftlöchern implementiert, mit Luftlöcher-Durchmessern von

ungefähr 110 nm. Es wurden Elektronenstrahllithographie und mehrere trocken- und nasschemische Ätzschritte umgesetzt um verschiedene Kavitäten zu realisieren, wie zum Beispiel L3 und H1 Kavitäten. Sowohl die optischen als auch die elektrischen Eigenschaften der PC-Membranen wurden mittels Rasterelektronenmikroskopie und μ-PL Messungen untersucht. Dabei konnten hohe Gütefaktoren von 4400 für die H1 Kavität und 5000 für die fundamentale Mode der L3 Kavität ermittelt werden. Simulationen dieser Modenenergien zeigen keine signifikanten Unterschiede zu den experimentell ermittelten Ergebnissen.

Table of Contents

Abstract .... **I**

Kurzfassung .... **II**

Table of Contents .... **IV**

1 Introduction **1**

1.1 Motivation 1

2 Fundamentals **3**

2.1 Physical Properties of Cubic Group III-Nitrides 3

2.2 Quantum Dots 5

2.3 Photonic Crystals 8

2.3.1 Electrodynamic in Periodic Dielectrics 9

2.3.2 Defects in Photonic Crystals 13

2.3.3 Photonic Crystal Membranes 14

2.3.4 Optimization of the Quality Factor 16

2.3.5 QDs embedded in PCs 17

3 Experimental **19**

3.1 Growth 19

3.1.1 Molecular Beam Epitaxy 19

3.1.2 Reflection High-Energy Electron Diffraction 24

3.2 Characterization 26

3.2.1 Atomic Force Microscopy 26

3.2.2 High-Resolution X-Ray Diffraction 28

3.2.3 Photoluminescence Spectroscopy 29

3.2.4 Electron Microscopy 32

3.2.4.1 Scanning Electron Microscopy 32

3.2.4.2 Transmission Electron Microscopy 33

4 Growth of c-AlN Epilayers and c-GaN QDs **36**

4.1 Sample Preparation 36

4.2 Thick c-AlN Layers 37

4.3 Single QD Layers 42

4.4 Asymmetric QD Pair 48

4.5 Stacked QD Layers 51

4.6 Summary of the Growth of c-AlN and c-GaN 64

5 Nextnano++ Simulations of c-GaN QDs **65**

5.1 Transition Energy of QDs 67

5.2 Mechanical Coupling of QD Pairs 70

5.3 Summary of nextnano++ Simulations 71

6 Photonic Crystal Membranes ... 72
6.1 Fabrication of PC Membranes ... 73
6.2 CST-Simulation of Modes ... 80
6.3 µ-PL Measurements of PC Membranes ... 86
6.4 Summary of PC Membranes ... 89

7 Summary ... 90

8 Outlook ... 92

9 Appendix ... VII
9.1 List of Figures ... VII
9.2 List of Tables ... XI
9.3 Bibliography ... XII
9.4 List of Abbreviations ... XVII
9.5 Temperature Calibration ... XIX
9.6 Optimized PC Membranes ... XX
9.7 Parameter List ... XXI
9.8 Nextnano++ Script ... XXII
9.9 List of Samples ... XXX

10 List of Publications ... XXXIX

11 Conference Contributions ... XL

12 Cooperation Partners ... XLII

13 Acknowledgment ... XLIII

14 Erklärung der Selbstständigkeit ... XLIV

1 Introduction

1.1 Motivation

Group III-nitrides are in the focus of interest due to their excellent properties for optical and quantum optical devices which operate in the UV spectral range. Especially QDs are used for many applications like QD-lasers, single-photon-emitters and QD detectors. The stacking of QDs is an appropriate way to increase the number of total QDs in the active region. Quantum dot lasers have been already realized containing stacked QDs for other material systems. For example, Saito et al. [1] presented a vertical-cavity surface-emitting laser consisting of ten layers of InGaAs quantum dots.

Due to the stacking of QDs with a thin spacer layer a structural coupling of the dots occurs [2], [3]. Local strain fields originated by the subjacent QD layer generate preferential nucleation sites for the QDs in the subsequent layer. The result is a vertical alignment of the QDs. In addition to the influence on the structural properties, electronic properties may change due to the stacking. As reasons could be mentioned a change of strain [4] and an electronic coupling between the QD layers [2,5]. In the InAs system these effects resulted in a redshift in PL emission energy in most stacking experiments [2,5]. InGaAs QD lasers with multi-stacked QD layers demonstrated laser oscillations from QDs at room temperature [6].

Stacked hexagonal QDs have already been realized in recent years indicating an increase in room temperature photoluminescence intensity with increasing number of stacked layers [7]. However, the hexagonal field has the disadvantage that piezoelectric and polarization fields lead to a reduced recombination probability [8]. The fields originate from the atom arrangement in the crystal.

This may be overcome by using zinc blende growth mode, where no polarization fields in (001) direction exist [9]. This growth direction is not well investigated at the moment. The growth of a single c-GaN QD layer was shown by Schupp et al. [10] for Droplet Epitaxy QDs and by Bürger et al. [11] for SK QDs. With the latter, single-photon emission was demonstrated [12]. The QDs show radiative lifetimes about one order of magnitude shorter compared to hexagonal, polar GaN QDs, which are emitting at the same energy [13].

The combination of QDs and photonic crystals (PCs) can lead to an increase of the optical gain and thus to lasing of the QDs. The QDs are embedded in the active layer. They can strongly couple with the optical field. Due to the minimization of most optoelectronic components, the development of nanocavity laser is an important element of the current research. A single layer of h-GaN QDs has already been embedded in a PC membrane by N. Li [14]. This membrane showed five times higher PL intensities compared to the active

layer without structuring. Another possibility is to embed stacked QDs in this PC membrane. By the fact that QDs normally achieve only a low gain, since on the one hand much less emitting material is available and on the other hand due to the inhomogeneous emission broadening, a large number of QDs, realized by several layers of QDs, are a first solution approach [15].

Photonic crystals are first shown by Yablanovitch [16]. His idea was to create a material showing similar behaviors as electrons in semiconductors. The periodic structured material in the PC affects the light in a similar way as the atomic potential the electrons. This analogy can mainly be explained by the analogism of the Schrödinger's equation for electronic wave functions and the Maxwell's equations for electromagnetic waves. Scattering of dielectric atoms lead to an optical band structure with optical band gaps in the range of the wavelength of the lattice constant.

Cubic AlN/c-GaN Microdisks [17] and 1D waveguide structures [18] are already realized containing QDs as the active medium. The whispering gallery modes of the microdisks show first transitions to the lasing regime. The waveguide structures still exhibit high losses, which are probably due to light that is not guided through the waveguide but scattered at the tethers. However, realizing PCs with III-nitride materials involve technological difficulties. Due to the small wavelength of the material, the dimensions of the PC must be small, too. Additionally, standard wet-chemical etching steps, normally used for the underetching of the active layer, are not possible.

The objective of this research is to realize a PC with c-GaN QDs incorporated in the active layer. For this purpose, firstly the fundamental knowledge about group III-nitrides, quantum dots and photonic crystals, with focus on photonic crystal membranes, are described in chapter 2.

Subsequently, chapter 3 depicts the experimental basics. After describing the MBE growth process, the structuring methods for the fabrication of the PC membranes are explained in detail. Finally the characterization methods used for the characterization of the QD ensemble as well as for the PC membranes are enlightened.

Chapter 4 describes the growth of thick c-AlN epilayers and the incorporation of c-GaN QDs into a c-AlN matrix. Additionally, stacked QD layers of two and several layers are realized and structurally and optically characterized. To complete the understanding of the QD layers, nextnano++ simulations are done in chapter 5.

The implementation of PC membranes is represented in chapter 6. At first the fabrication steps are explained in detail then simulation and experimental results of the PC membranes are shown.

2 Fundamentals

This chapter discusses the fundamental physical properties of cubic group III nitrides. Special attention is given to 3C-SiC, cubic gallium nitride (c-GaN) as well as cubic aluminium nitride (c-AlN). Then the main subject is low dimensional structures with a special focus on QDs, followed by the basics of photonic crystal membranes.

2.1 Physical Properties of Cubic Group III-Nitrides

This work investigates cubic group III-nitrides, more specifically the growth of c-AlN and c-GaN. Cubic group III-nitrides have the great advantage of covering a wide range of wavelengths (360 nm -2.1 µm). This makes them suitable for devices from the green to the UV spectral range. They also have high thermal and mechanical stability, which makes them a good base many high-power devices.

Group III-nitrides exist in two modifications, the hexagonal wurtzite structure and the metastable cubic zinc blende structure. The crystal structure of both, using the example of GaN, is shown schematically in Figure 2-1 [19]. Green spheres indicate Ga atoms and the smaller blue spheres represent N atoms. The zinc blende structure, shown in Figure 2-1 (b), consists of two fcc-sublattices being displaced by each other by ¼ of the distance along the diagonal of the cube in the [111] direction with a stacking sequence of ABCABC. Whereas the wurtzite lattice shows a stacking sequence of the (0001) planes of ABAB etc. in the [0001] c-axis (Figure 2-1 (a)).

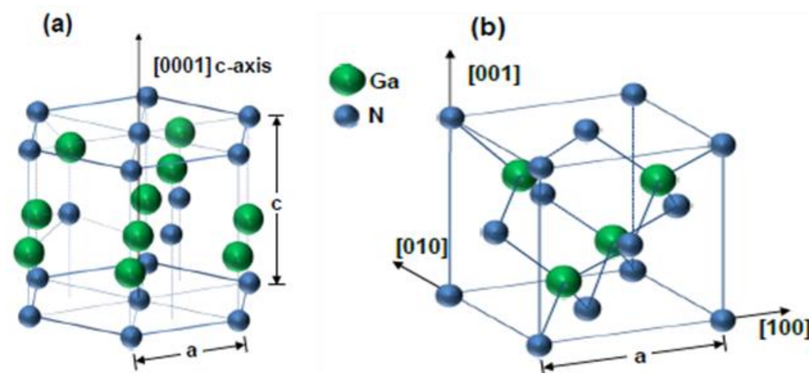

Figure 2-1: Crystal structure of (a) h-GaN and (b) c-GaN. Green spheres indicate Ga atoms and blue spheres N atoms.

The hexagonal phase has a big disadvantage. Referring to low dimensional structures, like quantum wells or quantum dots, a Quantum Confined Stark Effect (QCSE) occurs, which is caused by an internal field. More precisely, large piezoelectric polarization fields

occur along the c-axis and spontaneous polarization takes place at hetero-interfaces. This field leads to a spatial separation of the wave functions of electron and holes (see Figure 2-2 (b)). Due to the spatially separated wave functions a reduced recombination probability is expected [8]. The growth of the metastable zinc blende phase can reduce these internal fields so that no spontaneous polarization fields in (001) growth direction exist [9]. The wave functions of electrons and holes are no longer spatially separated. As a result, a higher recombination probability is expected using cubic group III-nitrides. Furthermore, theoretical calculations show that piezoelectric polarizations fields also do not exist in the (001) direction [20].

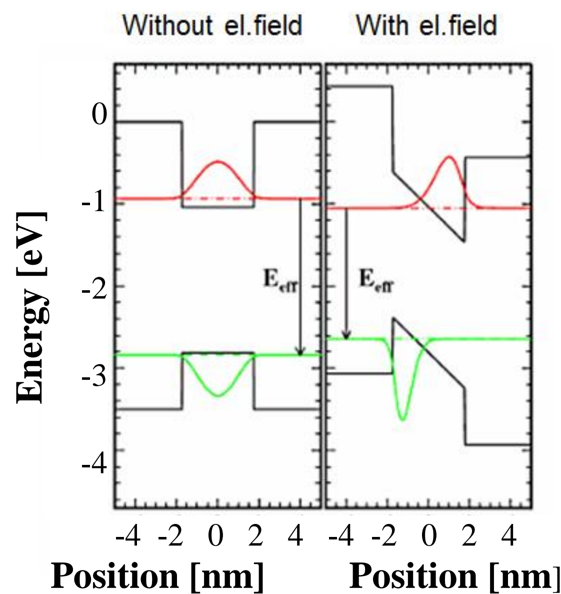

Figure 2-2: Schematic illustration of the band diagram for the cubic phase without internal electric field and for the hexagonal phase, which has an internal polarization field. The probability density for electrons (red) and holes (green) is sketched.

Further advantages of cubic GaN are the wide band gap of 3.23 eV [21] and the high exciton binding energy, which is about 26 meV [20], so it is suitable for room temperature applications. Additionally, it is a promising candidate for high power devices, due to the large thermal stability and conductivity.

2.2 Quantum Dots

Quantum dots (QDs) have opened many opportunities for physical research and technological applications, including quantum cryptography, quantum computing and optoelectronic devices, such as quantum dot lasers. Mainly, due to the drastic change of the electronic properties compared to systems with higher dimensionality they are in the focus of current research topics. Arakawa and Sakaki became one of the first using QDs in optoelectronic applications [22].

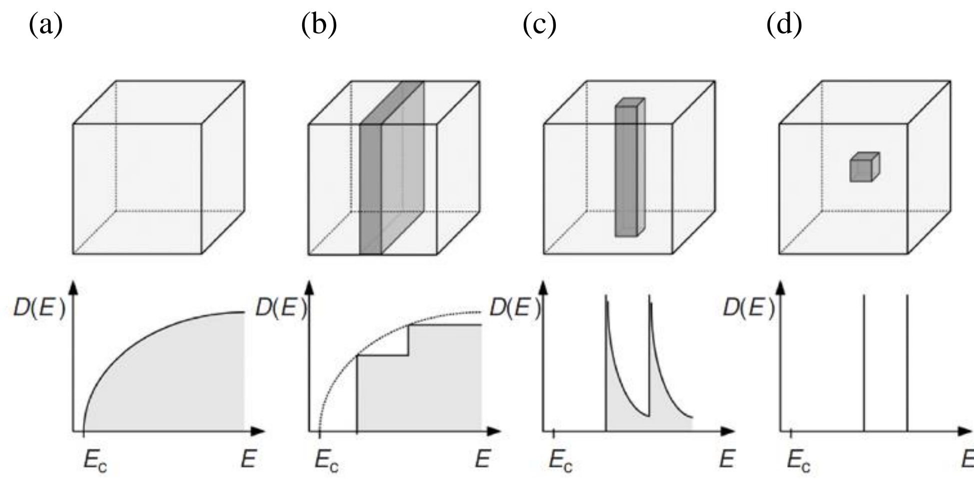

Figure 2-3: Density of states for (a) bulk, (b) quantum well (one-dimensional confinement), (c) quantum wire (two-dimensional confinement) and (d) quantum dot (three-dimensional confinement) [23].

Figure 2-3 shows a schematic of the density of states D(E) (DOS) of free electrons for different dimensionalities, going from bulk (three-dimensional (3D)) to QDs (zero-dimensional (0D)). The density of states per energy interval is the derivative of the states N with respect to the energy E:

$$D(E) = \frac{dN}{dE}. \qquad (2\text{-}1)$$

In a bulk semiconductor (3D), as shown in Figure 2-3 (a), the DOS is proportional to $\sqrt{E}$. Considering one dimension less, a two-dimensional (2D) electron gas is obtained, resulting in a step function with various discrete energy levels of constant energies (see Figure 2-3 (b)), which is described by the Heaviside-function Θ. In a one-dimensional (1D) quantum wire, the DOS shows a reciprocal dependence of the

root $(\sqrt{E})^{-1}$ as shown in Figure 2-3 (c). Whereas in a quantum dot (0D) the mobility of the electrons is confined in all spatial directions (see Figure 2-3 (d)).

In reality, the spectrum of a single QD shows a Lorentz-shaped curve. The width of the spectrum depends on the damping factor of the harmonic oscillator. Figure 2-4 depicts µ-PL spectra of single c-GaN QDs at 4 K [24]. Mesas are etched with a diameter of 200 to 500 nm to reduce the total number of QDs. The linewidth of those QDs is 500 ± 50 µeV with the resolution at the limit of the setup. The radiative lifetime of the QDs is shorter than 305 ps (at 3.9 eV). The energy levels, which are allowed, are discrete and clearly separated. So the density of states correlates with a series of atom-like delta functions. QDs are therefore also called "artificial" atoms [25]. This atom-like character provides many advantages. An important parameter is the exciton Bohr radius (a_0), which describes the size of the excitons (electron-hole-pair) in a semiconductor. To see confinement effects, the particle size must be smaller than the exciton Bohr radius. Common sizes for the Bohr radius are from 2 to 50 nm, depending on the material [26].

The QD ensemble consists of many QDs, varying in size, shape and tension. Thus leads to an inhomogeneous line broadening. The envelope of the spectral lines is a Gaussian function. The QD ensemble of c-GaN QDs is also shown in Figure 2-4 (grey marked area).

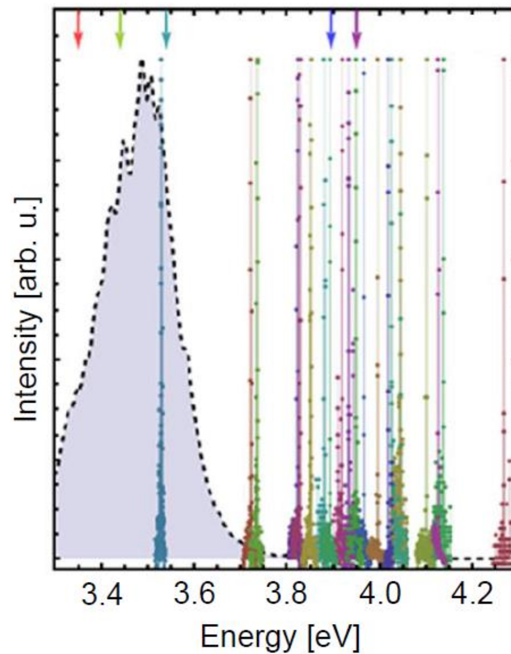

Figure 2-4: µ-PL spectra of single c-GaN QDs at a temperature of 4 K. The grey area shows the emission of the QD ensemble [24].

Since the discovery of the blue GaN Light Emitting Diode (LED), this material is of growing interest. As already described in chapter 2.1, GaN exists in two different crystal structures. Consequently, the behavior of the QDs is different, too. Fonoberov and Balandin [20] did numerical calculations of the internal fields of QDs. The results of their work are described in the following section. The numerical calculations were realized for both, hexagonal and cubic GaN QDs embedded in a hexagonal and cubic AlN matrix, respectively. They used a combination of finite difference and finite element methods to determine strain, piezoelectric and Coulomb fields as well as the electron and hole states.

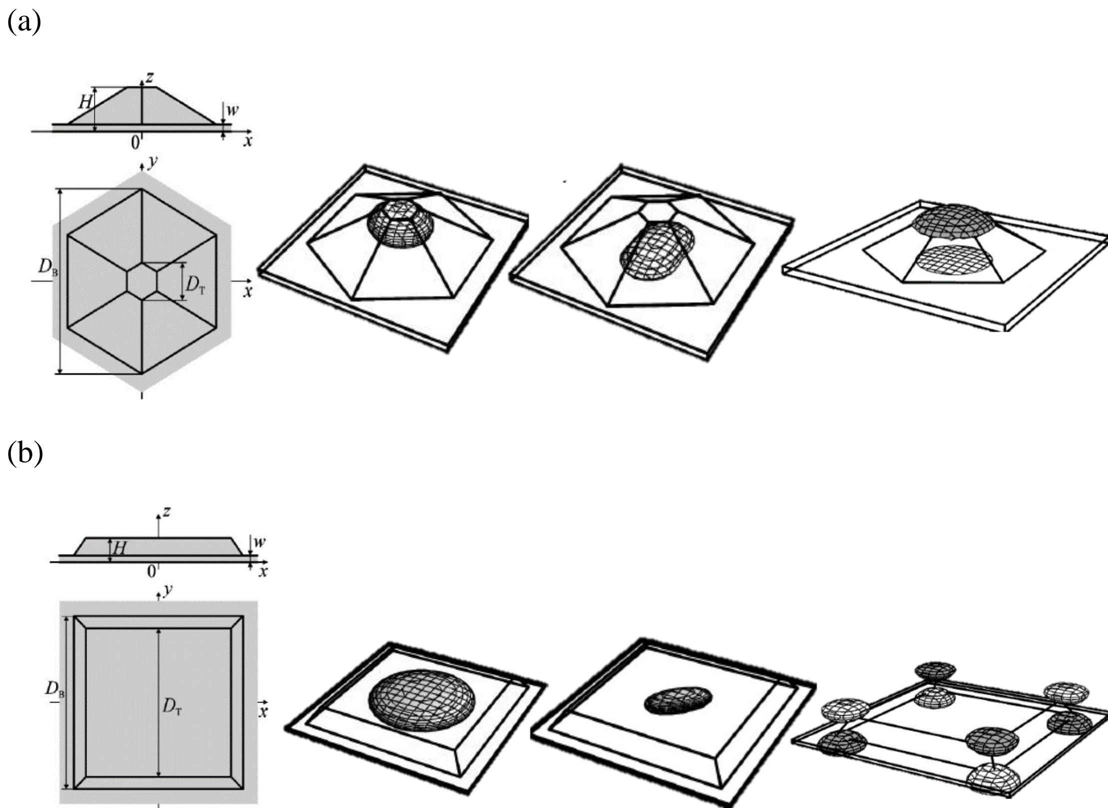

Figure 2-5: Shape (left), isosurfaces of the probability density $|\psi_e|^2 = \rho$ for the lowest electron and hole state (middle) and the piezoelectric potential of a QD with 3 nm height (right) for (a) h-GaN/AlN and (b) c-GaN/AlN [20].

The shape of both QDs used for the simulations is shown on the left side of Figure 2-5. For the hexagonal QD a truncated hexagonal pyramid on a wetting layer was used, whereas for the cubic QD, a truncated pyramid with a square basis was applied. The wetting layer is w = 0.5 nm and the height of the QDs is h = 3 nm. The piezoelectric potential (see Figure 2-5 (right)) of the hexagonal QDs is about ten times larger than that of the cubic QDs. Furthermore, the maximum of the potential of the hexagonal QD is in

the center and near to the top and bottom, which results in tilted conduction- and valence-band edges along the z-axis. Therefore it is energetically more favorable for electrons and holes to be located at the top and at the bottom (see Figure 2-5 (middle)). The maxima of the potential of the cubic QD are on the corners of the QD, consequently the influence on charge carriers is less.

2.3 Photonic Crystals

After the closer examination of multidimensional photonic crystals by Yablonovitch [16], photonic crystals (PCs) became of great interest mainly in the fields of quantum computing and quantum cryptography [27]. Fundamentally, a photonic crystal is an optical resonator, which confines light. The resonator is realized by a periodic arrangement of holes in a crystal. Due to the alternating refractive indices or dielectric functions of the material and the air holes, standing waves build up. As a result of constructive interference an excessive increase of the electromagnetic field occurs. The propagation of electromagnetic waves is influenced in a way comparable to the propagation of electric waves in a crystal. There the potentials of the atomic cores are arranged periodically. The distance of air holes in the PC is in the order of the optical wavelength of the material $\left(\frac{\lambda}{n}\right)$. In analogy to the crystal, a photonic band gap occurs for light with specific wavelengths and propagation directions.

Photonic crystals in different dimensions are already realized. Bragg-mirrors are an example for a 1D PC. The alternating refractive indices of two different materials lead to the creation of a photonic band gap (PBG). Because of reflections of multiple interferences in multilayer systems, 1D PC show a small absorption in comparison to metallic mirrors. In this work only 2D PCs are considered. That means the crystal is realized in two spatial directions (x and y) by an alternating sequence of air and a material of much larger refractive index. In the third direction (z) the crystal is homogeneous. The realization of a PBG in a 2D PC is much more complicated, compared to a 1D PC, because the band gap for all crystal directions as well as for all polarizations has to overlap.

2.3.1 Electrodynamic in Periodic Dielectrics

The following section is based on [28] and describes the physical principles of PCs. Basically, multiple scattering occurs at a periodic lattice in the case that an electromagnetic wave hits a PC. This scattering mechanism can be described by the Maxwell equations:

$$\nabla \cdot B = 0 \qquad (2\text{-}2)$$

$$\nabla \times H = \frac{\delta D}{\delta t} + j \qquad (2\text{-}3)$$

$$\nabla \cdot D = \rho \qquad (2\text{-}4)$$

$$\nabla \times E = -\frac{\delta B}{\delta t}. \qquad (2\text{-}5)$$

with B the magnetic induction, H the magnetic field strength, D the dielectric displacement, E the electric field strength, j the electric current density and ρ the electric charge density. Equations (2-3) and (2-5) describe the coupling of the E field and the B field with the help of the time derivative of the Faraday's induction law and the law of Ampère. These laws declare that the electric field generates a magnetic vortex field and vice versa. The law of Gauss (equations (2-2) and (2-4)) says that magnetic fields are source free and the source of the electric field are electric charges.

If only dielectric structures are considered, so that no free charges occur, $\rho = 0$ and $j = 0$ is valid. Additionally, in non-magnetic materials ($\mu = 0$) the following formulas apply:

$$B(r) = \mu_0 H(r) \qquad (2\text{-}6)$$

$$D(r) = \varepsilon_0\, \varepsilon(r) E(r), \qquad (2\text{-}7)$$

where μ_0 is the permeability and ε_0 is the dielectric constant. Applying (2-6) and (2-7) to the Maxwell equations and considering a harmonic time response

$$H(r,t) = H(r)\, e^{i\omega t} \qquad (2\text{-}8)$$

$$E(r,t) = E(r)\, e^{i\omega t}, \qquad (2\text{-}9)$$

formulas (2-3) and (2-5) can be transformed to the vectorial Helmholtz equation, also known as the master equation,

$$\nabla\times\left(\frac{1}{\varepsilon(r)}\nabla\times H(r)\right)=\left(\frac{\omega}{c}\right)^2 H(r), \qquad (2\text{-}10)$$

with c the speed of light.

In line with the time-independent Schrödinger equation, it is possible to define the following eigenvalue equation for the harmonic modes H(r):

$$\Theta\, H(r)=\left(\frac{\omega}{c}\right)^2 H(r) \qquad (2\text{-}11)$$

with

$$\Theta=\nabla\times\left(\frac{1}{\varepsilon(r)}\nabla\times H(r)\right) \qquad (2\text{-}12).$$

In this work a 2D PC membrane is considered with a hexagonal lattice of air holes, which is depicted with two linearly independent vectors a_1 and a_2 in the x-y-plane and the lattice translation vector of the unit cell *R*.

The dielectric function has a discrete translation symmetry

$$\varepsilon(r)=\varepsilon(r+R). \qquad (2\text{-}13)$$

The electromagnetic modes of the photonic crystal are Bloch states

$$H_k(r)=e^{i(k\cdot r)}\, u_k(r), \qquad (2\text{-}14)$$

with the periodic Bloch function $u_k(r)=u_k(r+R)$ with k the wave vector. The Bloch state with wave vector k_y and the one with the wave vector $k_y + g$ are identical, whereby the reciprocal lattice constant is defined as $g=\frac{2\pi}{R}$. Therefore, the mode frequencies must also be periodic and it suffices if we consider that k_y only exists in the range of $\left[-\frac{g}{2},\frac{g}{2}\right]$ [29].

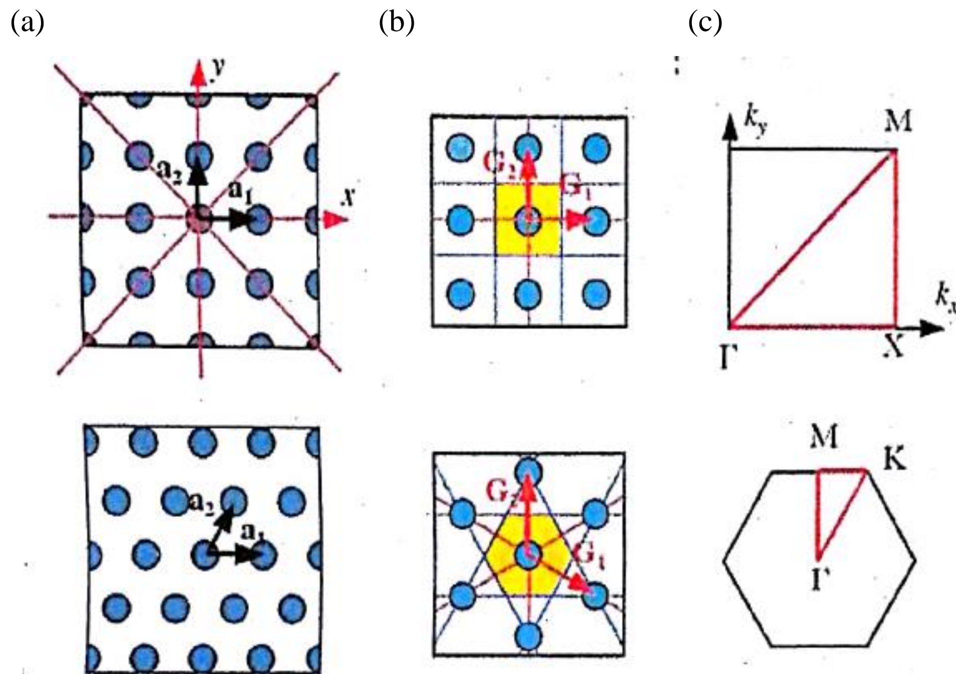

Figure 2-6: (a) Schematic illustration of the 2D air hole lattice of a square and a hexagonal lattice with lattice vectors a_1 and a_2, (b) reciprocal lattice with reciprocal lattice vectors G_1 and G_2 and the first Brillouin Zone (yellow), (c) first Brillouin Zone with irreducible BZ and high symmetry points Γ, M and K [28].

The translation lattice is described by the reciprocal lattice vector G, which defines the reciprocal space. The smallest region in the reciprocal space is called the Brillouin Zone (BZ). A k-vector, which is located beyond the first BZ can be compared to a k-vector in the zone, which has the same physical results. Due to the rotational symmetry it is possible to restrict the BZ even more. Figure 2-6 depicts a schematic illustration of two different 2D PCs. The upper part shows a square lattice of air holes, whereas the lower part shows a hexagonal lattice. Accordingly, the first BZ is also square or hexagonal. The BZs are highlighted yellow and the reciprocal lattice vectors are displayed (Figure 2-6 (b)). Figure 2-6 (c) shows the first BZ in more detail. The red line represents the irreducible BZ.

Capital letters mark high symmetry points Γ, K and M. At the corners of the BZ a split-up of the band is possible. For a unitary material the dispersion relation is linear. If we consider two materials with different dielectric constants ($\varepsilon_1 < \varepsilon_2$) that are arranged alternately (see Figure 6-2), modes in the optically thicker medium are more preferable. This leads to decreased energy or frequency. Whereas in the optically thinner medium an increased energy or frequency results. Therefore, a band results where the light propagation perpendicular to the layer structure is forbidden. This is called the PBG.

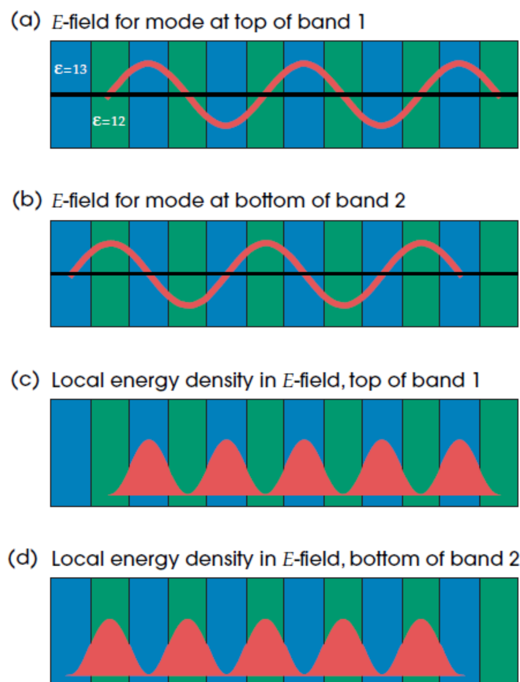

Figure 2-7: Schematic illustration of the field distribution in a photonic crystal from [28]. (a) and (b) show the E-fields and (c) and (d) the intensities of the highest frequency of the first band or the lowest frequency of the second band. Blue indicates the region with higher dielectric constant.

Characteristically, the electromagnetic vector fields are decoupled, so that two different polarization directions occur. On the one hand, transversal magnetic (TM) waves are formed with the electric field in z-direction and the magnetic field in plane (x-y-direction) and on the other hand transversal electric (TE) waves occur showing the electric field in plane and the magnetic field in z-direction.

The size of the PBG depends on different parameters. Conditions required for a high PBGs are a high refractive index, the geometry of the PC and the volume ratio of both materials.

2.3.2 Defects in Photonic Crystals

If defects in PCs are realized, the Bloch theorem (3-5) is no longer applicable and localized eigenmodes with eigenfrequencies in the band gap arise due to the symmetry braking. Thus, allowed states are possible in the PBG. These modes, with a frequency in the band gap, are bound to the defects. A wave, located in this band gap, cannot leave it lateral, because outside of the defect the propagation is suppressed due to the alternating dielectric constants. In a 2D PC the defect is realized by omitting one or various air holes in the center of the crystal. In Figure 2-8 typical cavities are shown. H1 is the easiest cavity with one missing hole in the center of the cavity. Omitting the surrounding holes radially it forms the H7 cavity, omitting one more circle the H19 cavity is realized. The result is nearly a circular defect, where the light can build whispering gallery modes, which is comparable to a mikrodisk [30]. The other possibility for the design of a defect is to omit holes in a row in the center of the crystal. One way is a L3 cavity with three missing holes in a row in the center. Omitting even more holes leads to the L5 and L7 cavity. In the linear defects, modes exist that are comparable to the macroscopic resonator. However, Akahane et al. [31] and Choi et al. [32] presented 2D modes, too.

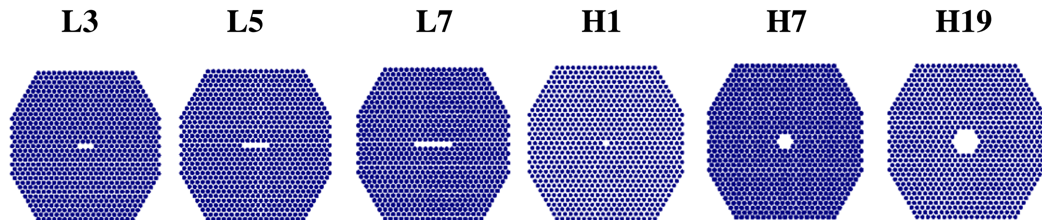

Figure 2-8: Schematic representation of typical cavity sizes. The L-cavities consist of missing holes in a row and the H-cavities of missing holes radially around the center.

If we consider an ideal cavity, losses would not exist. Deviation from this ideal character is described by the Q factor. Which is the ratio of the wavelength λ and the full width half maximum (FWHM) Δλ:

$$Q = \frac{\lambda}{\Delta\lambda}. \qquad (2\text{-}15)$$

The mode volume is the volume occupied by the confined optical mode. Large resonators have a large mode volume and a relatively low photon density in the cavity. Photonic crystals, compared to other microcavities, “can provide extremely small mode volumes and large theoretical Q values” [33].

2.3.3 Photonic Crystal Membranes

In this work a photonic crystal membrane, also called air bridge-type, is used. This membrane, also called slab, minimizes the escape of light from the slab in the surrounding media if the refractive index of the slab is much larger than the surrounding media, which reflects the light at the interface. The PC slab is used, because it corresponds almost to a 3D PC. In contrast to a 3D PC, a 2D PC membrane is much easier to fabricate with state-of-the-art semiconductor microfabrication techniques [34].

The basis vectors in real space for a hexagonal lattice of air holes (see Figure 2-6 (a)) are defined as follows

$$a_1=\left(\frac{\sqrt{3}}{2},\ \frac{1}{2}\right)a \tag{2-16}$$

$$a_2=\left(\frac{\sqrt{3}}{2},-\frac{1}{2}\right)\ a, \tag{2-17}$$

with $|a_1|=|a_2|=a$.

The basis vectors of the reciprocal lattice (see Figure 2-6 (b)) are

$$b_1=\left(\frac{1}{2},\ \frac{\sqrt{3}}{2}\right)\frac{4\pi}{\sqrt{3}a} \tag{2-18}$$

$$b_2=\left(\frac{1}{2},-\frac{\sqrt{3}}{2}\right)\frac{4\pi}{\sqrt{3}a} \tag{2-19}$$

with $|b_1|=|b_2|=\frac{4\pi}{\sqrt{3}a}$.

In a hexagonal lattice small regions of a material with large refractive index is surrounded by large areas of air, so that the air-filling-factor f_{air} is small. It can be determined with simple geometrical considerations:

$$f_{air}=\frac{2\pi}{\sqrt{3}}\ \left(\frac{r}{a}\right)^2. \tag{2-20}$$

The design of a hexagonal lattice of air holes is chosen, because a larger PBG is expected, compared to a square lattice, for example. Air-filling-factors of 30-40 % are used for technical applications, because of the small wall thickness for higher air-filling-factors.

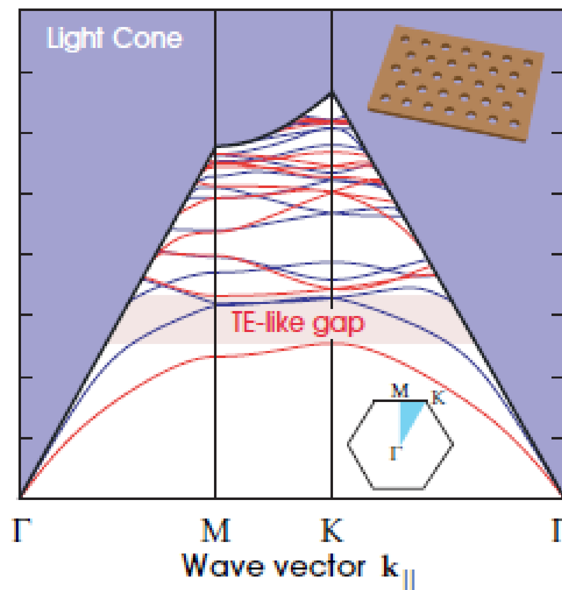

Figure 2-9: Band diagram for photonic crystal slab. The blue part (light cone) shows the extended modes propagating in air, below the cone the guided modes are located. The blue bands show the TM-like and the red bands, the TE-like bands. The first BZ is shown in the inset with the irreducible BZ, marked blue [28].

It should be noted, that from now on TE and TM polarized modes are called TM-like and TE-like modes. The modes are no longer TE- or TM-modes in any case. The electric or magnetic field is purely transverse only in the x-y-plane. That means that the in-plane wave vector is conserved, but the wave vector in z-direction is not. That leads to a coupling of the band to the mode continuum of the free space. Those extended modes form a light cone (see Figure 2-9). Below the light cone the guided modes, which exist due to the higher dielectric constant of the slab, are plotted. The eigenstates decrease exponentially with increasing distance to the center of the membrane.

A second important point of the PC used in this work is the design of the membrane. To facilitate the coupling of the light, an active layer with QDs is embedded. This layer simplifies a containment of light in the resonator. If the light is radiated from exterior perpendicular to the plane, most of the light would be reflected at the interface and

additionally the propagation direction of the transmitted wave mismatches the resonance conditions.

Additionally, the rate of spontaneous emission is increased and the relaxation time reduced in a resonant cavity with the same frequency as the emitter [28,35]. The rate is increased by the Purcell factor $f_{Purcell}$:

$$f_{Purcell} = \frac{3}{4\mu^2}\frac{Q}{V}\left(\frac{\lambda}{n}\right)^3 \tag{2-21}$$

with $\frac{\lambda}{n}$ the wavelength of the light in the medium with refractive index n, Q the grade of the crystal and V the mode volume.

2.3.4 Optimization of the Quality Factor

Due to the technological challenges in the III-nitride material system, only a few reports have shown cavity modes in PC in the blue/violet region. Choi et al. [36] calculated a Q factor of about $4 \cdot 10^4$ with a mode volume of about $1.3 \cdot \left(\frac{\lambda}{n}\right)^3$ for the e1 mode of h-GaN PC membranes with a L7 cavity. Experimentally, Q factors of about 800 were realized, which is due to inaccuracies in the fabrication of the PC. Quality factors of 5200 in an h-GaN PC membrane embedding InGaN QWs are shown in Ref. [37].

In order to obtain drastically increased Q factors, one opportunity is varying small details of the design of PCs. This can be realized by modifying the corners of the cavity. Triviño et al. [38] used a L3 cavity and shifted the three nearest holes outward (see Figure 2-10). Additionally, the radius of those holes was decreased. The estimated quality factor is about 110000, which is more than 65 times larger than the unmodified cavity with Q = 1700. Then again, enough periods of the photonic crystal must be available with a constant hole radius [39]. Due to the proximity effect during electron-beam lithography the holes on the edges of the PC are smaller, which has a huge impact on the quality factor of the PC. One solution to overcome this is to increase the dimension of the PC, so that the area with constant air hole radii is still huge enough.

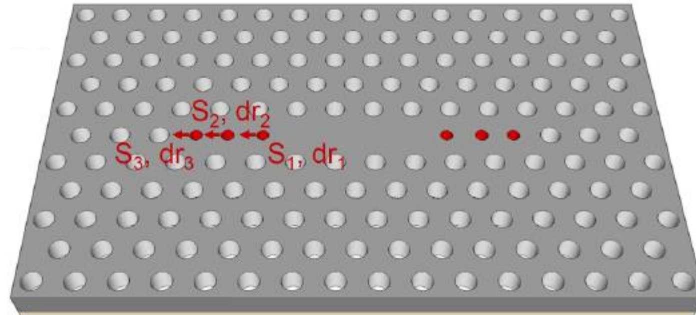

Figure 2-10: Schematic illustration of a cavity design by Triviño et al. [38]. It shows the h-GaN layer on top of an h-AlN buffer layer with a hexagonal array of holes and three holes missing in a row in the center. The holes which were modified for the optimized Q are marked in red.

2.3.5 QDs embedded in PCs

Of particular interest are PCs with QDs embedded in the active layer for application-oriented components as high-efficient single-photon-sources [40,41] or micro-lasers with low threshold current [42]. An entanglement of light in the form of photons with matter in the form of excitons is possible. Depending on the intensity of the coupling two regimes are differentiated. A weak coupling is called Purcell effect (see chapter 2.3.3). Due to a coupling with the resonator mode, a sharp increase of spontaneous emission occurs (Fermis golden rule). This process is irreversible. The integrated intensity of the exciton line is increased with approximation to the resonance of the optical mode. In the regime of strong coupling, the spontaneous emission is reversible due to an energy exchange between emitter and electromagnetic field of the resonator mode. This is called vacuum-rabi-oscillations or –splitting. A photon of the resonator mode is destroyed and generates an exciton in the QD or vice versa.

The coupling of the photon and exciton depends on the properties of the resonator as well as on the properties of the QD. A large-dimensioned resonator leads to a high coupling, thus affects the oscillation strength of the QDs. In addition, a high photonic inclusion and

a small mode volume of the resonator lead to a large coupling. The light inclusion in three dimensions is described by the Q factor.

Fast recombination times, small linewidths and high intensities are expected due to the coupling. It opens the possibility to select specific wavelengths.

3 Experimental

This section introduces at first the principle of epitaxial growth, the main setup of our molecular beam epitaxy system, including the in-situ RHEED setup, as well as the relevant growth techniques. Chapter 3.2 deals with the characterization methods used to characterize the epitaxial layers and the photonic crystal membranes.

3.1 Growth

In this work mainly, c-GaN QDs in a c-AlN matrix are grown epitaxial with a MBE system. This chapter focusses firstly on the principle of MBE growth, after that the setup used in this work is described, following the different growth techniques. At the end the setups for the fabrication of photonic crystal membranes are explained in detail. The plasma-enhanced chemical vapor deposition is used for the deposition of a hard mask as well as for the etching of the substrate. The electron-beam lithography setup enables the patterning of the sample. Reactive ion etching is used for different etching steps.

3.1.1 Molecular Beam Epitaxy

The MBE technique is based on the evaporation or sublimation of atomic beams or molecules of elements, like Ga and Al, onto a crystalline substrate face, like 3C-SiC. The ultra-pure elements are heated in effusion cells. On the substrate surface the gaseous elements are adsorbed and they diffuse, desorb and crystallize with other gaseous elements on the surface. The epitaxial growth takes place in an ultra-high-vacuum ($<10^{-9}$mbar). This is one of the main advantages of the MBE system, because it makes it possible to use in-situ measurement techniques during the growth, for example reflection high energy electron diffraction (for more details see section 3.1.2). Furthermore, the MBE system ensures a precise control of the beam fluxes and growth conditions. Normally the growth in a MBE chamber is far from thermodynamic equilibrium, resulting in surface processes which are mainly governed by kinetics [43]. The most important surface processes are the adsorption and desorption of atoms or molecules, the incorporation of atoms in the lattice and the interdiffusion processes. The dominating surface process depends on the growth conditions, for example the substrate temperature, the beam flux and the surface roughness. During crystal growth, different processes occur. Physisorption is a weak binding of an atom on the surface without electron interchange. Mainly van-der-Waals forces keep the atom. On the contrary, during chemisorption electrons are exchanged between atoms. Otherwise the atoms desorb again. One important parameter is the sticking coefficient s, which describes the ratio of the adsorbed atoms and the total number of atoms arriving at the surface [43].

$$s = \frac{N_{adh}}{N_{tot}}. \tag{3-1}$$

Specific values are shown in chapter 4.2.

Table 1: Parameters for 3C-SiC.

Parameter	3C-SIC
Lattice constant a [Å]	4.36 [44]
Bandgap $E_{gap,300K}$ [eV]	2.36 (indirect) [45] 6.0 (direct) [45]
Refractive index at 3.6 eV	2.09

Table 2: Parameters for c-AlN and c-GaN used in this work.

Parameter	c-AlN	c-GaN
Lattice constant a [Å]	4.373 [46]	4.503 [21]
Bandgap $E_{gap,300K}$ [eV]	5.93 (direct) [47] 5.3 (indirect) [47]	3.23 (direct) [48]
Effective conduction band mass m_e^*/m_0	0.3 [49]	0.19 [49]
Effective hole masses		
m_{hh}^*/m_0	1.32 [49]	0.83 [49]
m_{lh}^*/m_0	0.44 [49]	0.28 [49]
Split-off mass m_{so}^*/m_0	0.55 [49]	0.34 [49]
Deformation potential [eV]		
a_c	-6.8 [50]	-2.77 [49]
b	-1.5 [49]	-2.67 [51]
Refractive index at 3.6 eV	2.19	2.73

To realize epitaxial grown layers of c-GaN or c-AlN a cubic zinc blende substrate is needed. In this work, 3C-SiC pseudo-substrates are used. They consist of a 10 µm thick 3C-SiC (001) layer, which is grown epitaxially on a 500 µm silicon (Si) (001) 4" wafer. 3C-SiC is an indirect semiconductor with a lattice constant of 4.36 Å and a bandgap of 2.36 eV at room temperature (see Table 1). This work presents the growth of thick c-AlN epilayers and c-AlN matrixes with c-GaN QDs incorporated. In Table 2 the most important physical properties of both materials are listed. Due to the different lattice constant of the used materials shown in Table 1 and Table 2, a lattice mismatch occurs during a heteroepitaxial growth of, for example, c-AlN on 3C-SiC or c-GaN on c-AlN.

The lattice mismatch f between two materials can be calculated with [52]

$$f=\frac{a_{substrate}-a_{layer}}{a_{substrate}}. \qquad (3\text{-}2)$$

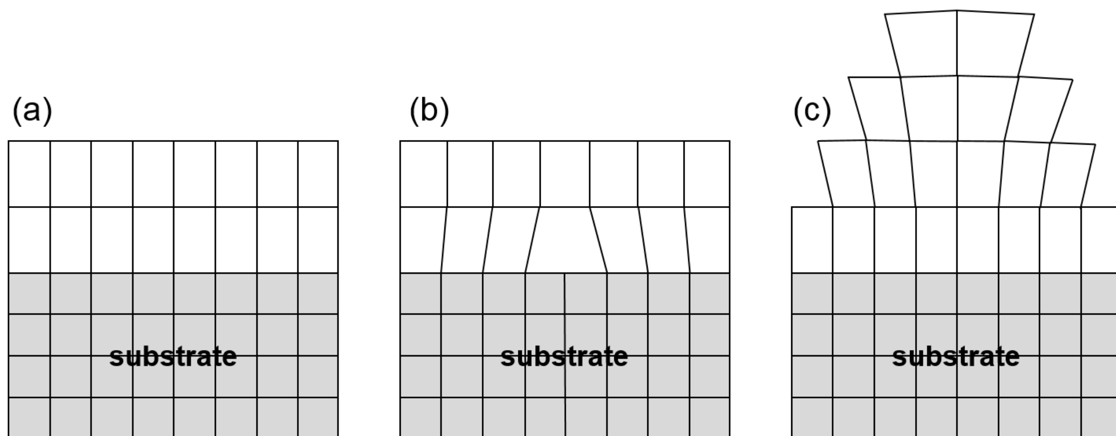

Figure 3-1: Growth on a lattice mismatched substrate (a) pseudomorphically strained growth, (b) partially relaxed layer and (c) island growth. The lattice constant of the substrate is smaller than that of the epilayer.

Therefore, the lattice mismatch between c-AlN and 3C-SiC is consequently around -0.25 % and much smaller than the lattice mismatch between c-GaN and 3C-SiC, which is -3.2 %. The lattice mismatch of c-GaN grown on c-AlN is about -3.0 %. This pseudormorphical strain originates from the difference in the lattice constants between the substrate and the epilayer in case of a lattice constant of the substrate which is smaller compared to that of the epilayer (see Figure 6-2). The lattice constant in plane of the epilayer matches the lattice constant of the substrate, resulting in a modification of the lattice constant of the epilayer in out-of-plane direction. In this case, the grown epilayer is compressively strained. It is also possible to obtain a tensile strained epilayer if the lattice constant of the substrate is bigger compared to that of the epilayer.

If the film thickness increases, it is sometimes energetically more favorable to form dislocations in order to decrease the strain [53]. The total energy, which is approximated by the sum of the elastic energy and the surface energies of all facets forming the island has to be minimized [54]. A partially relaxed epilayer is one opportunity (see Figure 6-2 (b)) and another is the formation of islands (see Figure 6-2 (c)).

The critical thickness, above which dislocations or islands are formed, is determined by [55]

$$h_c = \frac{b}{2\pi f} \frac{(1-\nu \cos^2\alpha)}{(1+\nu)\cos\lambda} \left(\ln\frac{h_c}{b}+1\right) \tag{3-3}$$

with b the absolute value of the Burger vector, f the mismatch of the system, α the angle between the dislocation line and its Burger vector, λ the angle between the slip direction and the direction of the film, which is perpendicular to the line of the intersection of the slip plane and the interface.

The Burger vector is $b=\frac{a}{\sqrt{2}}$ [56] and $\cos\lambda = \cos\alpha = \frac{1}{2}$ [52].

The Poisson ratio for the standard (001)-oriented substrate can be calculated with

$$\nu = \frac{c_{12}}{c_{11}+c_{12}}, \tag{3-4}$$

where c_{11} and c_{12} describe the components of the elastic tensor of the epilayer, which depend on the growth direction.

Sherwin et al. [57] estimated the critical layer thickness with the help of Matthews' and Blakeslee's force balance method to 0.7 nm (3 ML) for c-GaN and 14.1 nm (63 ML) for c-AlN on 3C-SiC.

As already mentioned, one opportunity is the formation of islands after the critical thickness. The growth mode is called Stranski-Krastanov growth. In this mode, a critical layer thickness of approximately 2 monolayers (MLs) is reached. Generally, there are three different growth modes. The Frank-van der Merwe (FM) growth is a layer-by-layer growth and island growth is called Volmer-Weber (VM) growth. The most common way to realize QDs is the self-assembled Stranski-Krastanov (SK) growth (see Figure 3-2). This growth technique is a mixture of FM and VW growth modes. The important parameter is the lattice mismatch between the film and the substrate. This growth mode represents firstly a layer-by-layer growth. After a critical thickness the wetting layer (WL)

and 3D islands (QDs) are formed. Due to this island formation the pseudomorphical strain of the layer is reduced.

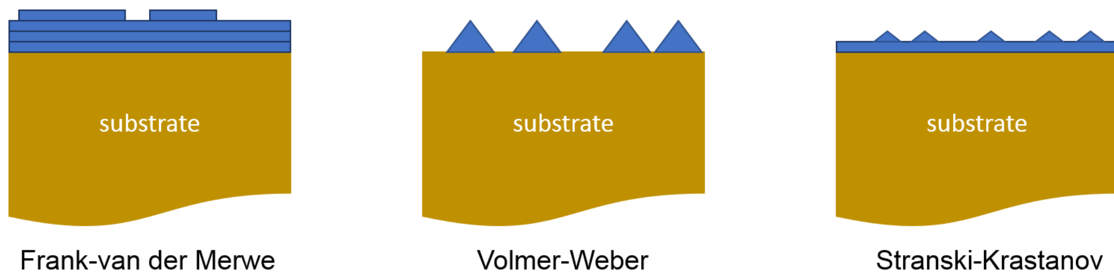

Figure 3-2 Schematic representation of the three different growth techniques: Frank-van der Merwe, Volmer-Weber and Stranski-Krastanov (after [43]).

All samples presented in this work are grown epitaxially by plasma-assisted molecular beam epitaxy (PAMBE) in a RIBER 32 MBE system equipped with an Oxford Applied Research CARS 25 rf activated plasma source. A schematic drawing is shown in Figure 3-3. Standard effusion cells, which are mounted between 5 and 32 degrees from the horizontal plane, are used for the evaporation of gallium and aluminum. The beam equivalent pressure (BEP) of each cell was calculated by measuring the background pressure and the beam flux pressure with the help of a Bayard-Alpert-Gauge, mounted at the back of the sample holder. The nitrogen was derived from dissociation of N_2 using the above-mentioned plasma source. Flow rates of the nitrogen gas around 0.2 sccm are used resulting in an N background pressure of about $2 \cdot 10^{-5}$ mbar. A liquid-nitrogen-shroud minimizes the residual water vapor and carbon-containing gases in the growth area. The substrate is mounted on a heated sample holder, which can be tilted to set the ideal angle between substrate and effusion cells and it can be rotated in order to achieve a homogeneous thickness across the substrate. Common substrate temperatures during growth are around 730°C. The growth is in-situ, monitored with reflection high energy electron diffraction (RHEED), described in section 3.1.2.

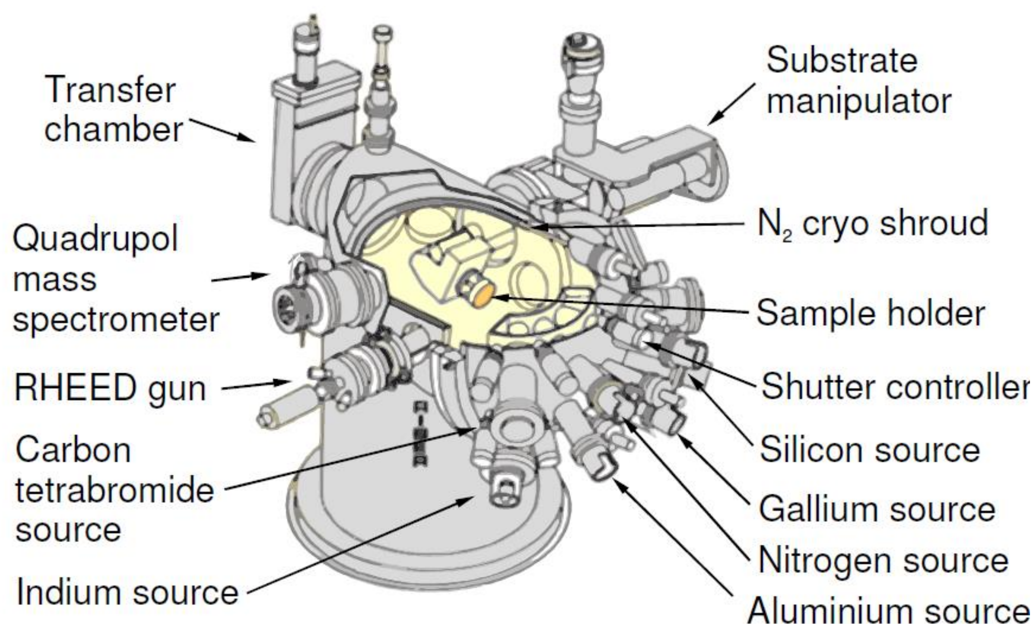

Figure 3-3: Schematic drawing of the MBE Riber 32 system [58].

3.1.2 Reflection High-Energy Electron Diffraction

The growth of the metastable cubic phase of GaN and AlN is only possible in a small parameter range. It is therefore necessary to monitor the growth. A high-energy electron beam with acceleration voltages between 10 and 30 kV (in this work 16 kV, 1.6 mA) is focused on the sample during reflection high-energy electron diffraction (RHEED). In this work a STAIB system is used. The angle of incidence is small with 0.5-2.5 [59], so the electron beam is mostly diffracted on the surface. The diffracted pattern becomes visible by a phosphor screen, which is recorded by a digital camera connected with a computer. Additionally, an aluminum layer is coated on the backside of the phosphor screen to increase the light output by reflecting the light to the viewers direction, which otherwise would be lost towards the vacuum chamber.

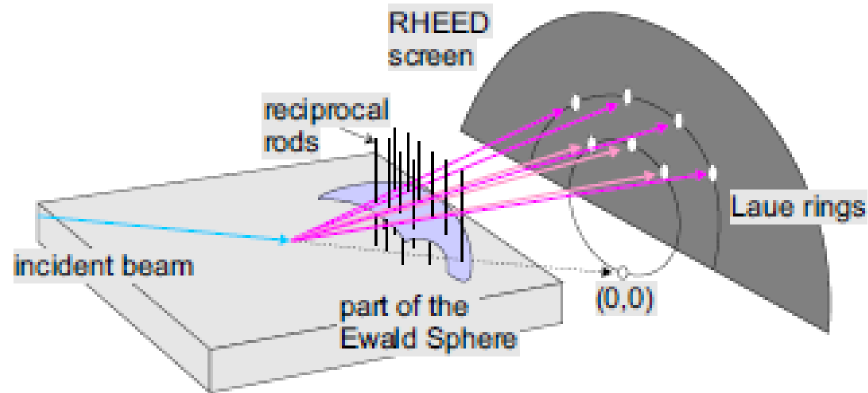

Figure 3-4: RHEED diffraction by means of the Ewald-sphere construction [60].

Figure 3-4 shows the main principle of the RHEED setup. The lattice points of the sample are described by infinite long rods with a thickness depending on lattice imperfections and thermal vibrations. The Ewald-sphere is used to describe the diffraction pattern. In fact, diffraction occurs if the wave vector of the diffracted electron k' is a multiple of the lattice vector wave vector of the incoming electron k_0. Whereby the dependence $|k_0|=|k'|$ applies to elastic scattering and therefore this corresponds to the radius of the Ewald-sphere. Hence, all diffraction reflexes match the intersections of the rod with the Ewald-sphere. The diffraction reflexes are arranged on Laue-rings, which are located above the shadow line (grey-shaded part on the RHEED screen in Figure 3-4). An ideal crystal would show spots on the screen, in a real crystal there are various reasons for a deviation, which are discussed in the following. Due to the sample size, the crystal is not extended infinitely, which leads to an increased spot size. In addition, the surface is not ideally smooth, which also results in an increased spot size. The indicator for a smooth 2D surface is a streaky RHEED pattern. Due to the size of the rods and the thickness of the Ewald-sphere, which is finite and depends on the spreading and the focusing of the electron beam, and furthermore due to the radius of the Ewald-sphere, which is much larger than the distance of the rods, a vertical expansion of the reflex occurs leading to a streaky reflex. In the case of 3D island growth spotty reflections are visible in the RHEED pattern.

3.2 Characterization

The ex-situ characterization methods are described in the following. For the structural characterization, atomic force microscopy, scanning electron microscopy, transmission electron microscopy and high-resolution x-ray diffraction are used. For optical characterization of the quantum dots and the photonic crystal membranes the photoluminescence spectroscopy is used.

3.2.1 Atomic Force Microscopy

Atomic force microscopy (AFM) measurements are done with a Nanosurf Mobile S device to receive information about the surface quality. In this work it is used for the determination of the surface roughness after the growth of thick c-AlN layers and capped QD layers. Additionally, uncapped c-GaN can be visualized and characterized. The basic principle is the scanning of the sample surface with a flexible cantilever with an atomically sharp tip. If the tip is in atomic scale, the surface and the tip interact with each other. This can be described with the help of the Lennard-Jones potential (see Figure 3-5 (b)), which is defined for the interplay of forces for neutral atoms [19]. Depending on the distance between the atoms an attraction or repulsion exists between them. The AFM can operate in two different modes, the contact mode and the non-contact mode. For the contact mode the tip is directly in contact with the substrate and a repulsive Coulomb interaction between tip and sample occurs. Repulsive Van-der-Waals forces appear for the non-contact mode, where a small distance is adjusted between the tip and the sample. The disadvantage of the contact mode is the possibility to damage the sample, so it is only used for hard materials. To measure the deviation of the cantilever a laser beam is focused on the cantilever end and then it is reflected onto a photodetector with four quadrants (see Figure 3-5 (a)).

(a)

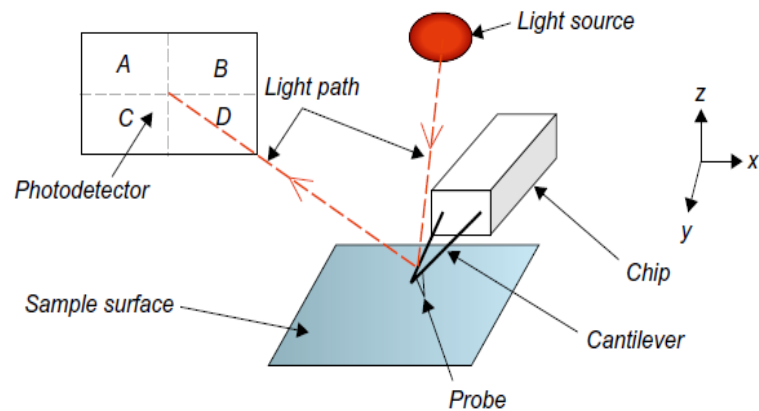

(b)

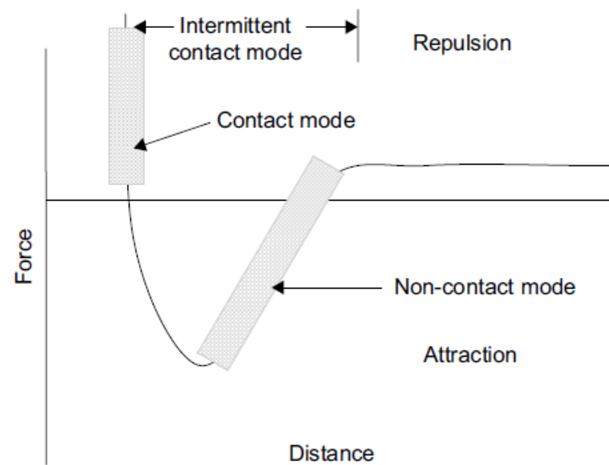

Figure 3-5: (a) Basic principle of an AFM setup. (b) Lennard-Jones potential showing the inter-atomic force over the distance between two atoms. Additionally it is shown in which force regimes the three different AFM measurement techniques are operating [61].

3.2.2 High-Resolution X-Ray Diffraction

High-resolution X-ray diffraction (HRXRD) is a standard method to characterize epitaxial layers non-destructive and ex-situ. The composition as well as the crystal quality of semiconductors can be investigated. X-rays are used, because the wavelength is in the same order of magnitude as the lattice constant of crystals. Figure 3-6 shows the main setup. An incident X-ray beam is directed at the sample, which is mounted on a goniometer stage. At the crystal planes the beam is diffracted, which can be described by the Bragg equation [62]

$$n\,\lambda = 2\,d_{hkl}\,\sin(\omega), \qquad (3\text{-}5)$$

where n is a natural number describing the order of diffraction, λ is the wavelength of the X-rays, d_{hkl} the distance between the lattice planes and ω the angle between the incident beam and the surface of the sample. If this equation is fulfilled, constructive interference occurs. The diffracted beam is detected and a reflex can be observed. Another important parameter is the angle Θ, which describes the angle between the crystal planes and the incident beam (see Figure 3-6). The angle between the incident and diffracted beam is 2Θ. The measurements are done in reciprocal space, where the diffraction plane is represented as a reciprocal lattice point. More information about X-ray diffraction can be found in [63].

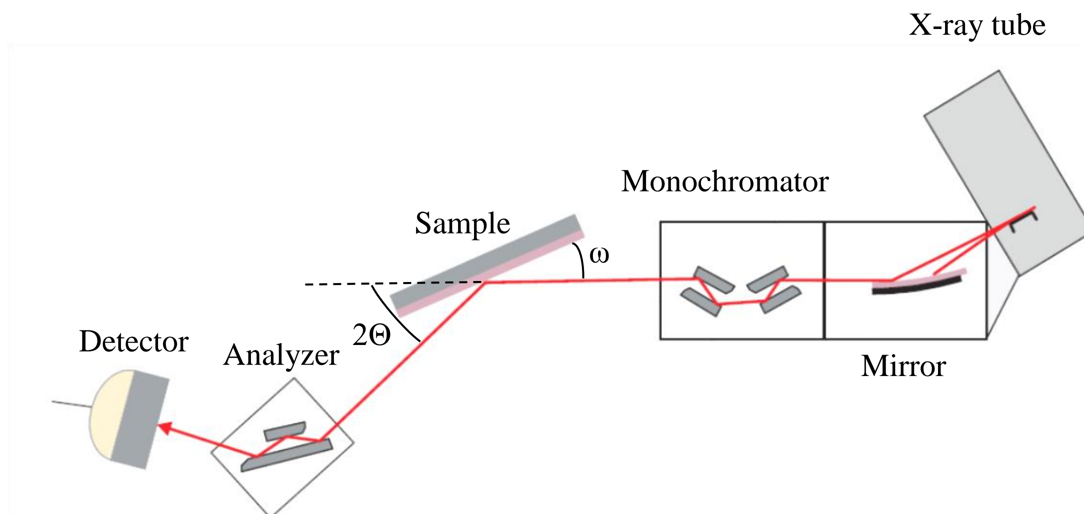

Figure 3-6: Illustration of the HRXRD setup [64]. From right to left: X-ray tube, mirror, monochromator, sample, analyzer and detector. The sample is mounted on an Euler cradle. The angles of the incoming (ω) and diffracted beam (2Θ) are shown, too.

Different measurements can be realized including ω-scans, ω-2Θ and 2D intensity distribution mapping in the reciprocal space, called reciprocal space maps (RSM).

During a ω-scan the incident angle is varied by "rocking" the sample. This measurement is also called rocking curve. It measures a reciprocal lattice spot while the scattering vector is moved along $q_{\parallel}$. Information about the crystal quality with the help of the intensity distribution as a function of the incident angle can be obtained.

Another possible measurement is the ω-2Θ scan, which contains information about the lattice constant and indirectly about the chemical composition. The incident angle as well as twice the detector angle are shifted.

Combining both measurement techniques, a 2D map of the sample is measured (RSM). The area around a reciprocal lattice point is measured here. The intensity is mapped as a function of the lattice constants $q_{\perp}$ and $q_{\parallel}$. The lattice parameter as well as the strain can be determined.

The HRXRD setup in this work is a Philips X'Pert materials research diffractometer with a copper anode emitting a $K_{\alpha 1}$ radiation (λ = 1.54056 Å). The monochromator has a parabolic mirror and a (220) channel-cut germanium crystal (2-crystals, 4 reflections) which only lets the $K_{\alpha 2}$-line through. The X-ray beam reaches the sample under grazing incidence, which leads to an elliptical spot on the sample. The diffracted beams are detected by a multichannel detector (Philips Analytical X'Celerator detector) with an analyzer (220 germanium crystal, 3 reflections) and a CCD detector.

3.2.3 Photoluminescence Spectroscopy

To determine the optical properties of semiconductors like the band gap energy, impurities or material quality, the easiest way is to measure photoluminescence (PL), because it is a non-destructive and sensitive measurement technique [65]. With the help of a monochromatic laser light, electrons in the sample are lifted from the valence band into the conduction band. The missing electron in the valence band is called hole. After a specific lifetime, the electron is falling back in the equilibrium state by non-radiative or radiative processes. One possible transition is the emission of a photon, which possesses the energy of the band gap of the semiconductor. Many transitions can be observed during PL spectroscopy measurements. Band to band transitions (e, h) is the recombination of an electron in the conduction band with a hole in the valence band. Another common transition in high quality semiconductors is the free exciton transition (FX). Due to the mostly high dielectric constant, the coulomb attraction is reduced hence leading to a weakening bond between electron and hole, which can be described as free electrons and holes with influencing wave functions, because of the coulomb-interactions. Bound

exciton transition (D^0, X/A^0, X) and donor acceptor transitions (D^0, A^0) are possible if the semiconductor is doped. The above described transitions are shown in Figure 3-7.

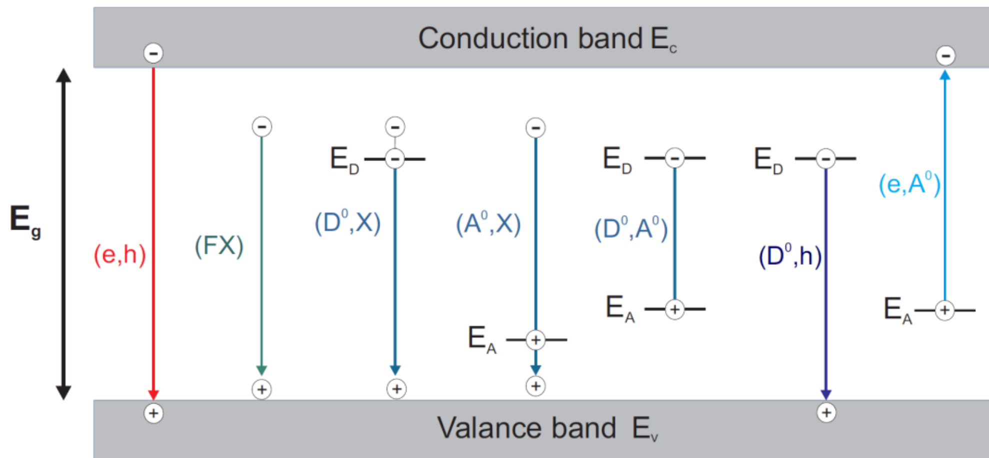

Figure 3-7: Schematic diagram of the several radiative transitions in a semiconductor: band to band transitions (e, h), free exciton transitions (FX), bound exciton transition (D^0, X/A^0, X) and donor acceptor transitions (D^0, A^0) (after [60]).

Fundamentally, it is possible to use various types of lasers with energies larger than the band gap of the semiconductor.

In this work different setups are used. For the characterization of the grown bulk samples with embedded QDs, a normal PL setup was used with a Nd:YAG laser with two frequency doubling steps emitting at a wavelength of 266 nm (energy: 4.66 eV). The laser is used at a power of 5 mW and has an excitation spot diameter of 2 µm. A Spex270M monochromator with a grating of 300 lines per millimeter and a Hamamatsu type 943-02 GaAs photomultiplier or an Andor CCD (iDus 420) are applied to detect the PL signal. An edge filter is used to eliminate the laser lines in the spectra.

For the characterization of the PC membranes, a µ-PL setup is used. Due to the small diameter of about 2 µm of the laser beam, it is possible to illuminate one single PC. The measurement setup used is shown in Figure 3-8. It consists of a Helium-Cadmium-laser with wavelengths of 325 nm and 441.6 nm. With the help of a bandpass filter, wavelengths outside a range of 275 nm to 375 nm are blocked. A beam splitter deflects the beam and then it is focused on the sample with an objective (NA=0.55). The emitted photoluminescence signal is guided through the beam splitter again by the same objective. A movable mirror allows the signal to be conducted either to a CCD-camera or to the spectrometer. With the help of the camera the sample can be observed live, which is

especially important when measuring photonic crystals. On its way to the spectrometer, the beam passes through a longwave-pass filter and a lens. The lens focuses the beam on the entrance slit of the grating spectrometer. Two different grids are available here (150 lines per millimeter with 500 nm blaze wavelength and 1200 lines per millimeter with 500 nm blaze wavelength). Furthermore, the sample is mounted on a movable table. It can be adjusted in x-y-direction with a resolution of approx. 100 nm using piezo actuators.

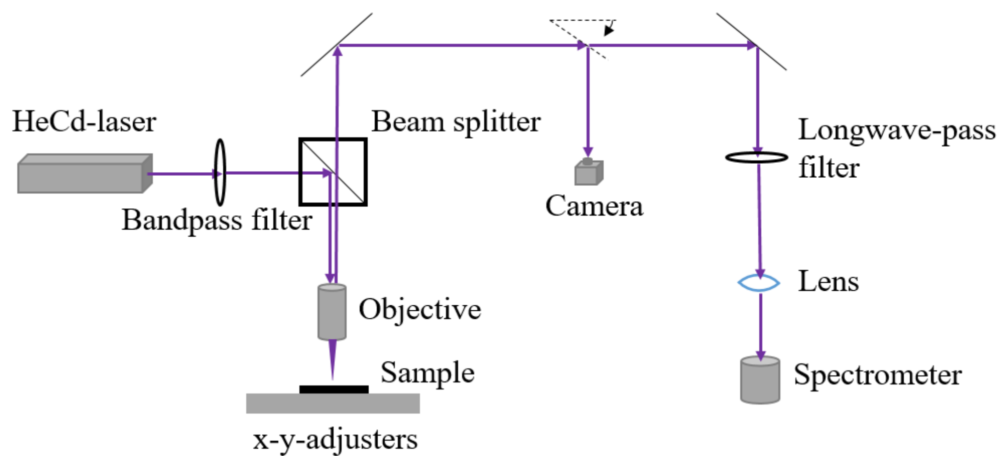

Figure 3-8: Schematic illustration of the μ-PL setup in the group of Prof. Dr. C. Meier.

3.2.4 Electron Microscopy

In this work the electron microscopy is used for different applications. The fabrication of the photonic crystal membranes are realized with electron-beam lithography due to the small dimensions of the air holes using a Raith Pioneer system. To determine the quality, scanning electron microscopy (SEM) images with the same system are realized. The characterization of the QDs is performed by a Jeol TEM which is additionally equipped with an EDX to analyze the chemical composition. In the following the main principal of each measurement technique is described.

3.2.4.1 Scanning Electron Microscopy

The scanning electron microscopy (SEM) is based on the principle that an electron beam, focused by several electromagnetic lenses, scans the specimen. Due to the interaction of the incident electron beam and the sample different signals, like X-rays or secondary electrons (SE) and auger electrons, can be detected, which give information about the chemical composition or the surface quality.

In this work a Raith Pioneer system was used with two different detectors and an additional writing unit for lithography. Voltages up to 25 kV are built with a Schottky-field emission cathode. For image generation a SE detector at the side and an InLens detector are available. The SE have energies up to 50 eV and result from inelastic scattering of the primary electrons in the upper atomic layers.

For the electron-beam lithography (EBL) the current of the electron beam is measured by a faraday cup to guarantee a constant current with sub picometer resolution. In this work a voltage of 25 kV with an aperture size of 7.5 µm is used, which leads to a current of approximately 14 pA or a dose of 60 $\frac{\mu C}{cm^2}$.

3.2.4.2 Transmission Electron Microscopy

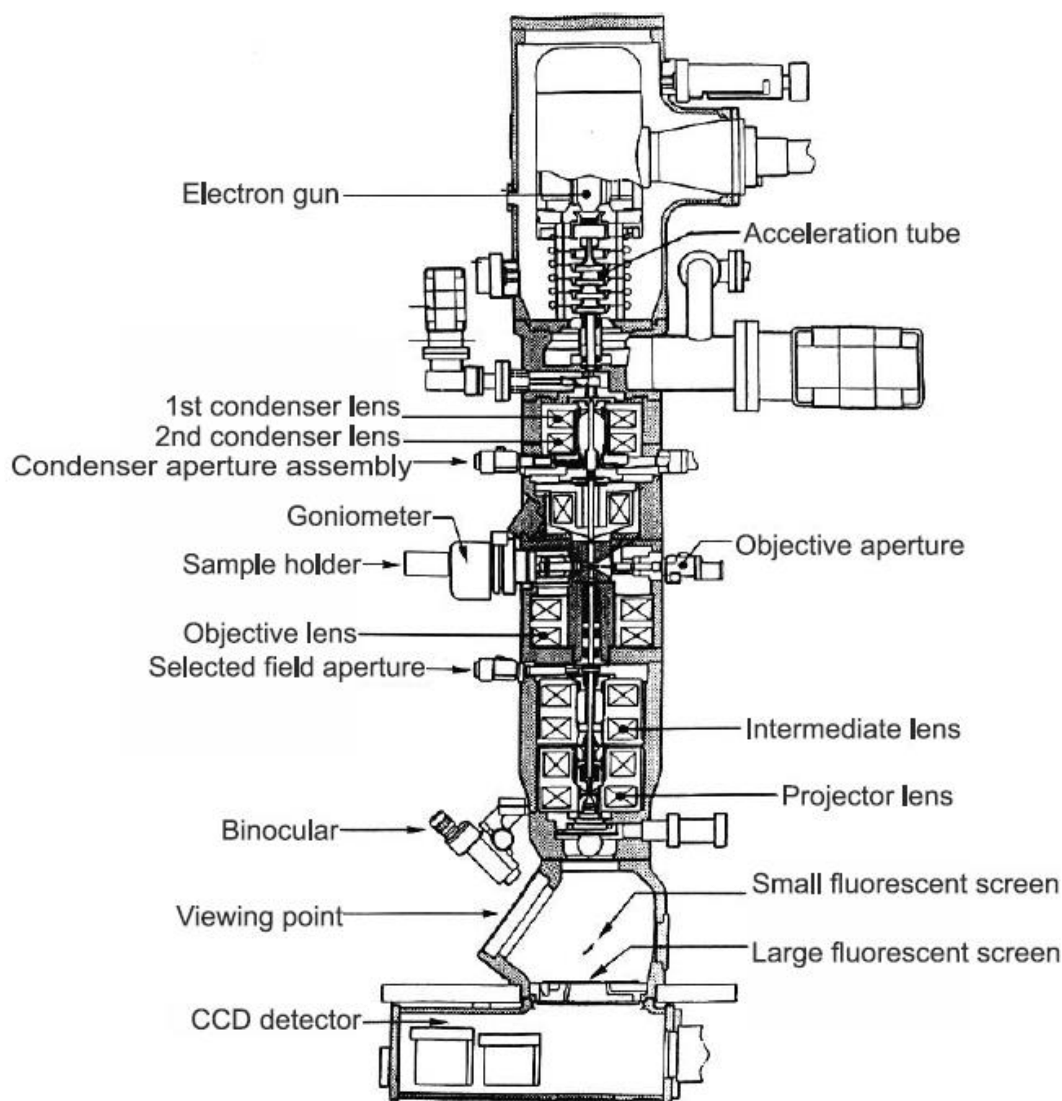

Figure 3-9: Basic setup of a TEM system (after [66]).

For a characterization in an atomic range, transmission electron microscopy (TEM) images are performed. The basic setup is shown in Figure 3-9. As described in chapter 3.2.4.1 electrons are generated and focused with the help of condenser lenses onto the sample. The difference is the voltage, which is in this case between 80 and 300 kV to reach the atomic resolution. The sample requires special preparation. It is thinned out by focused ion beam (FIB) so that thicknesses of 50 to 100 nm for conventional TEM and 10 to 20 nm for high resolution transmission electron microscopy (HRTEM) are reached. In the sample the electrons are elastic (no loss of energy) or inelastic (electrons loose energy) scattered and additionally diffraction occurs when crystalline samples are used.

Depending on the lenses the TEM can be used as a SEM to depict the surface or the electron diffraction pattern can be shown on the fluorescent screen. The general electron beam path is shown in Figure 3-10 (a). After penetrate the specimen, the electrons are focused by the electromagnetic field or the objective lens. In the back focal plane a diffraction pattern is produced. Using an additional objective aperture in the back focal plane an image of the specimen can be generated. Two different mode are possible, the bright-field image (BF) and the dark-field image (DF). The BF image mode Figure 3-10 (b) uses the forward scattered electrons, which leads to an image of high contrast. Dark parts represent heavier atoms or parts where the electrons are strongly scattered. In the DF image mode Figure 3-10 (c) a tilted electron beam arrives the specimen. So, regions with diffractions in a specific angle appear brightly in this mode.

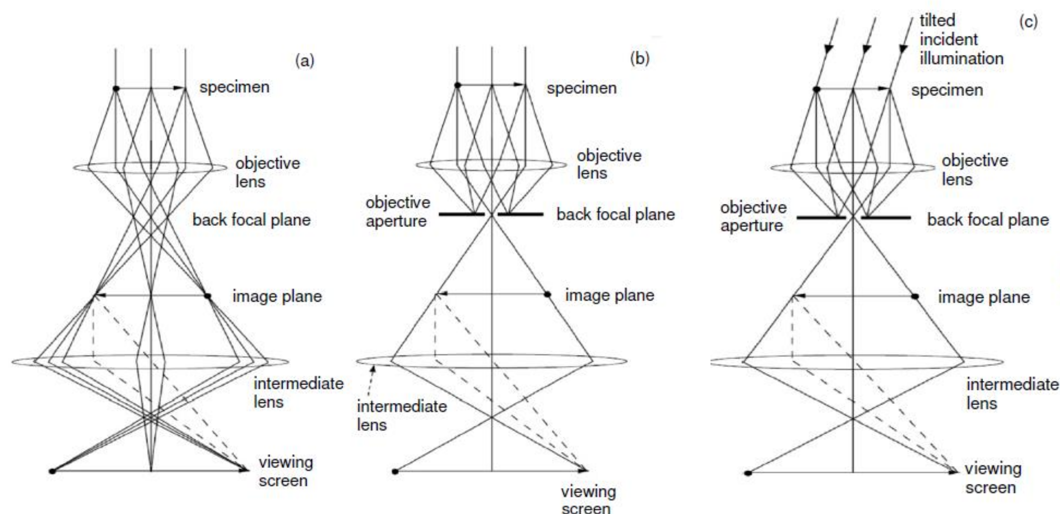

Figure 3-10: Main imaging modes in a TEM. The general electron beam alignment (a), bright-field imaging (b) and dark-field imaging (c) (after [66]).

The TEM can also be used as a scanning TEM (STEM) using scan coils to scan the specimen. Instead of the objective aperture, detectors are used to produce the image. The annular dark-field (ADF) detector detects the scattered electrons. Due to the dependence of the atomic number (z) and the scattering angle, thicker regions of the specimen or regions with high z scatter more electrons off-axis than thinner regions or lower z regions. By using a high-angle ADF (HAADF) it is possible to increase the z contrast.

It is possible to detect the characteristic x-ray radiation in a TEM as well as in a SEM, which is called the energy dispersive x-ray spectroscopy (EDX). The advantage of the combination with a TEM is that the specimen is very thin. The electron beam generates X-rays in a pear-shaped spatial volume with a diameter up to 2 µm depending on the

acceleration voltage. However, the voltage must exceed a certain value to detect all elements. Due to the small thickness of the specimen during TEM a higher spatial resolution can be reached.

4 Growth of c-AlN Epilayers and c-GaN QDs

The following chapter introduces the growth of both, c-AlN epilayers and c-GaN QDs. At first thick MBE-grown c-AlN epilayers were characterized by HRXRD to guarantee a buffer layer with high quality. Then, a single QD layer is embedded in a c-AlN matrix (chapter 4.3). The QDs are characterized structurally and optically. To increase the optical output of the QDs, the QDs need to be stacked. Chapter 4.4 introduces two stacked layers of QDs of different sizes. This structure is chosen to determine the thickness of the c-AlN spacer layers. A structural coupling as well as electronic coupling is possible with thin spacer layer thicknesses. Finally, the influence of the number of stacked layers has been investigated. It is important to note that the temperatures in this entire work refer to the indicated temperatures of the temperature controllers. The correlation between the displayed temperatures and the actual temperatures is inserted in the appendix (see chapter 9.5).

4.1 Sample Preparation

To avoid any contaminations the 3C-SiC substrates must be cleaned before growth. At first the substrate is dipped into acetone, isopropanol and DI water in an ultrasonic bath for two minutes each. Then a wet chemical etching with a hydrofluoric acid (HF)-buffered oxide etch (BOE) for 8 minutes in an ultrasonic bath is used for the cleaning. It consists of a 7:1 dilution of 40 % ammonium fluoride (NH_4F) with deionized (DI) water and 49 % HF in DI water. Afterwards, the final cleaning step is realized in the MBE chamber (see chapter 3.1.1) to remove oxides of the sample surface. This was implemented by Al flashes, where an Al flux of approximately $3\cdot10^{14}\,\frac{1}{cm^2 s}$ is deposited on the substrate surface at a temperature T_{sub} = 910°C for 5 s, followed by a break of 30 s. Due to the high substrate temperature the deposited Al desorbs in this break. The cleaning of the surface is also visible in the RHEED pattern, which is nicely streaky after 10 cycles of Al flashes [46]. Additionally, reflexes of the (2x2) surface reconstruction are visible (see Figure 4-1) indicated by the light streaky reflections in between the (-1,0) and (0,0) and the (0,0) and (0,1) reflections. The total intensity of the complete RHEED signal is much higher, too. The intensity of the diffraction reflexes depends on the degree of coverage of the surface. The rougher the surface the smaller the RHEED intensity. Therefore, the cleaning of the surface leads to a considerable smoother surface. In addition, Kikuchi-lines are visible in the RHEED pattern after the cleaning steps. Kikuchi-lines indicate an atomically smooth 2D surface.

After the cleaning steps, the substrate is cooled down to T_{sub} = 760°C, which corresponds to the growth temperature. It should be noted that the temperatures mentioned in this work refer to the displayed values of the temperature controller.

(a) (b)

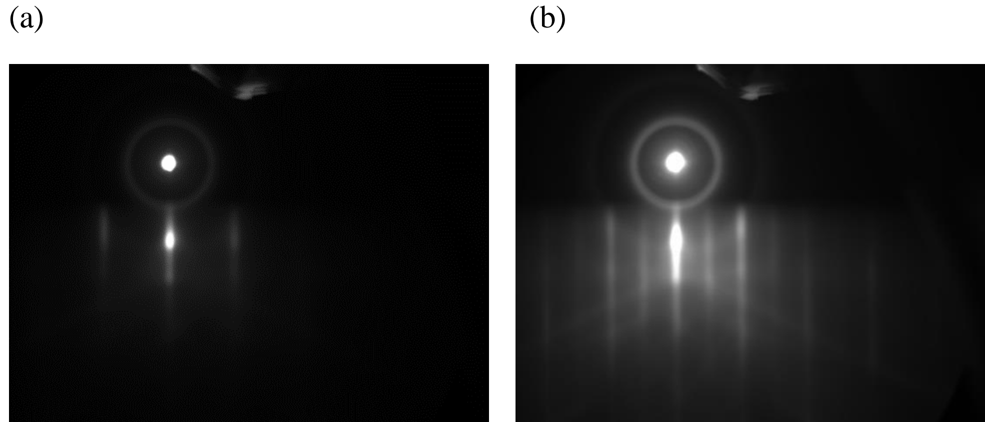

Figure 4-1: RHEED pattern of 3C-SiC measured at the [110] azimuth before Al flashes (a) and after 10 cycles of Al flashes (b). The Al flashes lead to a brighter and nicely streaky pattern with reconstruction reflexes in between the main reflexes.

4.2 Thick c-AlN Layers

The growth of c-AlN is only possible in a very small growth window, especially for the growth of thick c-AlN layers the parameters must fit right from the beginning. How to find the perfect growth parameters will be explained in the following. Mainly, the growth model of c-AlN [46] is similar to that of c-GaN [67].

It has been shown by As [68], that the growth of high quality c-GaN, which shows the lowest surface roughness to date, is only possible with 1 ML of Ga on the surface. This approach has already been applied to c-AlN layers using 1 ML of Al on the surface [69]. A main difference between the growth of c-GaN and c-AlN is the sticking coefficient which differs for the both materials (see equation (3-1)). While the sticking coefficient for Ga is s = 0.5, the sticking coefficient for Al is s = 1 at the used growth temperature. Due to the high sticking coefficient of Al the parameters are even more sensitive. If the Al flux is too high, Al droplets are formed on the surface. Usually, the best growth is achieved with an Al flux of $2 \cdot 10^{14} \frac{1}{\text{cm}^2\text{s}}$ and a N_2 flux of 0.21 sccm at a power of 260 W of the plasma source. To ensure an Al-rich growth 1 ML of Al is deposited on the surface before opening the N and Al shutter simultaneously for 20 s. The first few MLs are dominated by the VW growth, indicated by spotty reflections in the RHEED pattern. Then

the growth mode switches to the FM layer-by-layer growth showing a streaky RHEED pattern.

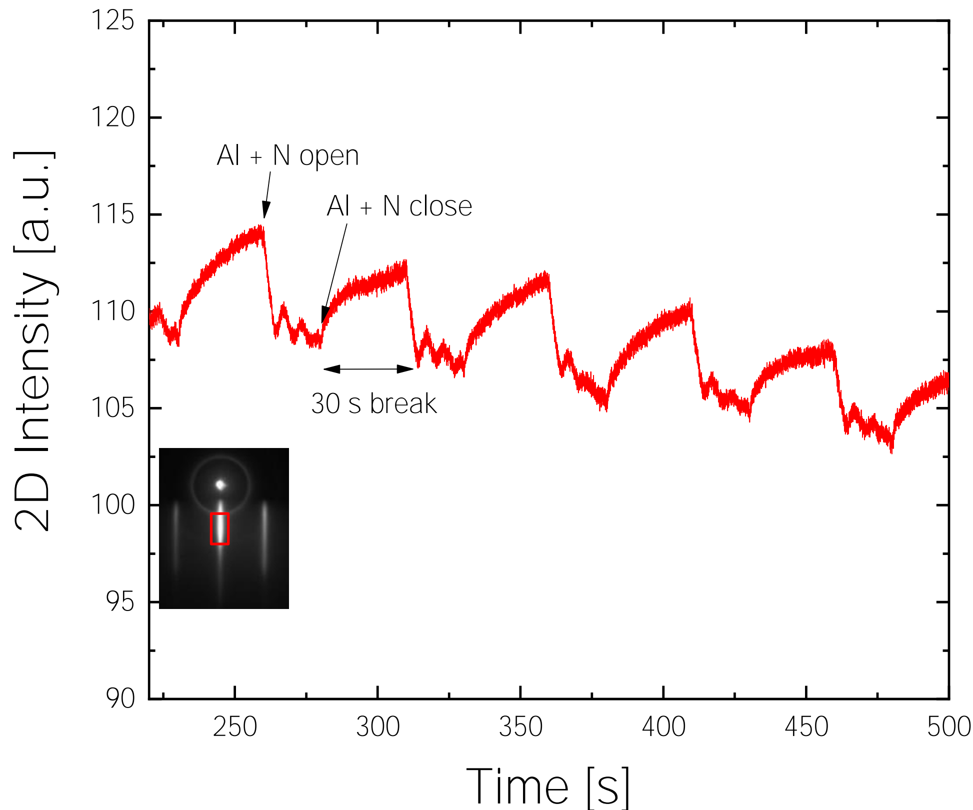

Figure 4-2: RHEED intensity of the 3D part of the (-1,0) reflex during c-AlN growth. The growth is determined by 20 s of depositing Al and N on the surface and 30 s break afterwards with both shutters closed. The inset shows the RHEED intensity pattern during the growth.

To reach a high quality flat c-AlN layer, the growth is interrupted after 20 s of growth for a break of 30 s (see Figure 4-2). In this break the main shutter is closed. In the RHEED intensity of the 3D part of the (-1,0) reflex an increase of the intensity is visible, which is due to a diffusion of the Al atoms on the surface leading to a flattening of the surface. During the growth cycles intensity oscillations are visible which supports the adoption of a FM layer-by-layer growth. The growth rate can be defined to a value of 0.27 $\frac{\mathrm{ML}}{\mathrm{s}}$ which corresponds to 211 $\frac{\mathrm{nm}}{\mathrm{h}}$ (1 ML of c-AlN is equal to 0.2175 nm). The decrease of the oscillation amplitude is due to a growth of more than one layer simultaneously. As already described, the growth break leads to a flattening and a subsequent FM growth again.

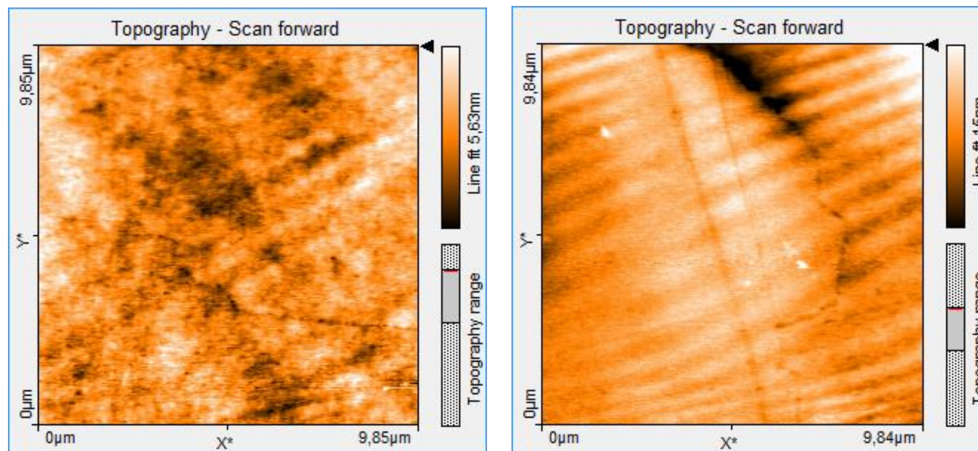

Figure 4-3: AFM measurements on c-AlN layers. The sample with 60 nm (a) has a rms of 0.91 nm. After a thickness of 230 nm the rms increased by a factor of two and results in a rms of 2.4 nm.

To determine the surface roughness after growth, AFM measurements are realized. Figure 4-3 (a) shows a 10 x 10 µm² field measured after growth of 60 nm c-AlN. The root mean square (rms) of the sample is 0.91 nm, which is comparable to the rms of the 3C-SiC substrate before growth. Increasing the growth time so that a thickness of 230 nm c-AlN is reached, leads to an increase of the roughness by a factor of two. More precisely, Figure 4-3 (b) shows a rms of 2.4 nm for the complete 10 x 10 µm² field. Excluding the upper part of the measurement, where a domain boundary is clearly present, the rms reduces to a value of 1.8 nm, which is still twice the value of the thin c-AlN layer.

A very smooth surface up to a layer thickness of 100 nm is also observable in the RHEED pattern. Figure 4-4 shows RHEED pattern after different growth thicknesses. In Figure 4-4 (a) the c-AlN layer with a thickness of 30 nm shows a streaky pattern indicating a smooth 2D surface. Increasing of the growth time to 33 minutes (see Figure 4-4 (b)), corresponding to a c-AlN thickness of 117 nm, lead still to a nice streaky pattern and a 2D surface. However, the intensity of the RHEED pattern is decreased. The thickest layer which was reached in this work is shown in Figure 4-4 (c) with a c-AlN layer thickness of 230 nm. In this RHEED pattern the streaky reflections are still visible, however, an increase of the 3D spotty reflections is observable (marked with yellow boxes). This indicates an increase of the surface roughness due to a faceting of the surface, which is observed in the AFM measurements, too. Additionally, next to the (1,0) reflection weak reflections appear. These reflections are due to hexagonal inclusions. Due to this reason the growth is stopped at this moment. A continuation of the growth would lead to several reflections along the diagonal lines indicating an increase of the hexagonal inclusions.

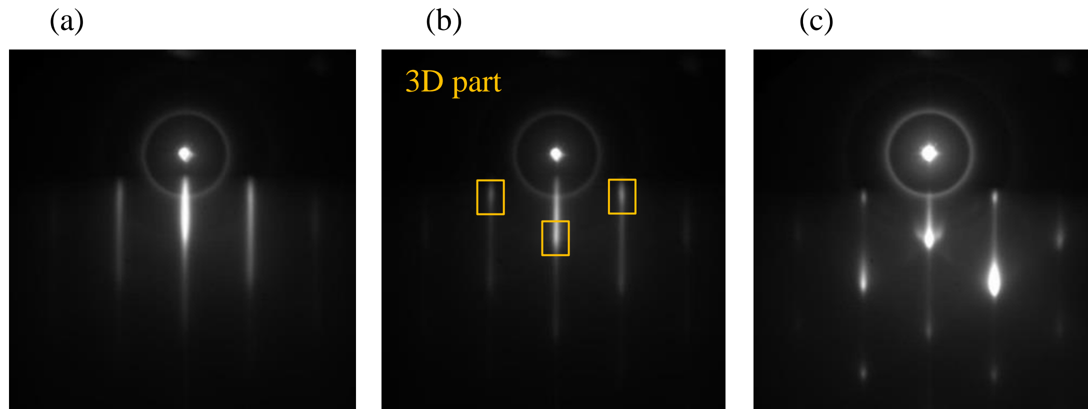

Figure 4-4: RHEED pattern measured at the [110] azimuth of AlN growth after 9 min (30 nm) (a), 33 min (117 nm) (b) and after 65 min (230 nm) (c).

HRXRD measurements of c-AlN layers are only possible using long integration times. Due to the small difference between the lattice constants of c-AlN and 3C-SiC, in the HRXRD measurements the peaks of both lay nearly at the same point in the symmetric map. Figure 4-5 shows the results of a (002) symmetric scan on both, the 3C-SiC substrate and a thick c-AlN layer (230 nm) epitaxial grown on the substrate. The position of the intensity maximum is almost the same for both samples. Due to small shifts during calibration, no exact statement can be made here.

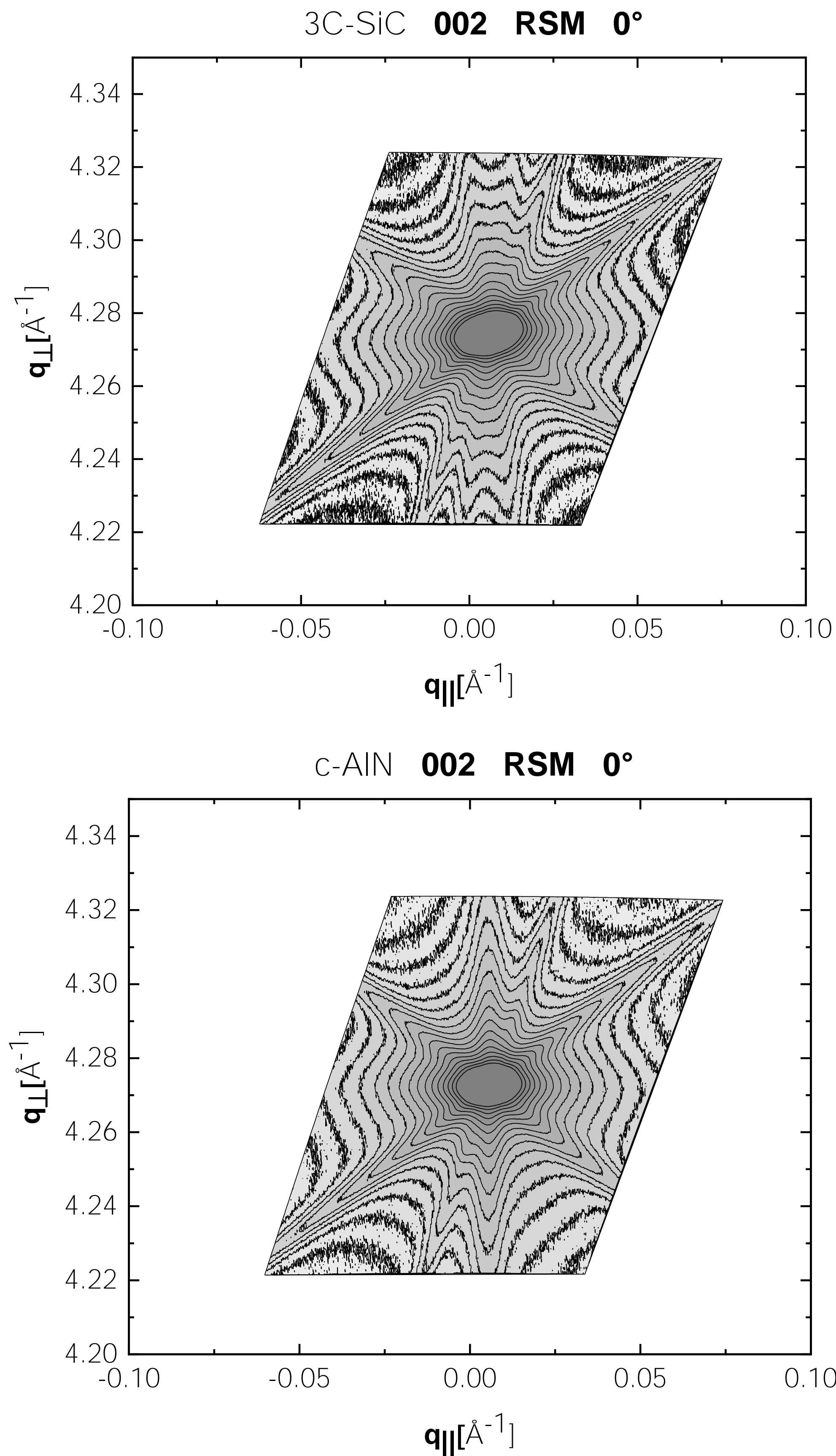

Figure 4-5: Reciprocal space map around the (002) reflex of 3C-SiC and a thick layer of epitaxial grown c-AlN on 3C-SiC.

4.3 Single QD Layers

In the following chapter cubic c-GaN QDs are realized on top of the c-AlN layers described before (chapter 4.2). A sample series is fabricated consisting of a c-GaN QD layer embedded between a c-AlN spacer and a top layer with a thickness of 30 nm each. The thickness of 30 nm ensures a surface with a small roughness after overgrowth of the c-GaN QDs. A smooth surface after the top layer is very important for further growth steps or structuring of the layer. This chapter focuses on the growth of the c-GaN QDs, including RHEED intensity measurements, the analysis of the RHEED pattern and the structural characterization of the sample with AFM measurements and optical characterization by PL measurements.

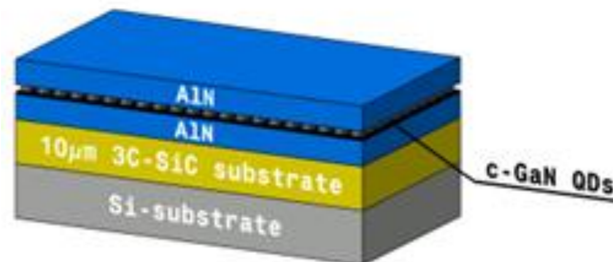

Figure 4-6: Sample structure of sample series A with one layer of QDs embedded in a c-AlN matrix of 30 nm layer thickness each on top of a 10 µm thick 3C-SiC substrate grown on a 500 µm Si (001). By changing the growth time, the amount of deposited c-GaN is varied between 13 and 30 s, which corresponds to a c-GaN coverage of 3 to 5 ML.

For the optical characterization one of the interesting parameters is the emission energy. Due to the dependence of the emission energy of the QDs on the QD size, a sample series is realized. This sample series consists of four samples with c-GaN deposition times varied between 13 and 30 s. The growth rate of a c-GaN bulk sample is 130 nm per hour, so the c-GaN deposition times correspond to a c-GaN coverage of 3 to 5 ML, respectively. One ML of c-GaN is equivalent to 0.225 nm.

Table 3: List of sample series A with one layer of QDs. The c-GaN deposition time is varied from 13 to 30 s. The GaN coverage is calculated for a layer-by-layer growth and increases from 3 to 5 ML.

Sample number	c-GaN deposition [s]	c-GaN coverage [ML]
A1	13	3
A2	20	3-4
A3	25	4
A4	30	4-5

In the following, the growth process of the c-GaN QDs is explained in detail. Basically, it is important to know that due to the large lattice mismatch, c-GaN favors the SK-growth mode on top of c-AlN layers. After the growth of the buffer layer a termination of the surface is realized (see Figure 4-7), which includes a deposition of N and Ga on the surface. At first the N shutter is opened for 7 s to saturate all open bonds. The RHEED intensity increases due to a flattening of the surface. After a short break Ga is deposited for 5 s on the surface. The intensity of the RHHED signal decreases during the deposition. After that the Ga desorbs again and the RHEED intensity increases to the value just before. Then another N termination for 7 s is done. For the QD growth the Ga and N shutter are opened simultaneously. Due to the large lattice mismatch between the two materials (see chapter 2.1) SK QDs and a wetting layer are formed. You can clearly see the turnover from 2D to 3D at a time of approximately 130 s in total. At the beginning of the QD growth the intensity of all reflexes drops sharply, but if QDs are formed the 3D part of the reflexes increases again. In this graph the QD deposition time is 25 s.

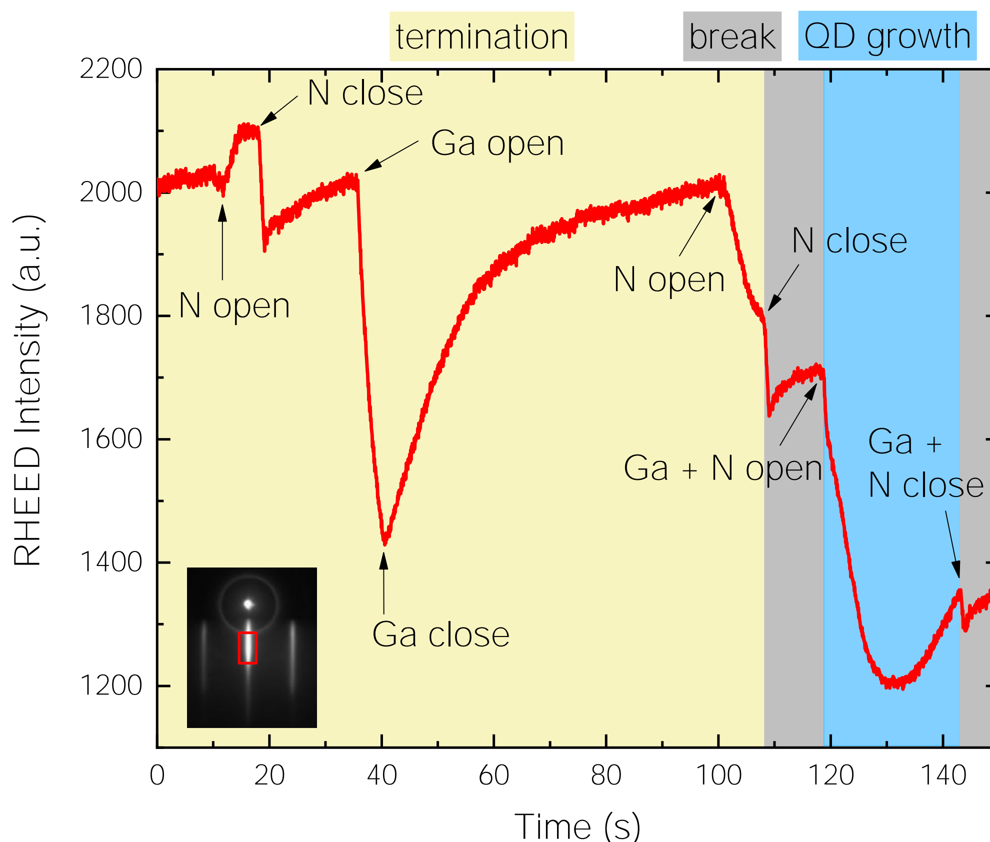

Figure 4-7: RHEED intensity of the 3D part of the (-1,0) reflex during termination and QD growth. The inset shows the RHEED diffraction pattern containing a mark for the measured point.

This formation can also be seen in the RHEED pattern. Figure 4-8 (a) shows the RHEED pattern measured at the [110] azimuth after the growth of the c-AlN buffer layer. The growth is determined by the Frank-van-der-Merwe layer-by-layer growth mode, resulting in a flat 2D surface, which can be seen in the RHEED pattern by the streaky reflexes (- 1,0), (0,0) and (1,0). As already explained in chapter 3.1.2, a 2D surface has streaky reflexes due to the size of the rods and the thickness and radius of the Ewald sphere. During the QD growth the RHEED pattern changes from the 2D pattern to a 3D spotty pattern, which indicates the formation of islands. The reflexes (-2,0) and (2,0) become visible here, because the 3D part is much brighter compared to the 2D signal. After the QD growth the QDs are capped with another c-AlN layer to enable a characterization of the QDs via optical measurements. A thickness of about 30 nm is chosen, because this corresponds to the carrier diffusion length in cubic group-III nitrides to enable excited carriers in the barrier to diffuse into the QDs [70].

The RHEED pattern after the growth of the c-AlN top layer shows a rapid smoothing of the surface resulting in streaky reflections after about 3 nm again, which again indicates a smooth 2D surface. The intensity is very similar to the intensity of the RHEED pattern after the growth of the c-AlN buffer layer, which proves a successful overgrowth of the c-GaN QDs to a total 2D layer.

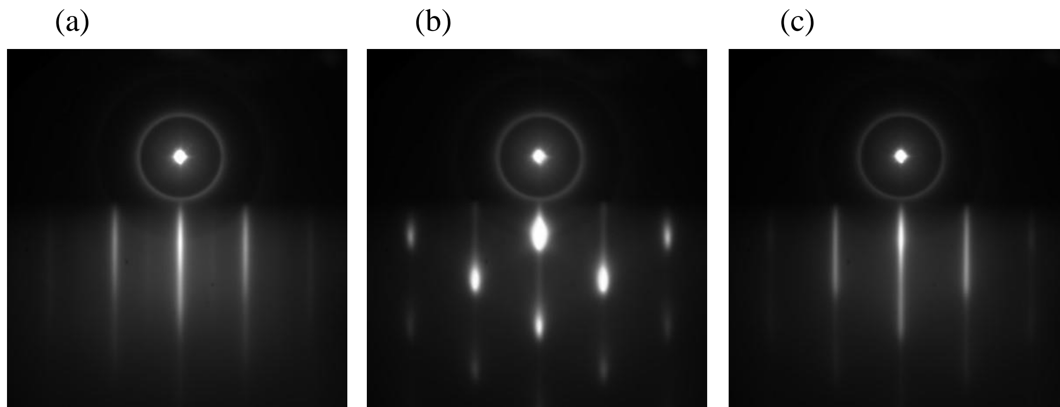

Figure 4-8: RHEED pattern measured at the [110] azimuth after growth of the c-AlN buffer layer after 13 min (30 nm) (a), the QD growth (b) and the c-AlN top layer growth after 13 min (30 nm) (c).

The roughness of the c-AlN top layer is a very important parameter. Considering, structuring of the surface with photonic crystals (chapter 6) or the overgrowth of this structure with another layer of QDs (chapter 4.4 and 4.5), it is very important to achieve the same conditions for the first and another random upper layer of QDs. AFM measurements are one good opportunity to measure the rms. Additionally, to get information about the QD formation, samples were immediately cooled down after the deposition of Ga and N and the uncapped QD layers are also characterized via AFM measurements.

In Figure 4-9 (a) an AFM image with a measured field of 500 x 500 nm² of uncapped c-GaN QDs is shown. In this sample the c-GaN deposition time is 30 s, leading to big QDs. AFM measurements on many positions of the sample are realized to determine the QD density, which is estimated to a value of $1.2 \cdot 10^{11} \frac{\text{QDs}}{\text{cm}^2}$. A sample with the same parameters for the c-AlN buffer layer and the c-GaN QD layer is realized, which is capped with an additional c-AlN layer with a thickness of 30 nm. The surface is quite smooth and shows a rms of 1.4 nm for a measured field of 10 x 10 µm². Of course, compared to a 30 nm thick c-AlN layer, the roughness is much higher, but nevertheless compared to the thick c-AlN layer of 230 nm this roughness is much smaller. In this image small islands are visible. These islands are probably Al droplets, resulting from an aluminum excess during the growth. Due to the sticking coefficient of aluminum (s = 1) at our growth

parameters, the aluminum forms islands on the surface instead of desorbing from the surface. The wave-like effects that can be seen here originate from measurement artifacts.

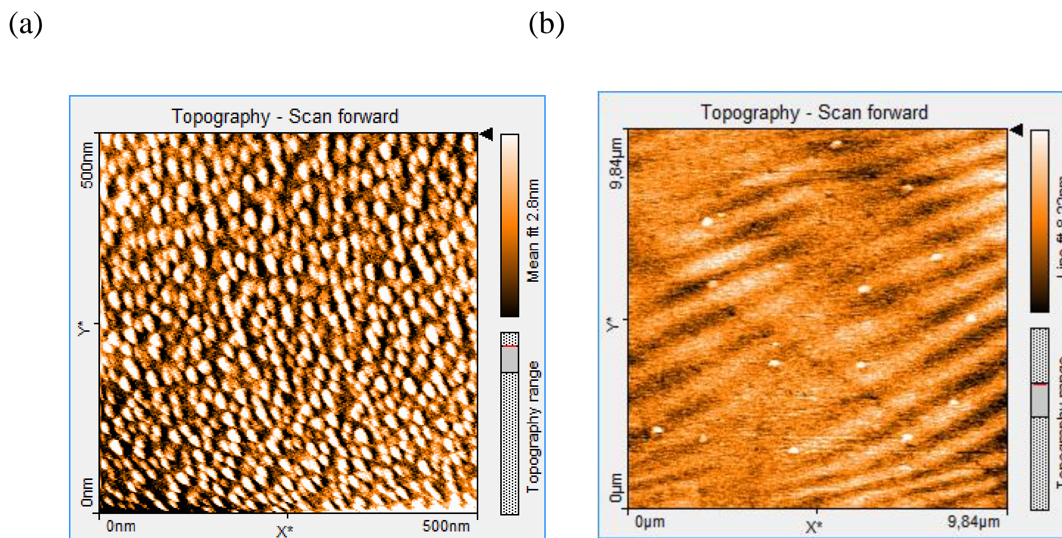

Figure 4-9: AFM images of uncapped (a) and capped (b) QDs. The thickness of the c-AlN buffer layer and in (b) the top layer, respectively, is 30 nm. The QD density of the uncapped QDs is about $1.2 \cdot 10^{11}\,\frac{\text{QDs}}{\text{cm}^2}$ and the surface roughness of the c-AlN with the capped c-GaN QDs is 1.4 nm.

The optical characterization is realized by photoluminescence measurements (see chapter 3.2.3). It is worth noting that due to the high band gap of c-AlN of 5.93 eV, no carriers are excited in this layer, as the excitation energy of the laser is too low. Therefore, only direct absorption in the QDs occurs. Additionally, it is basically possible to detect an emission of the WL. The WL layer acts like a thin quantum well. Numerical simulations show that the emission energy of a WL with a thickness of 0.2 to 0.5 results in a transition energy of 5.5 eV. This energy is much higher than the energy of the excitation source with 4.66 eV. Concluding, that in our experiments only the QDs are excited.

Figure 4-10 shows the room temperature PL spectra of the four samples described in Table 3 with different c-GaN deposition times. The normalized intensity is plotted over the energy. The spectra is plotted with an offset in y-direction. Each spectrum shows a Gaussian distribution, because the Gaussian shaped emission of many individual QDs are superimposed and lead to this broad QD ensemble peak, in contrast to the delta-like density of states of a single QD [71]. The FWHM is about 450 meV for sample A1 and about 350 meV for the other samples. It is clearly visible that the emission energy shifts to lower energies with increasing c-GaN deposition time. The smallest QDs (sample A1)

emit at an energy of 3.73 eV, whereas the biggest QDs show a redshift of 140 meV, resulting in an emission energy of 3.59 eV. Fonoberov and Balandin [20] showed that the QD height is the main confining parameter in c-GaN QDs. The redshift of the emission energy of the four spectra therefore correspond to an increase of the QD height. As already shown in the AFM measurements the QD diameter is relatively constant. As a result, this proves that the increase of the c-GaN deposition time only leads to an increase of the QD height, which causes the redshift of emission energy. Note the noise of the curves. Due to the lower deposition time of c-GaN and the associated lower density, the emission intensities of samples A1 and A2 are lower. The normalization results in a higher noise level.

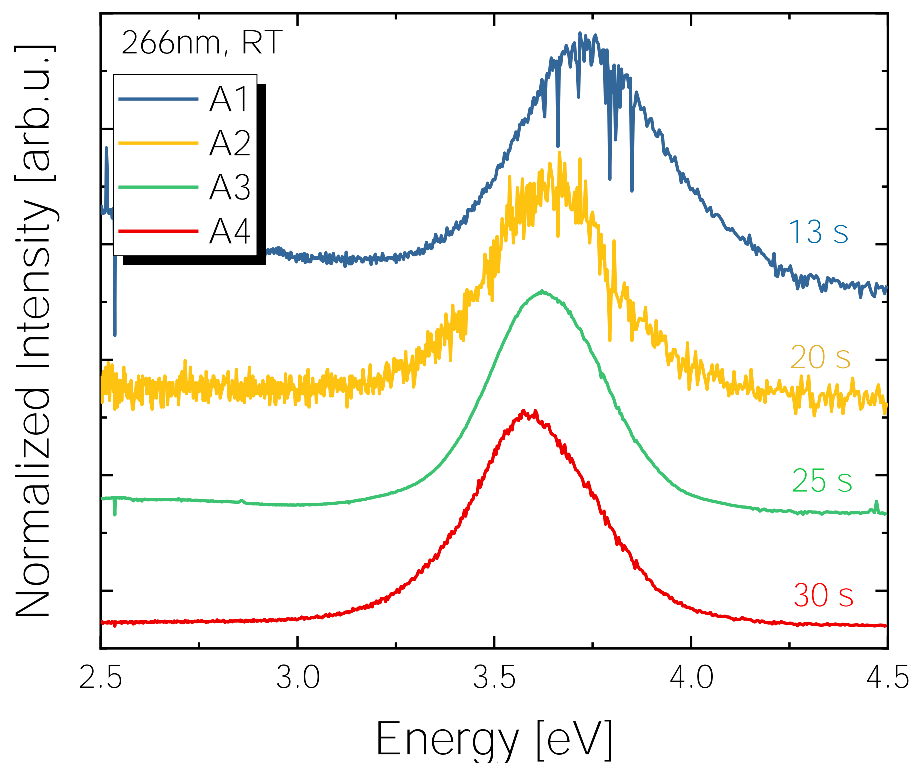

Figure 4-10: Normalized room temperature PL spectra of one layer of c-GaN QDs with deposition times from 13 to 30 s. The peak energy is shifted from 3.73 eV to 3.59 eV.

4.4 Asymmetric QD Pair

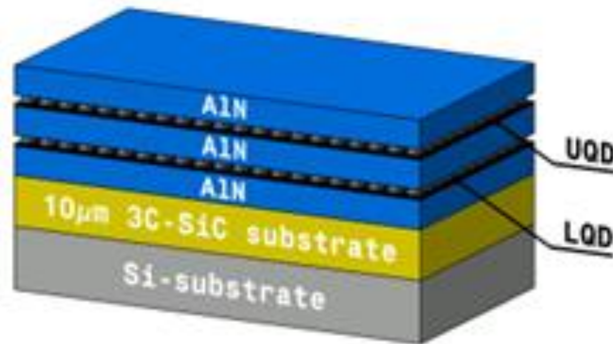

Figure 4-11: Sample structure of sample series B. The upper QD (UQD) layer is composed of bigger QDs and the lower QD (UQD) layer of smaller QDs. The c-AlN buffer and top layer have a thickness of 30 nm each, the spacer layer thickness is varied (2 and 20 nm thickness).

This chapter deals with the optical properties of stacked QDs. The stacking of QDs is a promising way to increase the performance of optoelectronic devices [1]. When stacking QDs, a coupling can occur between the individual layers of QDs. This means that on the one hand an electrical coupling and on the other hand a structural coupling between the QD layers is possible. The structural coupling will be discussed in more detail later in this dissertation (see chapter 5.2). The electrical coupling is analyzed in the following. This coupling can lead to a carrier transfer.

Table 4: List of sample series B with two layers of QDs. The deposition time of the LQD and the UQD is specified. The thickness of the spacer layer varies between 2 and 20 nm.

Sample number	Deposition LQD [s]	Deposition UQD [s]	Thickness spacer layer
B1	10	40	20
B2	10	40	2

For this purpose, a sample series with two QD layers stacked on each other is realized. The c-AlN buffer and top layer are 30 nm each, therefore comparable to sample series A in chapter 4.3. There are disparities in the deposition time of the two QD layers. The lower QD layer (LQD), which immediately follows the buffer layer, is composed of smaller

QDs (c-GaN deposition time of t = 10 s). The upper QD layer (UQD) consists of bigger QDs (c-GaN deposition time of t = 40 s). In the following this sample structure will be referred to as asymmetric QD pairs (AQDP). As shown in Figure 4-11 a c-AlN spacer layer is realized with different thicknesses of 2 and 20 nm, respectively (see Table 4).

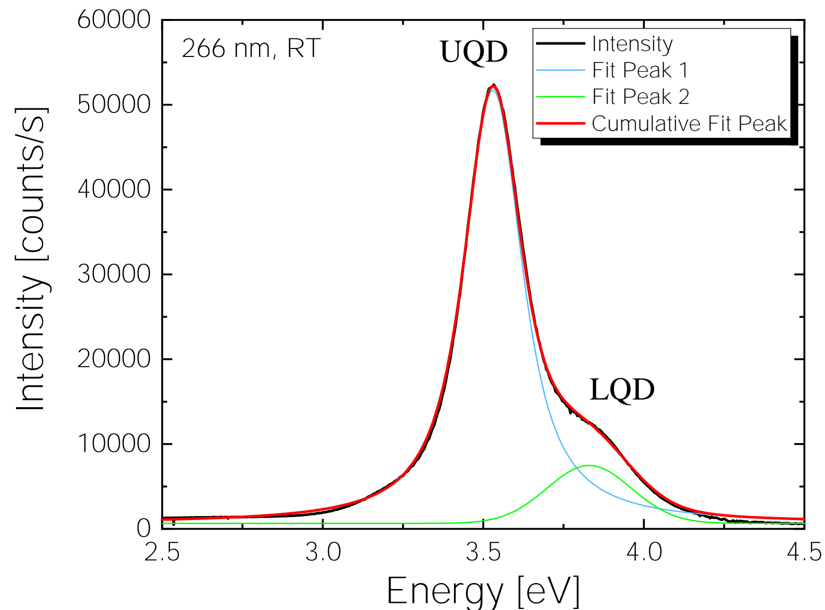

Figure 4-12: Room temperature PL measurements and corresponding fitting curve of asymmetric QD pairs with a spacer layer thickness of 20 nm (sample B1). The green line corresponds to the LQDs, the blue line to the UQDs.

The optical characterization is performed by PL measurements at room temperature. The setup is described in detail in chapter 3.2.3. Figure 4-12 shows the spectrum for sample B1, which consists of an AQDP with the thick spacer layer of 20 nm. Two peaks can be clearly identified and fitted with two Voigt functions. The red curve shows the cumulative fit, which matches the original spectrum very well. The blue curve (fit peak 1) shows an emission energy of E_{UQD} = 3.53 eV. Due to the lower energy they can be assigned to the bigger QDs (UQD). The peak intensity is about 50000 counts per second. Compared to the second fit peak (green curve), which only shows a peak intensity of 7000 counts per second, the intensity of fit peak 1 is nearly one order of magnitude greater. The emission energy is shifted 300 meV to higher energies, resulting in an emission energy of E_{LQD} = 3.83 eV. This energy fits the expected energy of the lower and smaller QDs, respectively. Comparing these emission energies to the emission energies of one single layer of QDs (see Figure 4-10) they fit very well to the development of the emission energy with changing QD size. One possible explanation for the low intensity of the lower QDs is that the energy of the emitted light of these QDs is high enough to

excite the upper QD layer. So, a part of the emitted light is absorbed by the UQDs. To reduce the reabsorption the order of the QD layers can be arranged reverse in the future.

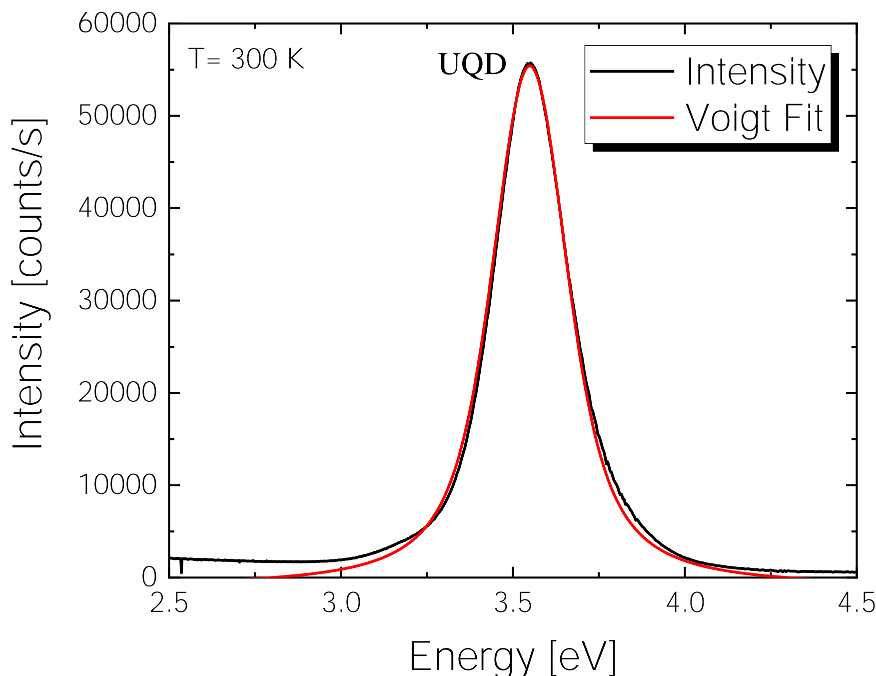

Figure 4-13: Room temperature PL measurement and corresponding fitting curve of an asymmetric QD pair with a spacer layer thickness of 2 nm (sample B2).

In comparison, Figure 4-13 shows the PL spectra of sample number B2, which consists of an AQDP with a thin spacer layer of 2 nm. It shows only one emission peak. The peak intensity with 55000 counts per second is comparable to the peak intensity of the UQD layer of sample B1. The emission energy is equivalent to the UQD layer as well. The emission energy of sample B2 amounts to E = 3.54 eV. No emission of the smaller QDs is observed.

It can therefore be concluded that the spacer layer thickness influences the electronic coupling between the two QD layers. The absence of the PL peak of the high energy QDs is a first hint of an increased carrier transfer probability between the two layers. This effect is also observed in other material systems, like in the InAs/GaAs system, where the main microscopic transfer mechanism is assigned to nonresonant tunneling [72].

4.5 Stacked QD Layers

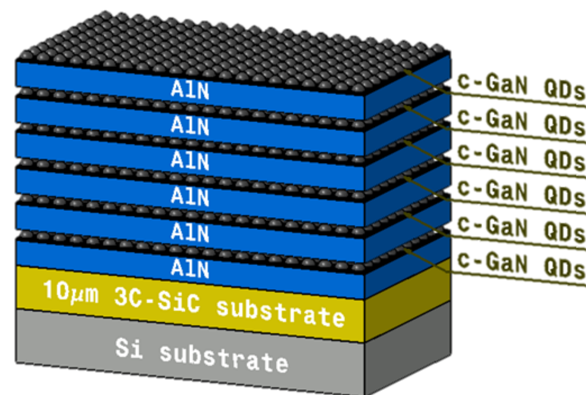

Figure 4-14: Sample structure of the sample with five stacked layers of QDs and an additional uncapped c-GaN QD layer on top. The c-AlN buffer layer and the c-AlN spacer layers have a thickness of 10 nm each.

To increase the number of QDs in the active region, one possibility is to stack the layers of QDs on each other. Samples with stacked QDs up to 20 periods were realized in this work. I will focus on a sample series with 1, 5, 8, 10 and 13 layers of QDs in this chapter to study the impact of the number of stacks on the optical properties. The thickness of the spacer layer is planned to be 10 nm each, so there is no coupling between the layers. This is important, because we want to investigate the optical output without electrically coupling between the QDs. An additional uncapped QD layer is realized on the top. In Figure 4-14 the sample structure is demonstrated by the example of a sample with 5 stacked layers of QDs and an additional uncapped c-GaN QD layer. To prevent re-evaporation of the Ga atoms it is very important to immediately cool down the sample after the deposition of the top QD layer. This top QD layer serves for ex-situ investigations of the QD size and density. In addition, samples without the top QD layer were realized to investigate the surface roughness of the c-AlN layers after several layers of QDs.

During the growth, after every c-AlN spacer layer and every QD layer, RHEED patterns are measured for each sample. The RHEED pattern of the sample with 8 layers of QDs is described more specifically in the following. In Figure 4-15 the RHEED pattern measured at the [110] azimuth after the seventh c-AlN spacer layer is shown. Comparing this to the RHEED pattern in Figure 4-8 (a) and (c) it looks very similar. The smoothing of the surface is still visible after several layers of QDs.

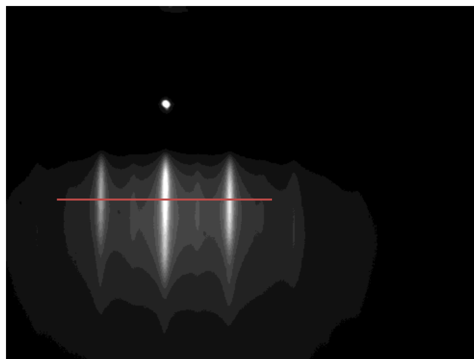

Figure 4-15: RHEED pattern measured at the [110] azimuth after the seventh c-AlN spacer layer. The pattern is still streaky and 2D.

Figure 4-16 proves the consistent quality of the c-AlN spacer layers with increasing number of QD layers. Line scans of the RHEED patterns after the third, fifth and seventh spacer layer growth were investigated. The depicted line is shown exemplarily in Figure 4-15 by the red line. It is set in a way that the (0,1) and (0,-1) reflections are depicted. At this position the 3D part is located. Therefore, an increase of the surface roughness due to a less successful overgrowth of the QDs would be immediately visible. The line scans are plotted with an offset in y-direction. The RHEED pattern shows the reciprocal lattice of the crystal, which is directly related to the lattice in the spatial domain with the help of a transformation. Consequently, the distance between the peaks, or differently said between the reflections, shows directly changes in the lattice constant. The constant distances between the (0,-1) and (0,0) and the (0,0) and (0,1) reflexes indicates a consistent lattice in each layer. Comparing the (0,-1) and (0,1) peak of each single line scan, a difference in intensity between the two peaks is observable. This difference is related to our setup. Whereas, comparing the (0,-1) peak or the (0,1) peak of each layer among each other, obviously there is a slight decrease in intensity. This behavior is also observable for the main peak. It is clearly visible that the saturation of the (0,0) reflex decreases with increasing number of stacked layers. This overall decrease of the RHEED intensity is probably due to a small decrease of the surface roughness of the c-AlN layer. Nevertheless, an increase of the 3D reflections is not observable.

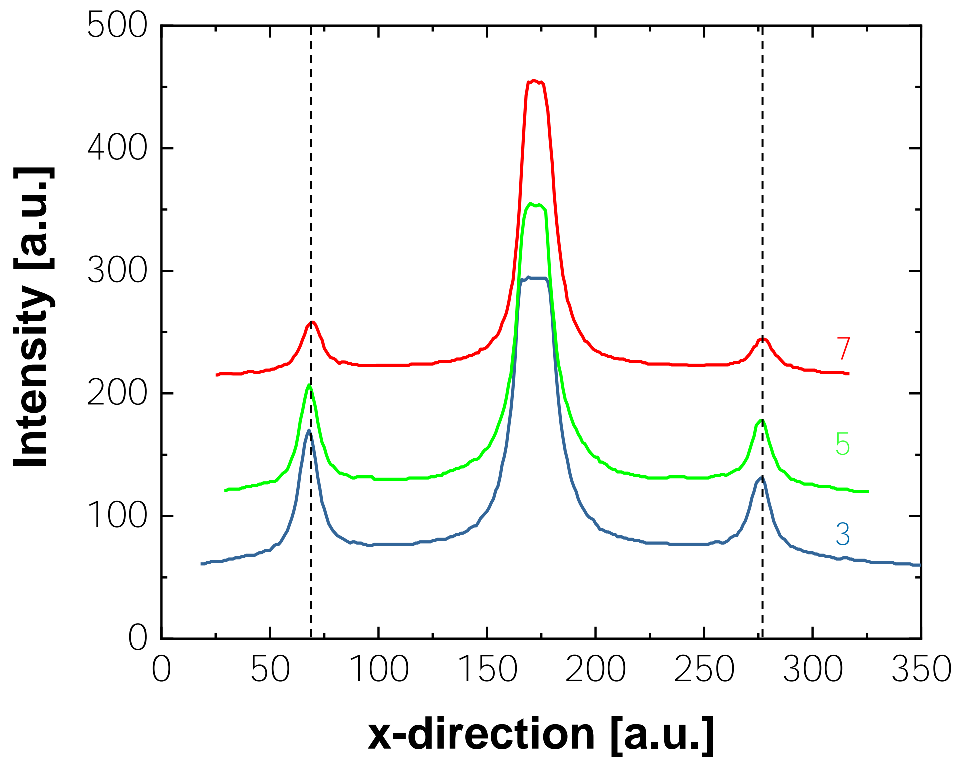

Figure 4-16: Line scans of RHEED patterns after growth of the third, fifth and seventh spacer layer. The selected position is shown in Figure 4-15. The line scans are plotted with an offset in y-direction.

The increase in surface roughness is analyzed more precisely with the help of AFM measurements. In Figure 4-18 AFM measurements for a sample with 10 layers of QDs is shown. The measured field is 10 x 10 µm². The rms is 2.7 nm, which is twice as much as the roughness of a sample with only one layer of QDs (see Figure 4-9). The slightly higher value, which was already expected due to the line scans of the RHEED patterns, indicates a small degradation of the surface quality with increasing number of stacked layers. At this point it is worth to notice that the thickness of 10 stacked layers is approximately twice as thick as the one with one layer of QDs. Additionally, the surface shows bright spots. These spots are Al droplets, which are due to slight oversupply of Al. Since the sticking coefficient at the used growth temperature is one, the Al does not desorb from the surface. So, the oversupply leads to deposits on the surface. Neglecting the two bigger droplets the rms is even better with 2.4 nm.

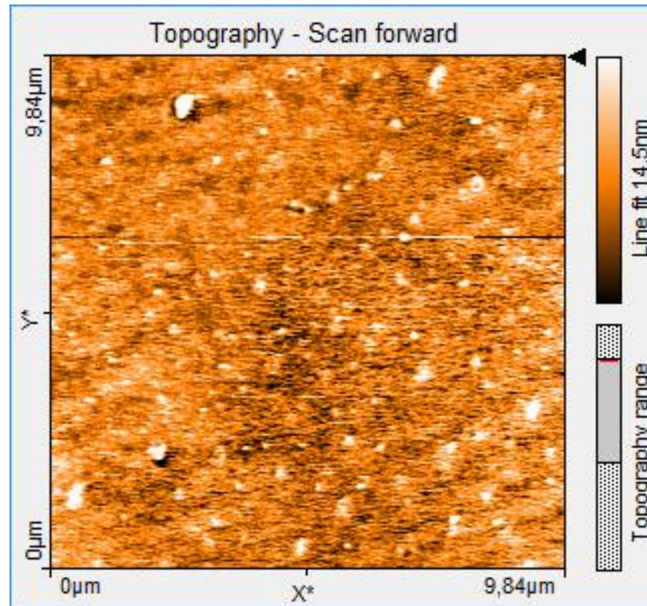

Figure 4-17: A 10 x 10 µm² AFM measurement of the c-AlN layer after 10 stacked QD layers of QDs without a top QD layer. The rms is 2.7 nm.

In Figure 4-18 AFM images with a scan field of 1 x 1 µm² of the uncapped top QD layer are shown for the sample with five and with 13 layers of QDs. These measurements were used to determine the density and the average diameter of the QDs. The average diameter is measured for 20 AFM images on different positions on the sample in a 0.5 x 0.5 µm² field. Efforts are made to ensure that in the measured fields no agglomerated QDs appear as depicted in Figure 4-18 (b) by the black circle. Several line scans were realized to determine the QD diameter, where half the maximum of the QD peaks were used as transition points for the determination of the size. The QD diameter is nearly constant in all samples and shows an average QD diameter of about d = 16 nm (±5 nm). The QD density decreases from $3.6 \cdot 10^{10}$ cm^{-2} for the sample with 5 layers of QDs to $1.76 \cdot 10^{10}$ cm^{-2} for the sample with 13 layers of QDs (see Table 5). A small decrease in QD density in the same order of magnitude was also observed by Gogneau et al. [73]. Although they realized samples with up to 200 periods they demonstrate a "homogenization of the island distribution as a function of the number of stacked layers" for hexagonal self-assembled GaN/AlN QDs.

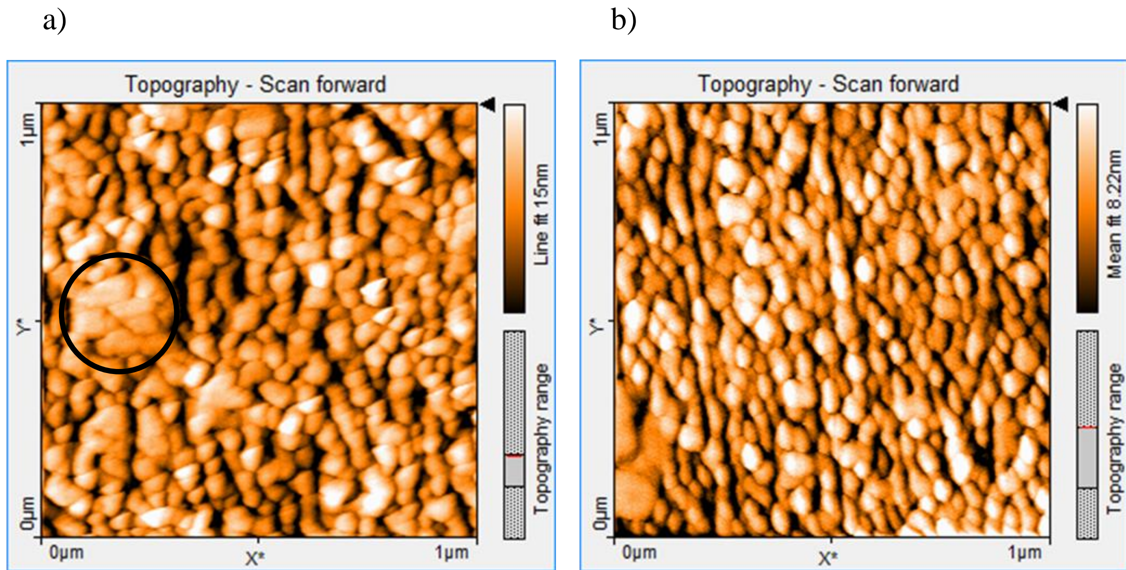

Figure 4-18: 1x1 µm² AFM scans of the uncapped top layer of QDs of (a) a sample with five stacks of QDs and (b) a sample with 13 layers of QDs.

Regarding the first 10 layers the QD shape changes in a way that the island diameter decreases, above a stable configuration is reached. The decrease of the island size is also theoretically modeled by Tersoff et al. [74] for SiGe alloys on Si or any similar systems. If the spacing between two islands is much smaller than the spacer layer thickness, the island size and spacing becomes progressively more uniform. If two islands are located very close together in one QD layer, in the next QD layer only one QD will appear at this place. The unification in size and the spacing is not visible in our samples. At this point it is important to note that the simulations were calculated for 2000 layers of QDs. For only 13 layers, as in this work, the QD density is decreased a little bit, but the spacing and the size are not uniform at all.

Table 5: QD densities for a different number of stacked QD layers. The density slightly decreases with increasing number of QD layers.

Number of stacked QD layers	5	8	10	13
QD density (10^{10} cm^{-2})	3.6 ± 0.04	2.16 ± 0.1	2 ± 0.12	1.76 ± 0.08

Additionally, in the AFM images of Figure 4-18 it is visible that the overall surface roughness is much higher. Looking at the QDs, it seems as some of them are grown on a hill and some of them are grown in a hole. This assumption is amplified by TEM measurements. A closer look to these measurements is taken in the following.

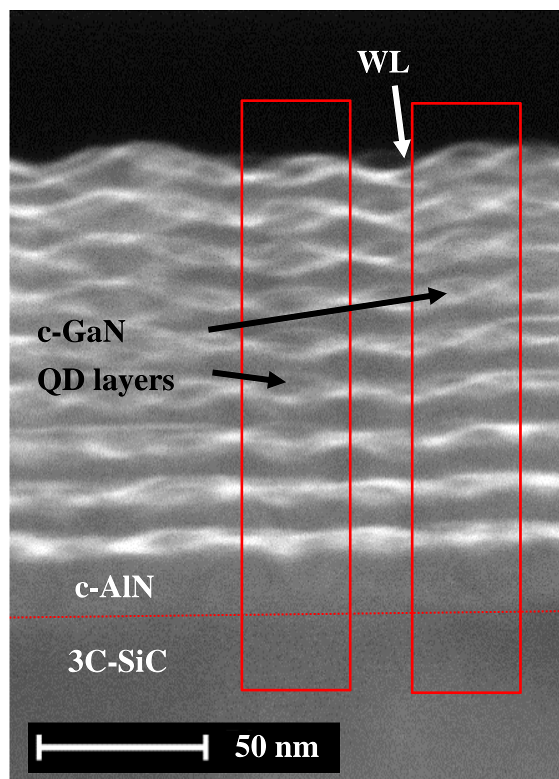

Figure 4-19: HAADF image of the sample with eight layers of QDs and an additional top layer of QDs. The red dashed line indicates the interface between 3C-SiC and c-AlN.

To determine the size more specifically and to clarify the correlations between the QD layers, TEM measurements are realized, performed in a FEI Tecnai G2 F20 [75] on the sample with 8 layers of QDs and an additional top layer of QDs. The sample is cleaved cross-sectional to see all layers of QDs. To perform TEM measurements with atomic resolution, it is very important to thin the TEM lamella out as much as possible. The thinning is done by focused ion beam [76]. HAADF as well as bright field images were performed. The HAADF in Figure 4-19 shows nicely the 8 layers of QDs and the additional top layer of uncapped QDs. The red dashed line indicates the interface between the 3C-SiC substrate and the epitaxial grown c-AlN buffer layer. The QDs, which are marked with the red boxes, and the WL appear bright. It is clearly visible that the QDs are vertically aligned along the growth direction and no stacking faults occur in this part

of the sample. However, it can also be determined that the layers are bent. The c-AlN buffer layer with a lattice constant of a = 4.37 Å is pseudomorphically strained on the 3C-SiC substrate, which has a lattice constant of a = 4.36 eV. The compressive strain in the c-AlN layer is because of the difference in the lattice constant, however the critical layer thickness (h_c = 14.1 nm) is relatively high, because of the small lattice mismatch. Due to the lattice mismatch between c-AlN and c-GaN, the c-GaN is compressively strained, too. Probably, the compressive strain in the whole structure induces the bending. This would also explain why the bending increases with increasing layer thickness. It is clearly visible that the first QD layers are smooth, whereas the top layer of QDs is strongly wavy.

In the upper part of Figure 4-19 the contrast is significantly worse. One possible reason for the low contrast is the sample preparation. If the slit-plane is not exactly in growth direction or if the QDs are not aligned vertically exactly, different planes are visible. So in the upper part of the region QDs of different depth are visible, which are overlapping in this image.

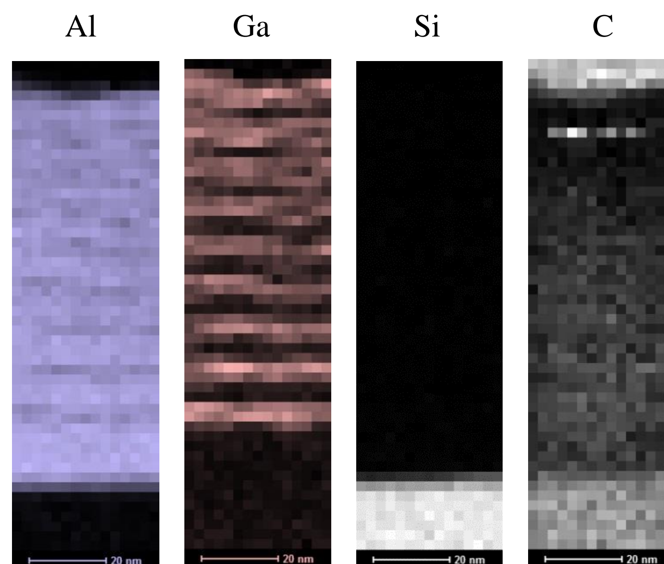

Figure 4-20: EDX mapping of the sample with eight layers of QDs and an additional top layer of QDs of the red marked in Figure 4-19. (a) Al content is marked purple (a), the red marked area shows the existence of Ga (b), the light grey part represents the Si (c) and the grey part represents the C incorporation (d).

Additionally, EDX measurements were realized on the sample with 8 layers of QDs and the additional top QD layer to prove that the growth was successful. Figure 4-20 shows the EDX mapping for the four relevant materials Al, Ga, Si and C. As already determined

before, in the lower part an abrupt interface is observable between gallium and aluminum. Therefore, we expect no Al/Ga mixing. The Carbon incorporation decreases with increasing layer thickness.

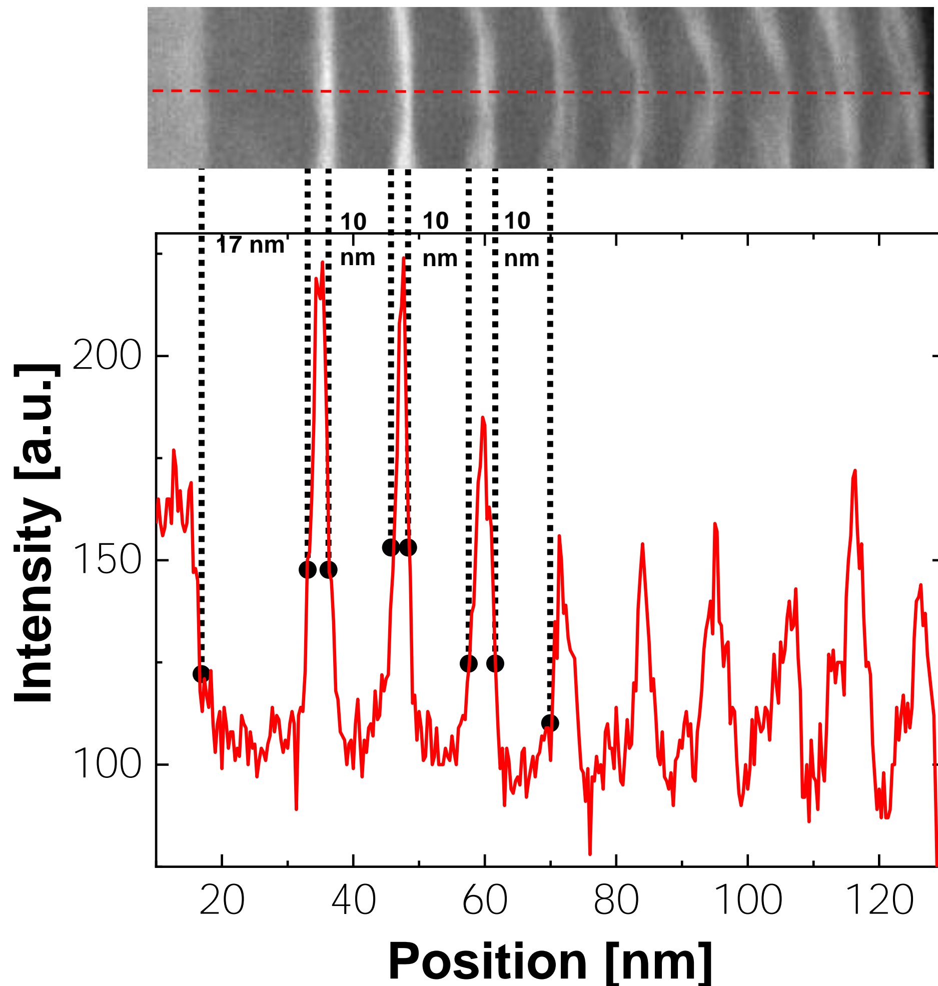

Figure 4-21: Contrast analysis of the TEM image to determine the c-AlN thickness. The upper region has been neglected, because of the low contrast ratio due to the smearing of the planes.

Figure 4-21 shows a TEM HAADF image, which depicts a part of the sample where the wetting layer is clearly visible. A line scan is implemented to determine the thickness of the single layers as marked with the red-dashed line. This scan is realized with Gatan Microscopy Suite. The contrast analysis of the line is shown in the diagram, where the intensity is plotted versus the position. Single peaks are observable attributed to the WL, which appears bright in the image. To determine the thicknesses, half of the maximum was used as transition point between AlN and GaN. It is clearly visible that the c-AlN buffer layer with a thickness of 17 nm is thicker compared to the c-AlN spacer layer with thicknesses of 10 nm. The growth conditions have not been changed. One possible

explanation is the change of the growth rate due to different sub layers. The buffer layer is grown on 3C-SiC which might lead to faster growth rates for the first MLs. The growth on the c-GaN 3D islands is much slower, maybe due to the different material or due the surface character. This leads to a thickness difference of 7 nm. The upper region of the sample has been neglected, because of the low contrast. Additionally, the thickness of the WL is determined, which is between 1 and 1.7 nm, corresponding to 5-7 ML. However, this line scan is not convincing for the determination of the exact WL thickness. It is only done to show the different thicknesses of the buffer layer and the spacer layers and not to determine any exact values.

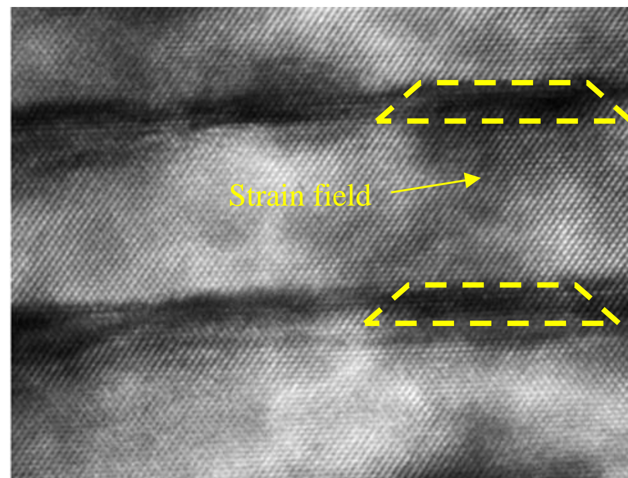

Figure 4-22: Cross-sectional TEM picture with atomic resolution in (110) direction. The GaN QD and the wetting layer appear dark, the c-AlN spacer layer brighter. No stacking fault is visible in this area. The yellow line indicates the truncated pyramidal shape.

For the determination of the WL thickness a bright field image with atomic resolution is used (see Figure 4-22). In this image the 4th and 5th QD layer is shown. The c-GaN appears darker in this image. No stacking faults are observable here. The WL thickness is determined to 0.2-0.7 nm, which corresponds to 1-3 ML. The QD shape is like a truncated pyramid, which was already expected by Fonoberov and Balandin [20]. The truncated pyramidal form is indicated by the yellow-dashed lines. The diameter of the QD is determinate to approximately 10 nm and the height is 2 nm, resulting in an aspect ratio of 5. The QDs, depicted in this image, are nicely aligned vertically through the growth direction (001). Furthermore, dark areas in the surrounding of the QDs are visible, an example is highlighted in the image. These areas appear dark due to strain fields. The QDs are grown in the SK growth mode, which leads to strain fields in the surrounding. The strain fields are the reason for the vertical alignment for small spacer layer

thicknesses. Similar observations were done for InAs/GaAs QDs by Heidemeyer et al. [4]. They showed the existence of strain fields for spacer layers of 3 and 10 nm and attributed a blueshift in emission energy to these complex strain fields.

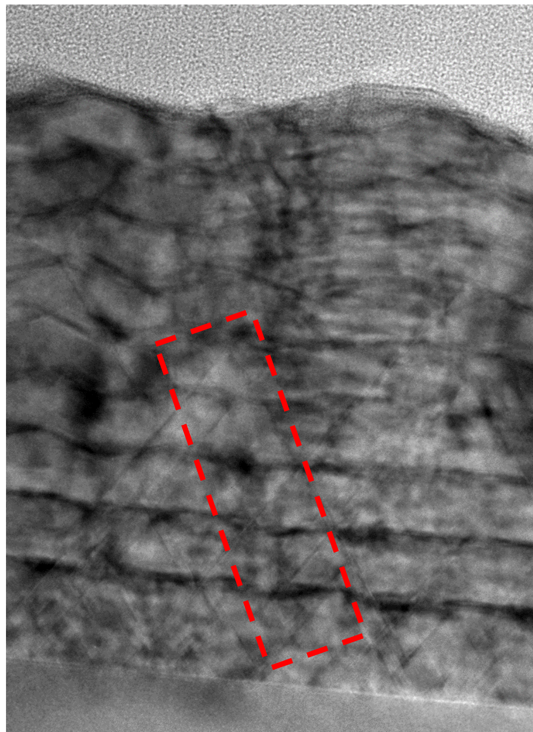

Figure 4-23: TEM picture of a sample region with stacking faults. The area framed by dashed red lines shows that the vertical alignment is tilted in (111) direction along the stacking fault.

So far only TEM images without any stacking faults or defects have been shown. Usually, in the cubic phase stacking faults occur in the [111] plane. These stacking faults are preferential nucleation sites for QDs because they behave like elastic potential minima on the surface. Daudin et al. [77] also stacked cubic GaN QD layers, however the density of the stacking faults was so high that he couldn't show a vertical alignment but an alignment which is driven by the presence of stacking faults. In our samples, we also found one region where stacking faults are observable (see Figure 4-23). This bright field TEM image also shows a sample with 8 layers of QDs and an additional top layer. The QDs and the WL appear dark. It is clearly visible that stacking faults extend to the entire sample thickness. QDs only appear at those stacking faults, so the total density of QDs is much smaller. There are areas were only the wetting layer is visible but nearly no QD.

Along the stacking faults the QDs are tilted vertically aligned in the (111) direction (see highlighted area in Figure 4-23).

Additionally, the samples are characterized optically by PL spectroscopy. The measurements are performed with a Nd:YAG laser at room temperature. The setup is explained in detail in chapter 3.2.3. In Figure 4-24 the intensity of the PL emission over the PL emission energy is plotted for the samples with 1, 5, 8, 10 and 13 layers of QDs. At first, it is worth noting that the excitation energy leads to direct absorption in the QDs, so that no absorption in the spacer layer occurs. Additionally, a peak related to the WL is not observable in this spectrum, because of its thickness of 1-3 ML. Numerical calculations show that the transition energy for thin quantum wells is larger than the energy of the used laser of 4.66 eV, so the WL peak is not in the measured energy scale. Due to the energetically more favorable position of the QDs compared to the WL the carriers will move to the QDs either way.

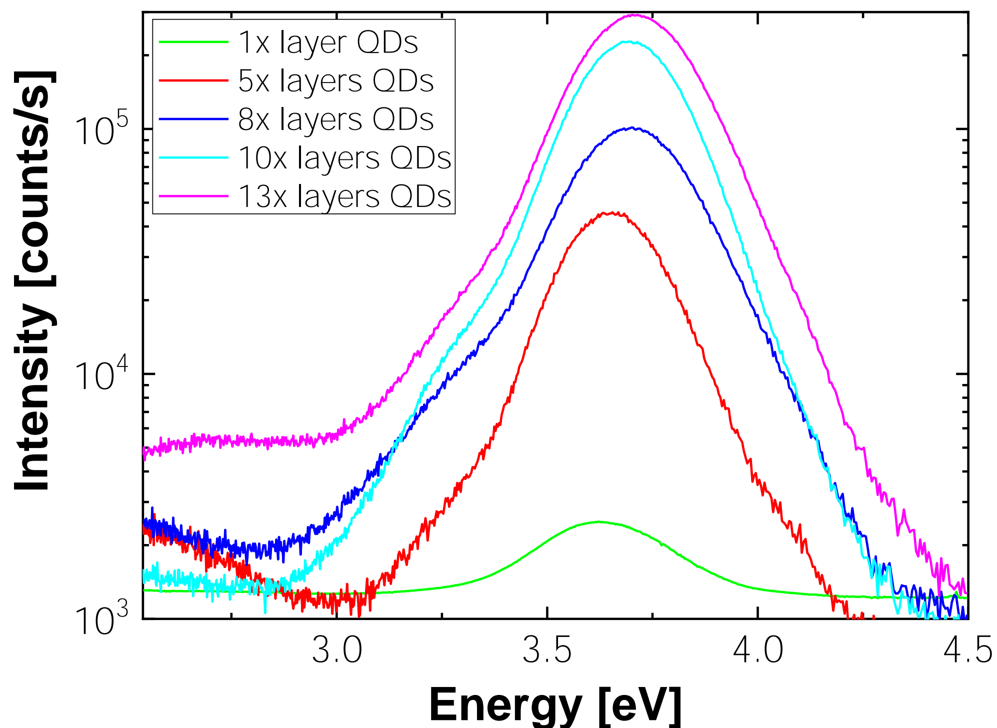

Figure 4-24: PL intensity (in logarithmic scale) versus the emission energy of the stacked QDs with 1, 5, 8, 10 and 13 layers of QDs. The measurements are done at room temperature. The emission energy and the intensity increase with increasing number of stacks.

In principal, the spectra show an increase of intensity with increasing number of stacked layers. Starting with the sample with one layer of QDs, as a reference sample, it shows an emission energy of 3.63 eV with a FWHM of 340 meV. As already described in chapter 4.3, this relatively wide range represents a superposition of Gaussian-shaped emission bands of many individual QDs [78]. Due to the large spot size of the laser, QDs with different sizes are measured in this spectrum, which results in this broad emission peak. Compared to the other samples, where many layers of QDs exist, the FWHM is relatively constant. It ranges between 290 and 340 meV. This indicates that the varying of the QD size in all layers is very constant, too. This is in contrast to other material systems like the hexagonal GaN QDs [73] or InAs QDs, where a decrease of the FWHM is observed with increasing number of stacked QD layers. This decrease is explained by a homogenization of the island distribution with increasing number of stacks. In our case, a homogenization is not observed, as verified with AFM measurements, so a narrowing of the FWHM was not expected at all.

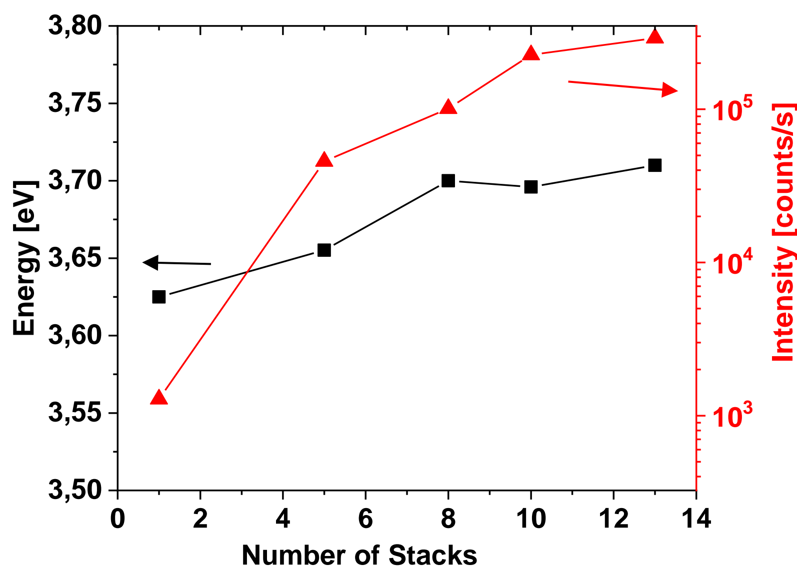

Figure 4-25: Emission energy and integrated intensity (semilogarithmic scale) as a function of the number of stacks. In both cases, an increase with increasing number of stacks is observable.

Whereas the PL emission energy shows a clear tendency to higher energies with increasing number of QD layers. Figure 4-25 shows the energy of the peak emission as a function of the number of stacked QD layers. The energy shows a blueshift of emission energy with increasing number of stacked QD layers from 3.59 eV to 3.71 eV. The main confining parameter in the c-GaN QDs is the QD height [20]. AFM measurements show that the QD diameter is relatively constant, concluding that the blueshift of emission

energy is due to a decrease of the QD height. In most stacking experiments the PL emission energy shifts to lower energies, for example in the InAs system, where it is attributed to a coupling between the dots due to a thin spacer layer [2]. Strain related effects in the c-GaN QDs would also lead to redshift of emission energy, because the QDs are compressively strained on the c-AlN layer. This is in contradiction to the observations shown in Figure 4-25. Therefore, the influence of the decrease of the QD height is significantly higher than the influence of strain related effects. A decrease of the QD height of one to two ML is expected.

In addition, the integrated intensity in logarithmic scale is plotted against the number of stacked QD layers. It shows an almost linear dependence. The intensity of the sample with five layers is approximately 40 times as high as that of the sample with one layer of QDs. The sample with 10 layers of QDs shows a 200 times higher intensity compared to the sample with one QD layer. Comparing the stacked c-GaN QDs to stacked h-GaN QDs, the h-GaN QDs show a drastic increase from the sample with one QD layer to the sample with 3 QD layers, afterwards the intensity becomes almost stable [79]. This behavior is explained by an increasing uniformity of the QD size with increasing number of stacked QD layers. Up to three QD layers they observed that the emission of large-sized QDs becomes dominant, whereas the formation of small QDs is drastically reduced. In this work, it was shown that the size distribution of the c-GaN QDs is constant and independent of the number of stacked QD layers. In conclusion, this independency is the reason for the linear increase of the PL peak intensity. The influence of possible, available surface or interface properties or defects in the c-AlN, whose existence was already proven with the help of TEM images, on the increase of the PL intensity has to be investigated in the future. One possibility to exclude those impacts is to realize a sample series with a much thicker c-AlN top layer. Fundamentally, the increasing PL intensity shows that QDs are excited in each layer and an increased number of QDs contribute to the PL signal.

4.6 Summary of the Growth of c-AlN and c-GaN

Cubic-GaN QDs of high quality embedded in a c-AlN are realized successfully with MBE employing the SK growth mode. Single QD layers as well as QD layers with up to 20 layers of QDs are realized. The investigation of thick c-AlN layers shows that a smooth surface is only realized with thin layers below 100 nm thickness. For the growth of a single QD layer a buffer and top layer thickness of 30 nm each is chosen. The varying QD size, realized by deposition times between 13 and 30 s, shows a decrease of emission energy with increasing deposition times. Which was expected, since the main confining parameter in our QDs is the QD height. Adding a second layer of QDs to the sample structure, a structural and electrical coupling of the QDs can be observed if the c-AlN spacer layer is thin enough. The structural coupling leads to a vertical alignment of the QDs if no stacking faults are present. The electrical coupling is verified due to the absence of the peak for the high energy QDs in the PL measurements. TEM measurements are performed to show the vertical aligned QDs. The stacking of up to 13 layers of QDs results in an increase of the QD emission energy with increasing number of stacked layers. In addition an increase of the emission intensity of the peak energy with increasing number of stacked layers is observed. This indicates that QDs are excited in each layer and an increased number of QDs contribute to the PL signal with increasing number of stacks.

5 Nextnano++ Simulations of c-GaN QDs

Simulations, using nextnano++, a commercial available self-consistent Schrödinger-Poisson solver [80], are realized. Nextnano++ uses a numerical method to minimize the strain energy of the system in order to determine the actual band structure influenced by strain. Then, in a second step, the Schrödinger equation and Poisson equation for electrons and holes in the conduction and valence bands at the important points of the Brillouin zone are also solved numerically and the energetic position of the charge carriers as well as the wave functions and the residence probabilities of the charge carriers are calculated. The program requires the material parameters of the used materials c-AlN and c-GaN as starting point of the simulations. Most of the parameters are included in the scope of delivery of the software and have been taken from relevant publications, especially [81]. However, some parameters have been obtained from other sources and replaced in the parameter list of the software. A parameter list with the used parameters can be found in chapter 9.7.

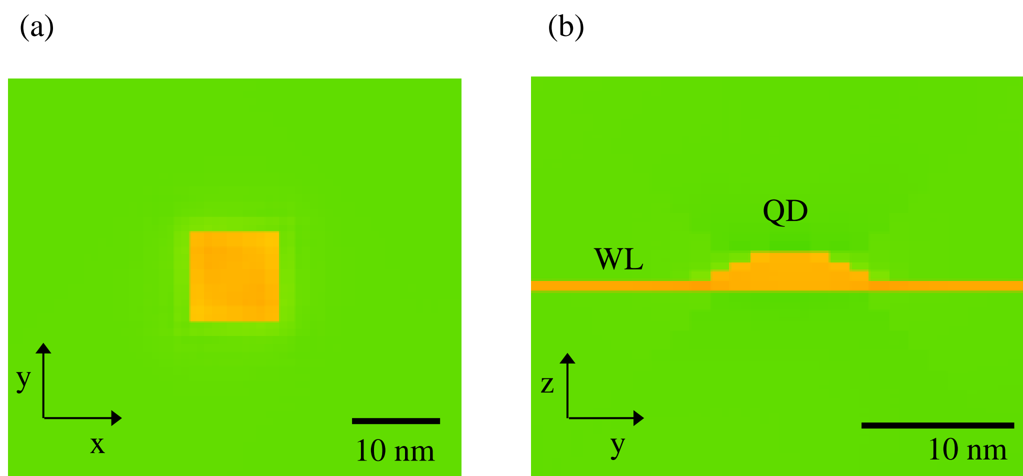

Figure 5-1: Shape of the QDs used for the simulations with nextnano++. The cross section of the bottom of the pyramid is a 10 x 10 nm² square in the x-y-coordinate system (a). In the y-z-direction the QD has a truncated pyramidal shape (b). The height of the QD is 2 nm. The wetting layer is also visible and the thickness amounts to 0.7 nm.

In this work the software is used to investigate the electronic properties of the QDs and to validate the experimental data shown in chapter 4.3. Additionally, the influence of QD pairs is investigated theoretically. For both simulations the first step needed for the simulations is the implementation of the size, shape and chemical composition of the 3D QD structure. As already explained, the c-GaN QDs are assumed to have a truncated pyramidal shape, which is theoretically used by Fonoberov and Balandin [20] in

chapter 2.2 and experimentally proven with the help of TEM images in chapter 4.5. The square basis is oriented in the (001) direction and the side facets of the pyramid are parallel to the (111) direction.

Figure 5-1 shows the orientation of one single QD in the simulation program. The c-GaN QD and the WL are displayed in yellow. The surrounding area, which consists of c-AlN, is colored green. Figure 5-1 (a) shows a top view of the QD. For a better visualization, the WL was omitted here. The figure shows the bottom of the pyramid which is oriented in x-y-direction and has a diameter of 10 nm. The truncated pyramidal shape extends in the y-z-coordinate system, shown in Figure 5-1 (b). A wetting layer is implemented with a thickness of 0.7 nm, which corresponds to approximately 3 MLs. The WL thickness is determined in chapter 4.5, too, with the help of TEM measurements with atomic resolution. The QD width in this figure is 10 nm and the QD height is 2 nm, resulting in an aspect ratio of 1:5. For the simulations, QD diameters of 5, 10 and 15 nm are used and the QD height is varied from 0.225 nm to 3 nm to cover a wide range of QD sizes. The lower number represents exactly one ML of c-GaN. The WL thickness is constant for all simulations and is not included in the QD height mentioned before. The parameters used for the simulations are shown in Table 2. Wecker et al. [82] also used these parameters for the simulations of c-GaN single and multi-quantum wells to estimate the interband and intraband transitions with nextnano^3. The results of the simulations fit very well to the experimental data. In this work comparable results are expected by using the same parameter set. The additional parameters, which are necessary for the eight-band k·p theory are taken from the material database of nextnano++, where Vurgaftman et al. [81] is the main source.

After the definition of the QDs and strain calculations, nextnano++ continues with solving the Schrödinger and Poisson equations. The electron and hole wave functions are received using the eight-band k·p model. For the calculations room temperature is presumed because the experimental measurements of the emission energies are realized at room temperature as well. The transition energies of one single QD layer are calculated. Both, the height and the diameter were varied. In addition, the influence of the thickness of the spacer layer could be determined with the help of strain calculations of two stacked layers of QDs.

5.1 Transition Energy of QDs

In order to verify the results from chapter 4.3, simulations were performed with the help of nextnano++. As described above, the Schrödinger equation and the Poisson equation have to be solved numerically. The simulations are realized for QD diameters of 5, 10 and 15 nm. In Figure 5-2 the results of the calculations for the conduction band minimum and valence band maximum as a function of the QD height are shown. Due to the broad emission peaks in the experimental PL measurements, shown in Figure 4-10, these selected diameters reflect well the size distribution. In the result it is visible, that the difference between hole and electron energy levels change only slightly with relatively significant increase of the QD height from 0.225 nm to 3 nm. This can be explained by the absence of the piezoelectric field in the cubic phase. Compared to wurtzide GaN, where a piezoelectric potential is present, the high QDs show much smaller energy differences than the small QDs, because the piezoelectric potential increases linearly with increasing QD height [20]. It is also visible that the band edges are shifted to higher energies with increasing QD width.

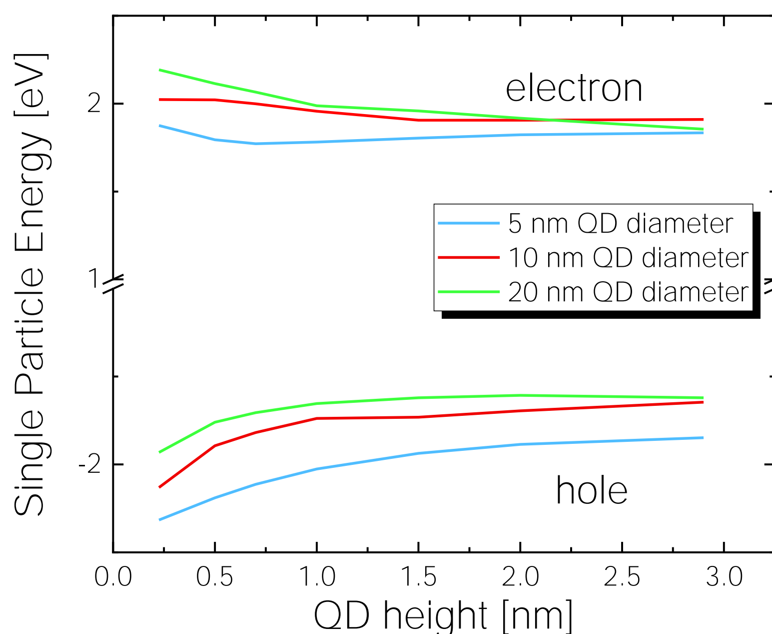

Figure 5-2: Results of the eight-band k·p model of the conduction band minimum and valence band maximum as a function of the QD height. The diameter of the QD is varied between 5 and 20 nm, because of the broadening of the size.

In Figure 5-3 the transition energies plotted versus the QD height are presented. According to the absence of the piezoelectric field, not only a low decrease of the conduction and valence band difference is observable, but also an influence of the emission energy is observable. The behavior of the emission energy is mainly affected by the deformation potential and confinement [20]. It is important to mention at this point that the c-GaN bulk energy gap is at 3.23 eV, which is significantly lower compared to the c-GaN QDs. Contrary to this, the h-GaN emission energy drops below the bulk energy due to the spontaneous polarization [20]. Whereas in c-GaN QDs the emission energy is always higher than the bandgap.

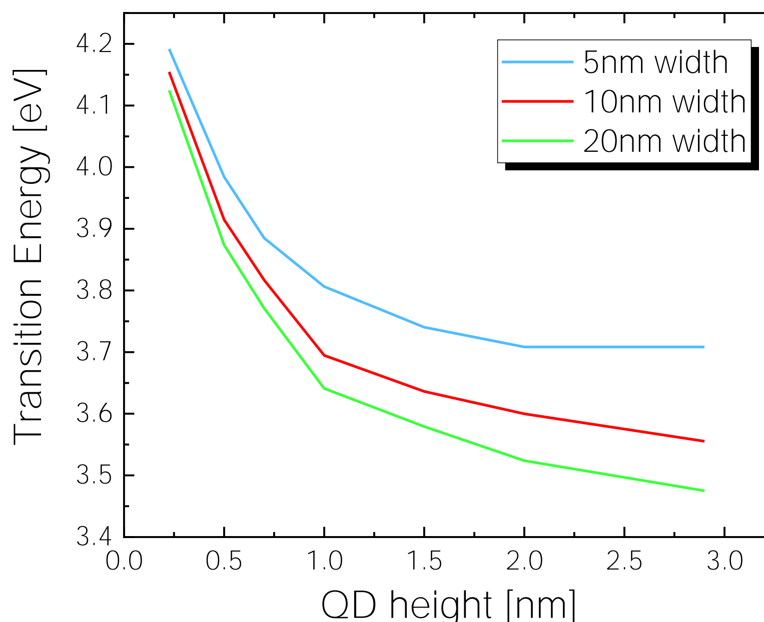

Figure 5-3: Results of the eight band k·p model of the transition energy as a function of the QD height. The diameter of the QD is varied between 5 and 20 nm, because of the broadening of the size.

Comparing these results to the experimental data, it is necessary to explain the difference between QD height and the GaN coverage. During the SK process the deposited c-GaN amount transforms into the WL, which has a thickness of about 0.7 nm, and into the c-GaN QDs. The height of the QD is higher than the deposited amount of c-GaN. In Figure 5-4 the black squares represent the measured QD emission energy for different QD deposition times taken from Figure 4-10. In this diagram not the deposition time is plotted, but the GaN coverage. The GaN coverage is like depositing the equivalent of 0.9 nm, corresponding to 4 MLs, of a planar c-GaN layer. This planar layer is the

thickness measured before the WL and QDs are formed. Additionally in Figure 5-4 the simulated results of the QD emission energy in dependence of the QD height are plotted taken from Figure 5-3. Two different QD diameters are plotted. The red curve represents the smaller QDs with a width of 10 nm and the green curve shows the emission energy for QDs with a width of 20 nm. The experimental data fits very well to the simulations. The shape of the curves are nearly similar.

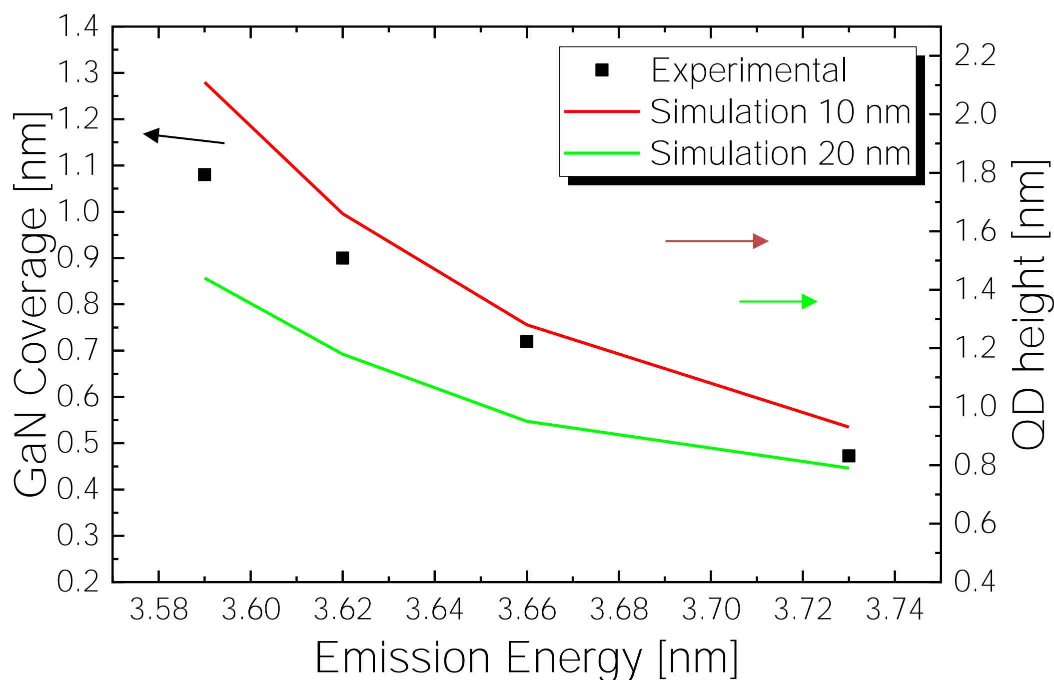

Figure 5-4: Emission energy as a function of the GaN coverage for the experimental results and the QD height for the simulations for a QD width of 10 and 20 nm.

5.2 Mechanical Coupling of QD Pairs

Strain calculations were carried out to estimate the influence of the spacer layer thickness. When stacking QDs a vertical alignment of the QDs can occur as shown experimentally in chapter 4.5. QDs in a second layer of QDs accumulate mainly in the areas of the QD below. This happens due to strain in the lower layer. In order to be able to determine up to what distance these strains are effective, simulations were carried out with the help of nextnano++.

To investigate strain and its influence on QD layers above, two QD layers were stacked on top of each other. As already described in chapter 5, the dimensions of the two QD layers are described first. The thickness of the spacer layer was varied. This allows a mechanical coupling between the QD layers to be demonstrated. In the software nextnano++ the calculation of the strain of a layer takes place directly as the next step, since, as already mentioned above, it is the basis for creating the band model.

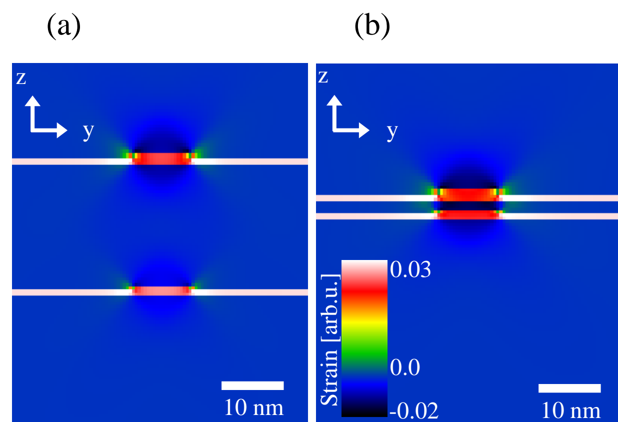

Figure 5-5: Strain simulations in growth direction for QD pairs similar to chapter 5 with (a) a spacer layer thickness of 20 nm and (b) a spacer layer thickness of 4 nm.

In Figure 5-5 the results are shown calculated for the component of the strain tensor in the x-y-plane in growth direction (z-direction) for a spacer layer thickness of 20 and 2 nm, respectively. These values are chosen in comparison with the experimental data of chapter 4.5. For both spacer layer thicknesses the QD is compressively strained, visible from the red color. Due to the strain of the QD, the surrounding is influenced, too. Looking at the simulation results, the surrounding of the QDs is dark blue, which means there is tensile strain. In Figure 5-5 (a) the spacer layer has a thickness of 20 nm. But the tensile strained surrounding of the QD is spatially extended 5 nm below and 5 nm above the QD. So the tensile strained areas do not influence each other. It is worth noting, that for the interest of clear presentation and better understanding the QDs are arranged on top of each other. Due to the thick spacer layer no vertical alignment occurs in this sample.

Decreasing the spacer layer thickness (see Figure 5-5 (b)), the tensile strained areas in the surrounding of the LQD and UQD merge, resulting in only one large tensile strained area. This strain induces the vertical alignment of the QDs. This is comparable to the results of the TEM measurements shown in Figure 4-22.

5.3 Summary of nextnano++ Simulations

In this chapter, the software nextnano++ is used to gain further understanding of QDs. In the first part, the transition energies of a single layer of QDs are examined. The simulations show a decrease of the QD height with increasing emission energy. This is similar to the experimentally determined results. The slop of both curves is the same.

In the second part, the strain of the QD and its surrounding is investigated. A second layer is implemented and the thickness of the spacer layer varied to prove the mechanical coupling. It could be shown that the surrounding of the QD is tensile strained. If now the tensile strained areas of the upper and lower QD are brought together by a reduction of the spacer layer thickness, one large tensile strained area results. This tensile strained area could already be observed in TEM measurements in chapter 4.5 and leads to a vertical alignment of the QDs.

6 Photonic Crystal Membranes

Photonic crystals (PC) are in the focus of interest in the field of light-emitting diodes (LEDs) to enhance the external efficiency [83]. They consist of periodic lattices with alternating refractive index resulting in a diffraction of the propagating light. At certain frequencies propagating electromagnetic modes does not exist which leads to a photonic band gap (PBG).

An additional refractive index contrast in the vertical direction between the active layer and air leads to a confinement of light in all three dimensions. This refractive index contrast is realized by an undercut of the active layer. Such an underetched PC is called PC membrane or air-bridge type. Strong Purcell enhancement can be reached due to high Q factors and small mode volumes. The main advantage compared to a 3D crystal is that the manufacturing process is much easier. The realization of 3D crystal membranes is a technological challenge. Whereas the realization of 2D PC membranes employs common process techniques like EBL, RIE and PECVD.

The optical cavity in the active layer is realized by a controlled defect in the PC. For other material systems very high quality factors for one-dimensional photonic crystal nanobeam cavities embedding h-GaN/AlN quantum dots are observed [84].

Theoretical calculations of different arrangements of the air holes have shown that air holes arranged like a honeycomb [85,86] or like atoms in a graphite [87,88] result in the largest possible photonic band gap (PBG), because small regions of a material with a high refractive index are surrounded by large areas of air. As a result, a small air filling factor occurs [34].

In this work, the basis of the PC membranes forms the QD sample of chapter 4.3 consisting of one single QD layer embedded between two c-AlN layers. The used material system provides a short emission wavelength. As described in chapter 2.3.3, the dimensions of the PC must be in the order of the optical wavelength. Therefore, the dimensions of the PC must be very small which is challenging.

The following chapter includes 2D photonic crystal membranes, already mentioned in the basics in chapter 2.3. At first, detailed information about each step of the fabrication procedure is given. This also includes the explanation of the used setups and the mention of the parameters for each process step. Afterwards, theoretical calculations with the commercially available time domain solver Computer Simulation Technology (CST) -Microwave Studio are shown to determine the optimal dimensions of the PC membrane. Additionally, the positions of the modes are calculated. Finally, the PC membranes are optically characterized by μ-PL measurements.

6.1 Fabrication of PC Membranes

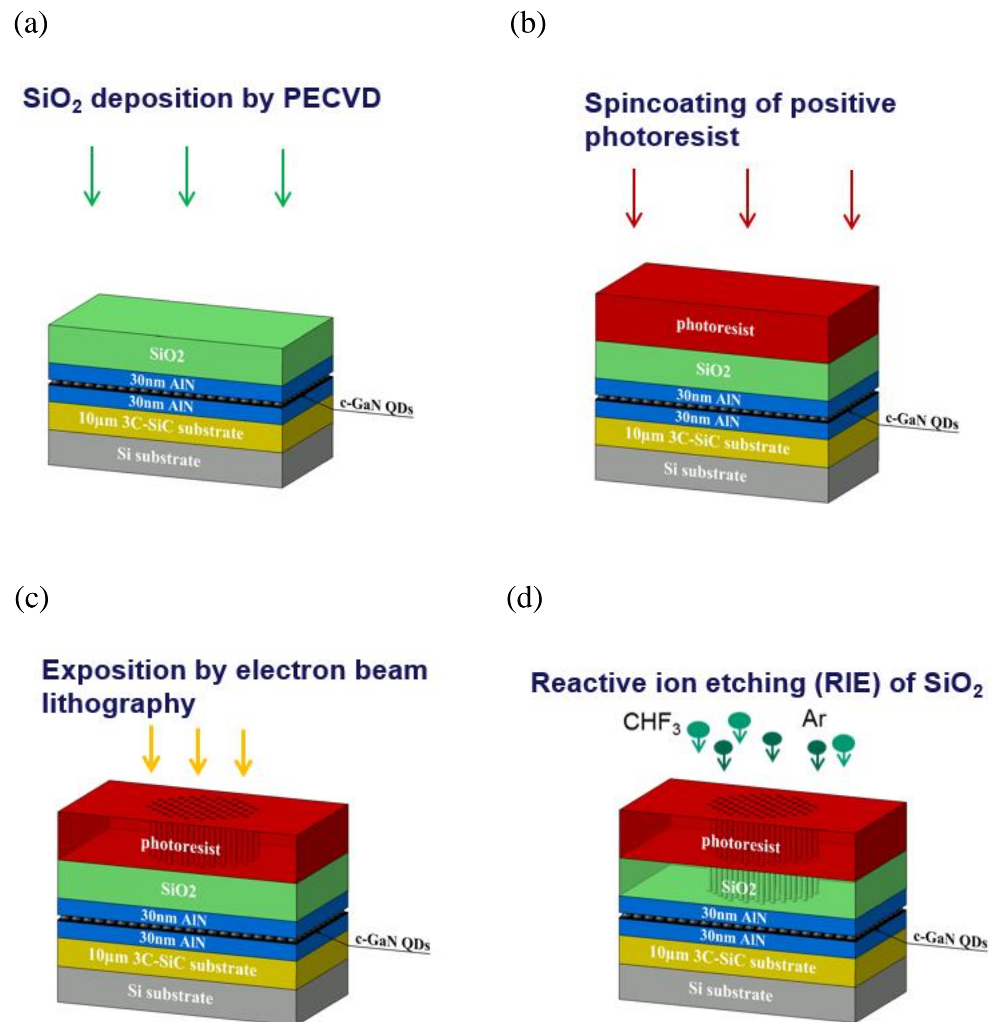

Figure 6-1: First four steps of the fabrication process of the PC membrane. Each fabrication step is shown including the deposition of SiO_2 as hard mask with PECVD (a), spin coating of positive photoresist (b), patterning with electron-beam lithography (c) and RIE etching of SiO_2 (d).

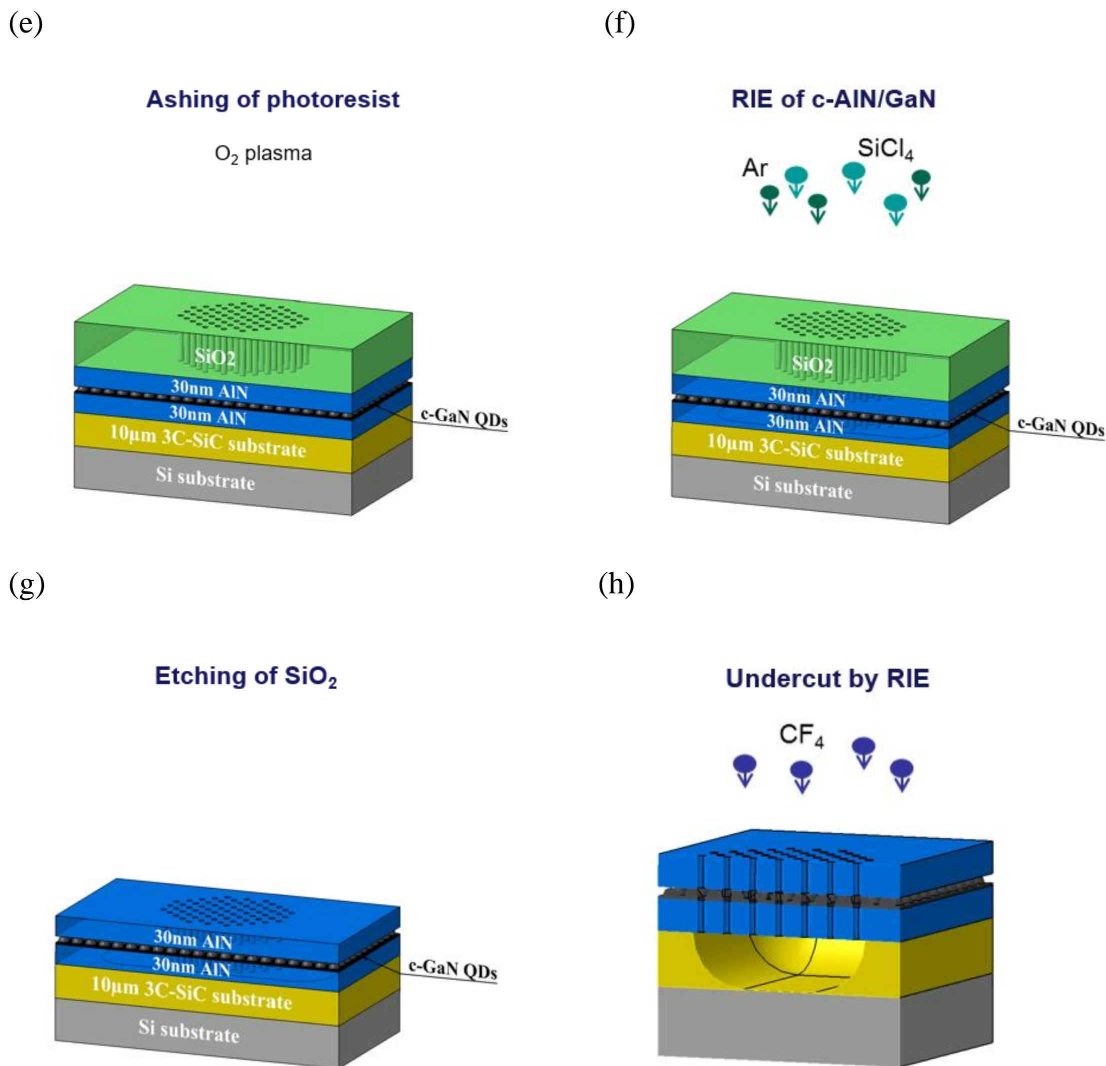

Figure 6-2: Second four steps of the fabrication process of the PC membrane. Each fabrication step is shown including ashing of the photoresist (e), etching of the active layer (f), removing the hard mask (g) and realization of the undercut by RIE (h).

A top down process is developed to create the free-standing membrane. The first step of the fabrication of the PC membrane is the deposition of a SiO_2 hard mask employing plasma enhanced chemical vapor deposition (PECVD) with an Oxford Plasmalab 80 Plus (Figure 6-1 (a)). Since the photoresist will not resist the following etching steps, a hard mask is usually used. The choice of the material required for this mask depends on the active layer. It is important that the hard mask can be removed easily after transferring the pattern in the active layer without destroying it. For the deposition of SiO_2, silane (SiH_4) and nitrous oxide (N_2O) are used as precursors with a flux of 400 sccm. The chamber pressure is 1 Torr, the radiofrequency power (RF power) is 20 W and the

substrate holder is at 300°C. A growth rate of 73 nm per minute is reached. To ensure that the hard mask withstand the patterning transfer in the active layer a thickness of 80 nm is realized. After the hard mask deposition, the sample is cleaned with acetone, isopropanol and DI-water and placed on a hot plate at a temperature of 100°C. Through the heat treatment, the photoresist, which is spin coated in the next step, adheres better on the sample surface. Positive photoresist (ZEP520A) is used and spin coated with a Süss MicroTec LabSpin 6/8 with a rotation speed of 6000 rpm, an acceleration of 1500 $\frac{1}{s}$ and a duration of 60 s, resulting in a thickness of 380 nm (Figure 6-1 (b)).

Afterwards the resist is baked out for 2:30 min at 180°C. This photoresist is sensitive especially to electron beams. Although electron-beam lithography (EBL) is much slower compared to optical lithography on the one hand, on the other, the edges are sharper, and it is possible to easily change the structure for each sample. A schematic mask for the electron-beam lithography is shown in Figure 6-3. One element consists of 9 PC and a description of the patterned PCs. The dose within those 9 PCs is varied to find out the optimal patterning parameters. Up to 200 structures of these 9 PC packages are realized on one sample. They consist of different ratios of radius to lattice constant and of different cavity sizes. In this case a L3 cavity is shown as an example.

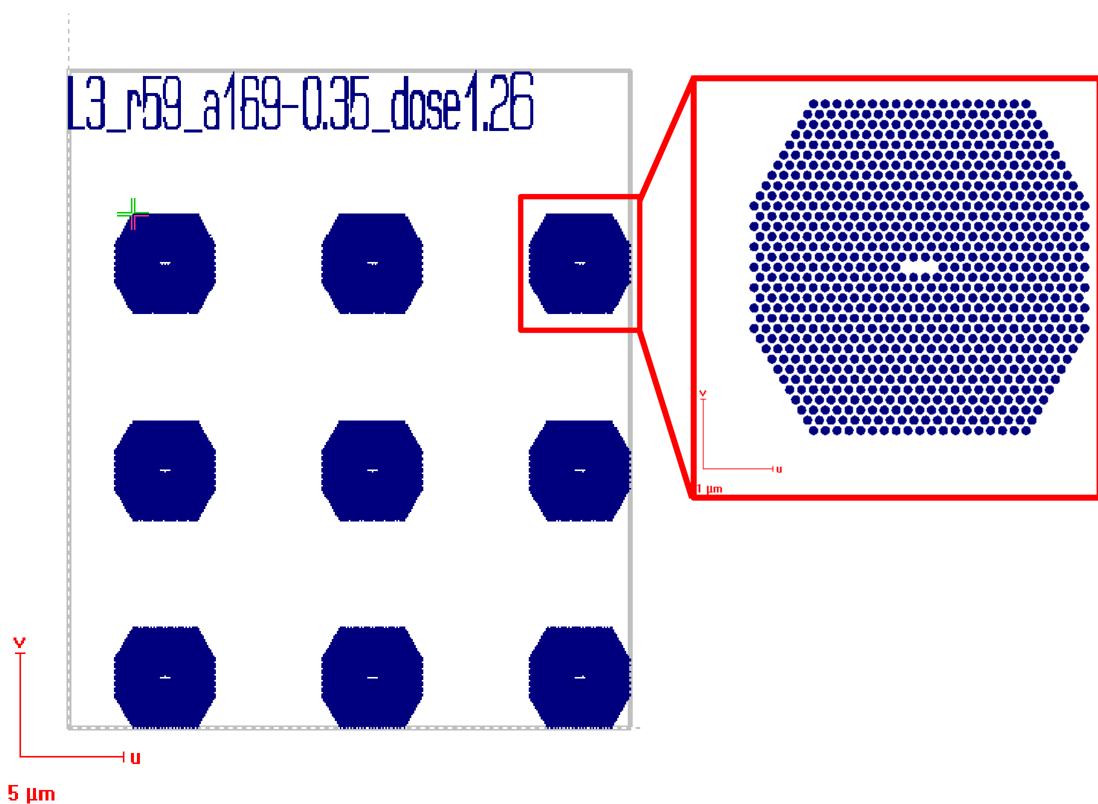

Figure 6-3: Mask for EBL of one element and a close-up of one PC out of this element. Nine PCs are arranged in one pattern. In this case L3 cavities with a radius of r = 59 nm, lattice constant of a = 169 nm and a dose factor of 1.26 are shown.

The optimal parameters to obtain a hole diameter as round as possible and a homogeneous hole size depend on many different factors. The interaction of the r/a-ratio and the dose factor play an important role. With a large r/a-ratio, the dose must be chosen accordingly small to prevent, among other things, the proximity effect. Ratios from 0.3 to 0.37 in 0.1 steps are realized for H1, H7, H19, L3, L5, L7, L9 and L15 cavities. Different r/a-ratios by constant slab thicknesses lead to a tuning of the cavity-mode energies and the size of the PBG changes. In addition, the dose depends on the size of the cavity. The preset dose is constant at 65 $\frac{\mu C}{cm^2}$. With the help of dose factors, the dose can be set for each individual structure or even for each individual air hole. The optimal values for the radius, the lattice constant, the resulting r/a-ratio and the resulting dose, calculated from the preset dose multiplied by the dose factor, are shown in Table 6 for each individual cavity design. It should be noted that the analysis was carried out using a purely structural analysis only. All parameters were varied and then evaluated with the help of SEM images. An assessment of the optical activity was not made.

Table 6: Optimized parameters for different PC cavities. The values are determined using SEM images. The criteria are as round holes as possible, no undesirable defects and a constant air hole radius.

	Optimal Radius [nm]	**Optimal Lattice Constant [nm]**	**Optimal r/a-ratio**	**Optimal Dose Factor $\left[\frac{\mu C}{cm^2}\right]$**
H1	59	169	0.35	82
H7	68	192	0.35	76.38
H19	54	169	0.32	85.8
L3	59	169	0.35	81.9
L5	54	169	0.32	78
L7	68	192	0.35	74.1
L9	68	192	0.35	72.15
L15	51	169	0.30	89.7

In the following, the individual steps for fabricating a PC membrane are explained in more detail using a L3 cavity. This has a radius of r = 59 nm and a lattice constant of a = 169 nm, which leads to a r/a-ratio of 0.35. The preset dose is 65 $\frac{\mu C}{cm^2}$. In this case the dose factor is 1.26 leading to a final dose of 81.9 $\frac{\mu C}{cm^2}$.

In the used EBL process, the aperture is small with 7.5 µm and the voltage of the electron gun is 25 kV. The beam current is measured by a Faraday cup. The selection of the aperture size, beam current and the area dwell time enables an exposure of the resist by minimizing the impact of backscattered electrons (proximity effect). After the exposure of the photoresist (Figure 6-1 (c)), the resist is developed with the help of n-Amylacetat for 60 s. Since a positive photoresist is used, the unexposed parts of the sample remain. For the stop bath the sample is dipped in isopropanol for 15 s and subsequently cleaned with DI-water. The pattern is then transferred to the hard mask by reactive ion etching (RIE) using CHF_3 with 20 sccm and Ar with 20 sccm (Figure 6-1 (d)), respectively. The pressure is 30 mTorr and the RF power is 25 W. The etching rate is 8 $\frac{nm}{min}$, so the etching time is 10 min. The CHF_3 in this process stabilizes the sidewalls which leads to an anisotropic etching. In the subsequent step, the photoresist is removed using an oxygen plasma (Figure 6-2 (e)). An oxygen flux of 47.5 sccm is used with a pressure of 50 mTorr, a RF power of 10 W and an inductively coupled plasma (ICP) power of 200 W for 15 min. To transfer the pattern into the active layer RIE is used again applying $SiCl_4$ with 4.5 sccm and Ar with 4.5 sccm as process gases (Figure 6-2 (f)) for a duration of 90 s, leading to an etching rate of 1 $\frac{nm}{min}$. The pressure is 10 mTorr, the RF power is 150 W and the ICP power is 60 W. Steps (d) – (f) are performed in an Oxford Plasmalab 100 etching system. In order not to contaminate the sample unnecessarily, as many steps as possible have been carried out without interruption. The etching of the hard mask, the removal of the photoresist and the etching of the active layer are realized without removing the sample from the system. Only during the parameter determination and for illustrative purposes the sample is removed after each step and examined by SEM. Subsequently, the hard mask is removed (Figure 6-2 (g)) by using a buffered oxide etching (BOE) solution for 8 min (exact composition already described in chapter 4.1).

Finally, the AlN/GaN is underetched to ensure a minimization of the outcoming light (Figure 6-2 (h)). Conventionally, this step is realized by wet chemical etching steps. Unfortunately, the material selectivity between 3C-SiC and c-AlN/GaN is low, so the active layer cannot resist during a wet etching process. Therefore, a dry chemical etching process has been developed using the Oxford Plasmalab 80 Plus. A tetrafluoromethane (CF_4) flux of 90 sccm at a pressure of 1 Torr, a RF power of 200 W and a strike power of 60 W at a substrate holder temperature of 375°C is used.

To be able to report every single step and to evaluate the performance of the etching process, SEM images are performed. In Figure 6-4 SEM images of the last three fabrication steps are shown as a top view as well as a close-up of the cavity and a cross-section of the PC membrane, respectively. This cavity is a L3 cavity with a radius of d = 58 nm (± 1 nm) and a lattice constant of a = 170 nm (± 2 nm). The top view of the complete PC membrane shows that the hole size is relatively constant across the whole cavity. A decrease of 3-5 nm from the center to the border of the PC is observable but only for the outer holes, which is attributable to the proximity effect during EBL, which is already described in section 3.2.4. The close-up of the center of the PC shows that the air holes have a quiet circular shape. A cross-section of the PC membrane after the last etching step is realized to demonstrate the suspended membrane. In this image the sample is mounted on the sample holder with a tilt of 82° with respect to the x-y-plain. The etched 3C-SiC shows a sawtooth-like profile, which leads to non-constant under etching depth of 150 nm to 300 nm. We assume that this depth and the high roughness ensure a decoupling of the optical mode from the substrate.

The surface roughness of the AlN layer is measured by atomic force microscopy (AFM) measurements. A 10 x 10 μm^2 field is measured. An rms surface roughness of 8.4 nm is determined, which originates mainly from the last etching step by RIE.

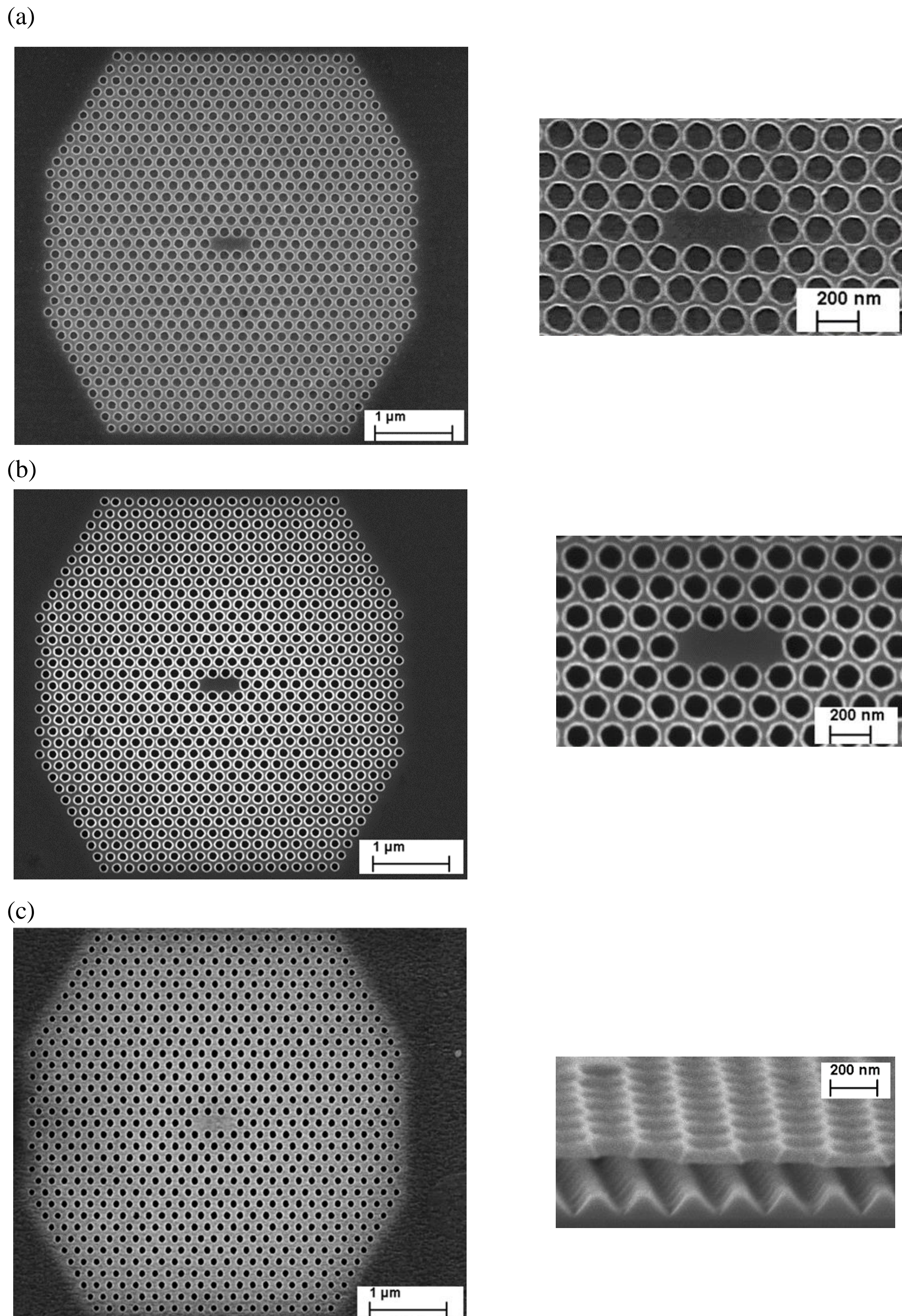

Figure 6-4: SEM images of the last three steps of the fabrication process of the PC membranes, which correspond to images (f), (g) and (h) in Figure 6-1 and Figure 6-2. A top view of a L3-cavity is shown as well as a close-up of the defect of the PC in (a) and (b) and a cross-section of the free-standing membrane in (c).

6.2 CST-Simulation of Modes

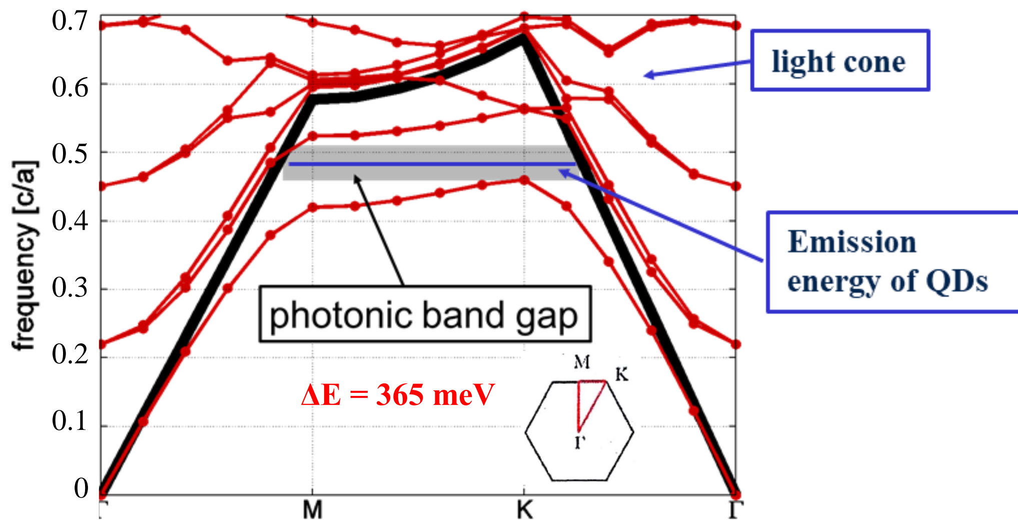

Figure 6-5: Photonic band structure of TE-like modes with slab thicknesses h = 62 nm, lattice constant a = 170 nm and air hole radius r = 108.8 nm. The black line indicates the light cone. The resulting PBG is shaded in grey color. The emission of the QDs is assumed to lie in the middle of the PBG.

Simulations with the commercially available time domain solver CST Microwave Studio are realized to estimate the energetic position of the modes for different r/a-ratios and various slab thicknesses for a triangular array of air holes from the group of Jens Förstner. The software package MIT Photonic-Bands computes definite-frequency eigenstates of the Maxwell equations ((2-2), (2-3), (2-4) (2-5)) to get the band structures and electromagnetic modes of periodic structures. The program uses fully-vectorial and 3D frequency domain methods. It is suggested that the emission energy of the QDs in the active layer is E = 3.6 eV and that this emission energy lies precisely in the center of the photonic band gap. Figure 6-5 and Figure 6-6 show the dispersion relation of a L3 cavity. The slab thickness is assumed to be h = 62 nm, the lattice constant is a = 170 nm and the diameter of the air holes is d = 108.8 nm. The black line represents the light cone. Below the light cone the guided modes which are localized to the plane slab are plotted. Outside the cone the states which are extended infinitely in the region outside the slab are shown. The blue line shows the emission energy of the QDs, which lies in the middle of the PBG and therefore leads to higher Purcell factors. For TE-like modes (red curves) a photonic band gap (PBG) exists over all symmetry points below the light cone. The photonic band gap extends from f = 0.46 c/a to f = 0.51 c/a with c the velocity of the light. So, this frequency corresponds to energies from E = 3.357 eV to E = 3.722 eV leading to a photonic band gap of 365 meV. This PBG is one of the largest one obtained in the simulations. A further increase of the size of the PBG is possible with a decrease of the

thickness of the slab [89]. However, a thinner slab has many disadvantages. On the one hand the surface would be rougher due to the thinner top layer of c-AlN and on the other hand due to the undercut of the active layer the membrane would be more instable. For TE-like modes no PBG occurs as shown in Figure 6-6.

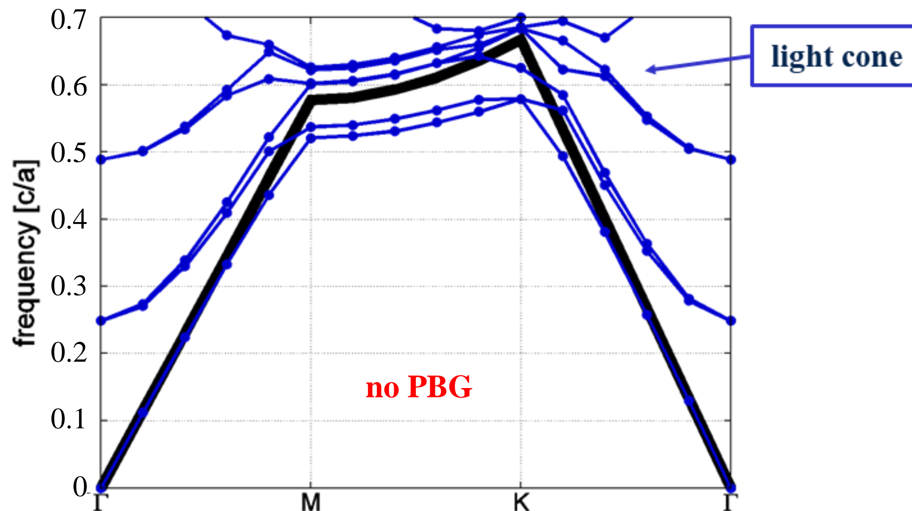

Figure 6-6: Photonic band structure of TM-like modes with slab thicknesses h = 62 nm, lattice constant a = 170 nm and air hole diameter d = 108.8 nm. The black line indicates the light cone. No PBG is observable.

The simulations are realized for various parameters to show that the parameters have a huge impact on the size of the PBG. Table 7 shows simulations for different slab thicknesses. The lattice constant and hole diameter have been modified so that the largest possible photonic band gap is achieved. So, these three parameters are used for the simulations of the photonic band structure. For each PC from 1 to 5 the TE-like modes are plotted and the frequency and the energy, respectively, of the minimum and the maximum of the band gap (BG) are investigated. So PBG thicknesses from 218 meV to 356 meV are achieved. PC1 responds to the photonic band structure of Figure 6-5, where the largest possible PBG is realized. The thickness of 62 nm fits very well to the samples shown in chapter 4.3, where c-GaN QDs were embedded in a 60 nm thick c-AlN matrix. Unfortunately, the hole diameter in this case is very small. However, chapter 6.1 showed that hole diameters of 106±2 nm are achieved. Decreasing of the slab thickness to 51.5 nm (PC2) or 43.4 nm (PC3) leads to PGB of only 218 meV and 251 nm, respectively. Increasing of the hole size with consistent slab thickness of 62 nm (PC4) also results in a smaller PBG size. Changing both (PC5), of course, the PBG thickness does not increase as well.

Table 7: Results of the simulations for different PCs. The lattice constant a, hole diameter d and slab thickness t are varied. The minimum and maximum of the bandgap are calculated with the help of CST Microwave Studio to determine the resulting photonic band gap thickness.

	PC1	PC2	PC3	PC4	PC5
Slab thickness t [nm]	62	51.1	43.3	62	46.5
Lattice constant a [nm]	170	170	173	176	186
Hole diameter d [nm]	108.8	111	112	141	149
r/a	0.32	0.326	0.324	0.4	0.4
Energy BG min [eV]	3.36	3.49	3.47	3.45	3.47
Energy BG max [eV]	3.72	3.71	3.73	3.73	3.74
PBG thickness [meV]	365	218	251	286	267

As an example, Figure 6-7 shows the result of the simulations for the photonic band structure of PC5. It has a large lattice constant (a = 186 nm) and a large hole diameter (d = 149 nm). The band gap extends over a range from E = 3.47 eV to E = 3.74 eV, resulting in a photonic band gap of 267 meV. Compared to the already shown simulation of PC1 in Figure 6-5, this is much smaller.

Additionally, a simulation is realized, where the active layer is directly on the substrate. This means that the underetching step is has been omitted and the active layer is now applied directly to the substrate. Remember: underetching leads to an increased number of outcoming light due the lower reflectivity. The refractive index contrast between c-AlN and air is higher than between c-AlN and 3C-SiC, which leads to a higher reflectivity at the interface between c-AlN and air.

The slab thickness is increased with 276 nm. The disadvantage of such a thick layer, however, is a significantly higher roughness of the layer. The results of chapter 4.2, in which the c-AlN layer thickness was varied, confirm this. This increased roughness leads to an inaccuracy during EBL and thus to a reduction in the quality of the PC. The advantage of this thick layer is that a higher slab thickness normally leads to a larger PBG. Accordingly, the air hole diameter with d = 149 nm and the lattice constant with a = 186 nm, corresponding to a r/a-ratio of 0.4, have also been adapted. Anyway, no PBG is visible.

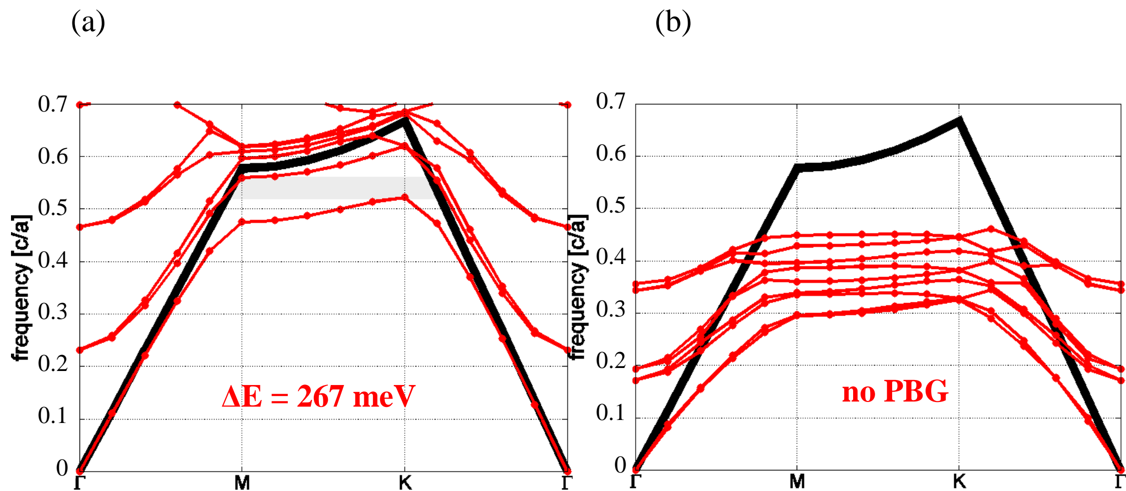

Figure 6-7: Photonic band structure of TE-like modes with the following features of PC5 (a) with slab thickness h = 46.5 nm, lattice constant a = 186 nm, air hole diameter d = 149 nm and a PC with the active layer directly on top of the substrate (b) with lattice constant a = 344 nm, air hole diameter d = 276 nm and slab thickness h = 172 nm.

Additionally, the electric field distribution and the mode spectrum of a H1 and a L3 cavity are shown in Figure 6-8 and Figure 6-9. As Akahane et al. [90] have published, it is important for an increase of the Q factor that the envelope function of the mode profile is confined in-plane. For a point defect in a 2D PC membrane, the PBG effect is used to limit the light in the plane. In addition, total internal reflection at the interface between air and active layer results in a vertical confinement.

When light is confined in a very small cavity, different components of the plane wave with different wave vector magnitudes and directions are created. The tangential component of the wave vector in the layer plays an important role. If this is between 0 and $\frac{2\pi}{\lambda}$, the wave can escape to the air, because the conservation law is fulfilled. If, however, the wave vector is larger than $\frac{2\pi}{\lambda}$, the light is strongly limited in-plane because the conservation law is not fulfilled, i.e. total reflection prevails.

(a)

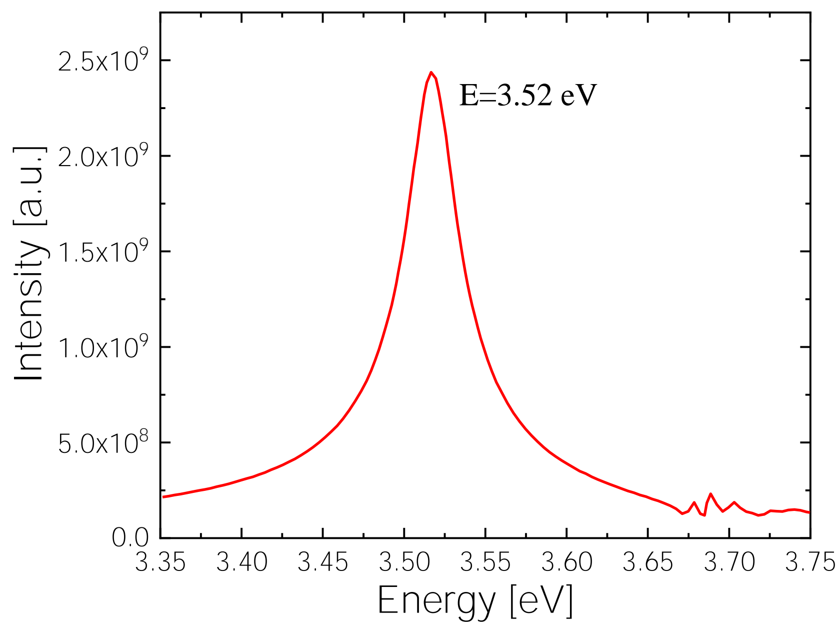

(b)

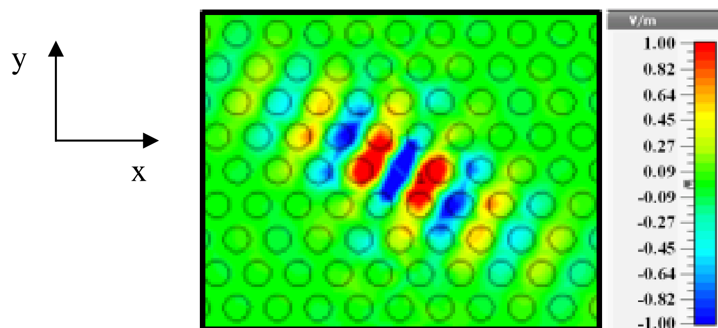

Figure 6-8: Spectrum of an H1 cavity with a r/a-ratio of 0.32 (a) and the electric field in y-direction (b).

The simulations, shown here, are done using the parameters for PC1. In Figure 6-8 (a) the spectrum for the H1 cavity is shown. One clear mode is visible with an energy of E = 3.52 eV. The electric field distribution for the fundamental mode is shown. The air holes are indicated by grey circles, a hole being omitted in the center of the figure to generate the H1 cavity. A diagonal dipole field for the electric field in y-direction is visible (see Figure 6-8 (b)). Red parts represent areas with an electric field higher than zero and blue parts signify areas with an electric field lower than zero. Only in the area of the defect an electric field is visible, whereas the surrounding approaches zero. If a

maxima of the field is directly located in an air hole, it is influenced from the medium. If the maxima are mainly located outside the air holes, the influence of another refractive index on the modes is relatively low.

In addition, the simulations are done for the L3 cavity (see Figure 6-9). This cavity shows modes at E = 3.46 eV and E = 3.68 eV (see Figure 6-9 (a)). The electric field distribution in y-direction is attached, too. Here, a quadrupole mode is visible for the electric field in y-direction (see Figure 6-9 (b)).

(a)

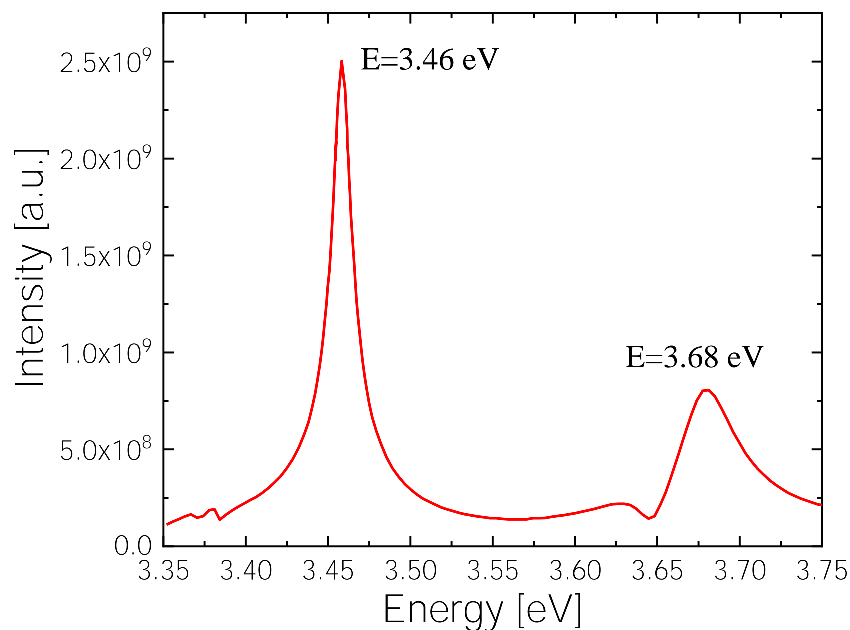

(b)

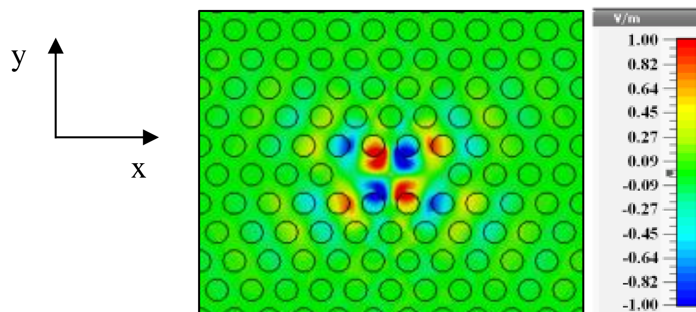

Figure 6-9: Spectrum of an L3 cavity with an r/a-ratio of 0.32 (a) and the electric field distribution in y-direction of the mode at 3.68 eV.

6.3 µ-PL Measurements of PC Membranes

Micro-PL (µ-PL) measurements at room temperature are performed on two different PC membranes to study the optical properties and compare it to the simulations done in chapter 6.2. The detailed information of the setup is described in chapter 3.2.3. Several H1 and L3 cavities were measured. One exemplary spectrum of the H1 cavity is shown in Figure 6-10.

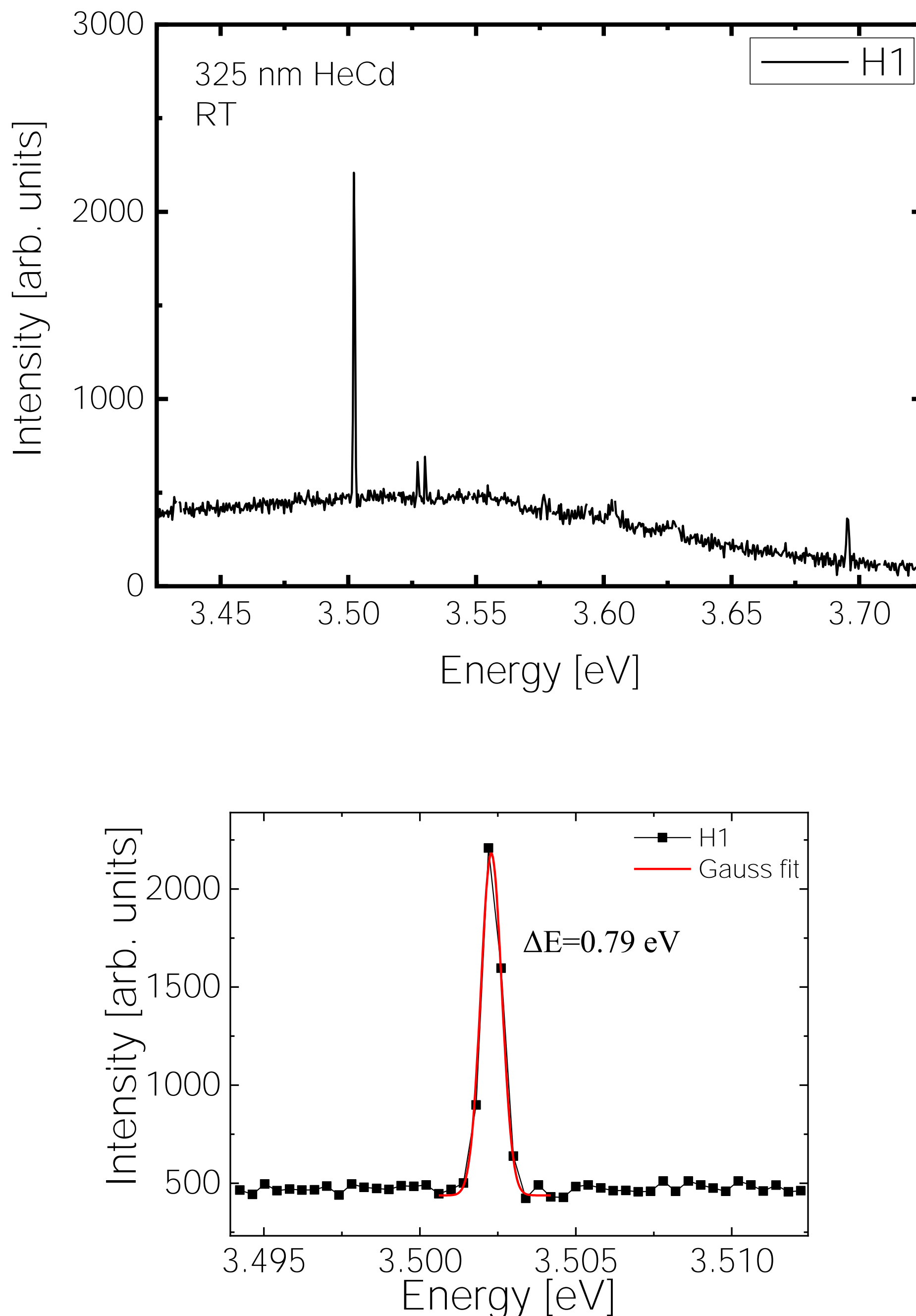

Figure 6-10: Room temperature PL measurements of a H1 cavity and close-up of the mode.

Distinct modes are observable in this spectrum. The dominating peak is at an energy of E = 3.51 eV. To better determine this peak, a close-up of this peak is shown as well, where it becomes visible that the FWHM is ΔE = 0.79 meV. This corresponds to a Q factor of about 4400. The residual peaks appearing at around 3.525 eV can be assigned to plasma lines of the HeCd-laser.

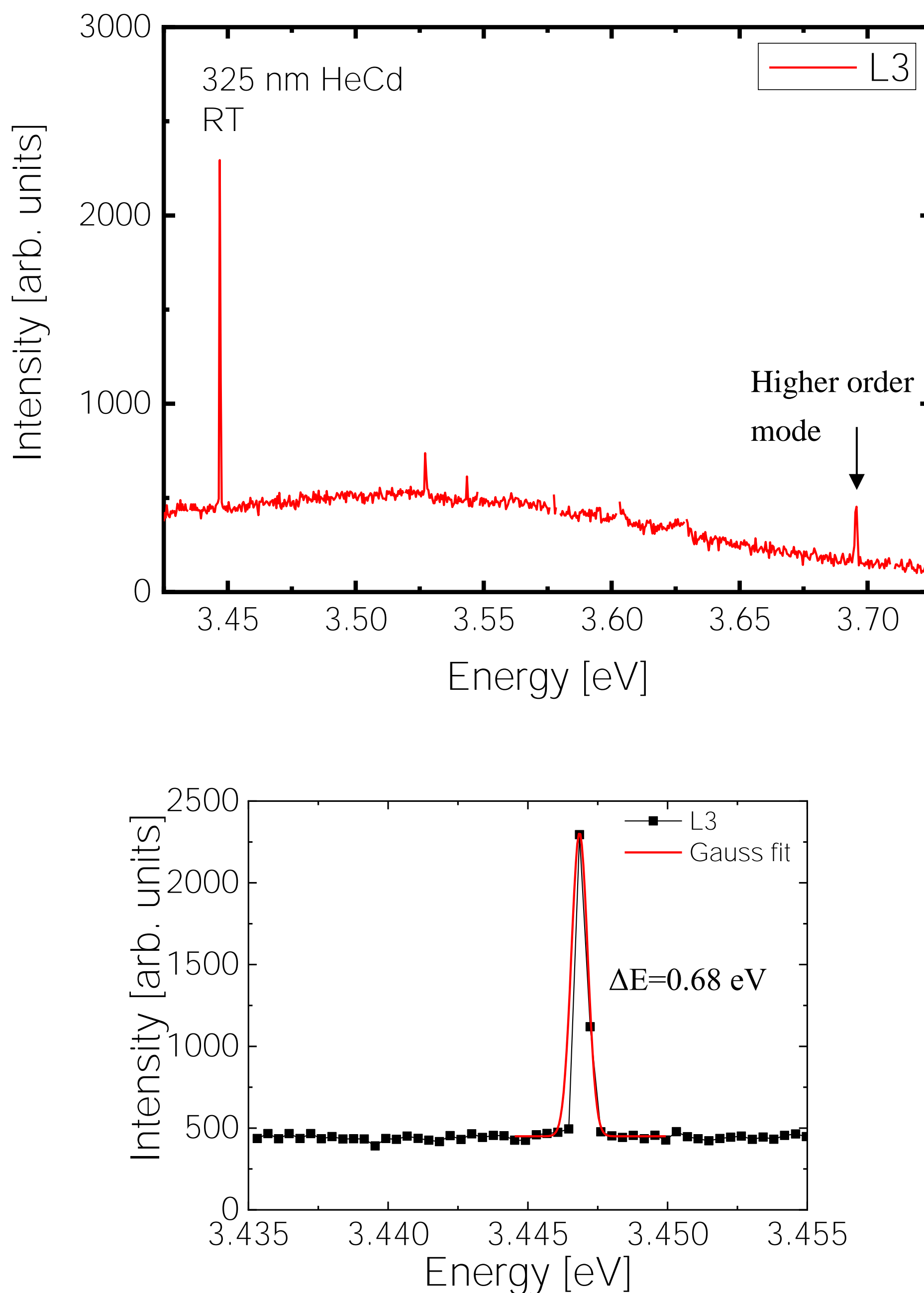

Figure 6-11: Room-temperature μ-PL measurements of a L3 cavity and close-up of the fundamental mode.

Figure 6-11 shows the spectrum of the L3 cavity. Here, two narrow peaks are visible. Whereby the mode with an emission energy of E = 3.45 eV is dominant. The FWHM of this fundamental mode is ΔE = 0.68 meV. As can be observed in the close-up of the peak, it consists of only four measuring points. This is related to the resolution of the measurement setup. The quality factor is estimated to a value of about $Q \cong \frac{E}{\Delta E} \cong 5000$. This value is comparable to the maximal Q factor reachable for this material system. The higher order mode has also been analyzed (not shown here). The energetic peak position is E = 3.69 eV and the FWHM is ΔE = 1.2 meV, resulting in a Q factor of Q = 3000. The order of magnitude of the Q factors reached in this work corresponds to the values known from literature. For example, Néel et al. [91] have achieved Q factors of 1800 for L3 cavities of h-AlN with embedded h-GaN QDs.

Table 8: Energetic mode positions for the experimental and simulated results of chapter 6.2.

Cavity	Mode energy (experimental) [eV]	Mode energy (simulated) [eV]
H1	3.51	3.52
L3	3.45	3.46
	3.7	3.68

Table 8 compares the results of the experiment with the calculations made in chapter 6.2. The experimental and calculated mode energies for the H1 and L3 cavities are shown. The simulated mode energies have been determined by the simulation program of CST Microwave Studio. The mode energies show an excellent agreement. Only a small difference of $\Delta E_{H1} = 0.01$ eV for the H1 cavity and a difference of $\Delta E_{L3,1} = 0.01$ eV for the fundamental mode and $\Delta E_{L3,2} = 0.02$ eV is observable. This small deviation originates from imperfections of the PC. As already described in chapter 6.1, the diameter of the air holes decreases from the center to the border of the PC due to the proximity effect during EBL. Additionally, the air holes are not perfectly circular. The hole radius and the lattice constant are very sensitive parameters. Only a small change leads to a direct change in the energetic position and therefore to a change of the Q factor. The other small peaks visible in this spectrum are again due to the HeCd plasma lines, which could not be suppressed completely.

6.4 Summary of PC Membranes

PC membranes have been successfully manufactured. In this chapter it is shown that processes in dry and wet chemical etching and electron-beam lithography were successfully created. In order to obtain the correct hole diameter and lattice constant, the parameters of the individual process steps were adapted exactly. This was realized for different cavities like L3, L5, L9 and H1, H7 and H15. In determining the largest possible PBG, simulations were performed with the commercially available time domain solver CST Microwave Studio. It was shown that the PBG is strongly dependent on the slab thickness, the lattice constant and the hole diameter. Therefore, all parameters were varied one after the other to achieve the largest possible PBG.

For the optical characterization of the fabricated PC membranes, room temperature PL measurements were performed on H1 and L3 cavities. Individual modes are visible. These have high Q factors. For the H1 cavity this is 4400 and for the main mode of the L3 cavity this is 5000. The position of the modes fits perfectly to the simulated mode energies.

7 Summary

In this work PC membranes with c-GaN QDs incorporated are realized. The results can be divided into two main sections: Firstly, self-assembled QDs embedded in a c-AlN matrix are investigated theoretically, optically and structurally. The QDs are grown in the SK growth mode by plasma-enhanced MBE on a 3C-SiC /Si (001) substrate. Both, one QD layer as well as several QD layers on top of each other separated by a spacer layer with varying thickness are content of these chapters. Secondly, PC membranes with one layer of QDs are fabricated. Theoretical calculations as well as optical and structural analyses were performed here.

In the first part, samples with one layer of QDs show a redshift of emission energy with increasing QD deposition amount in PL measurements. The shape of each spectrum is a superposition of Gaussian shaped emission bands of many individual QDs. The decrease of emission energy can be explained by an increase of the QD height with increasing deposited amount of c-GaN. In our QDs the main confining parameter is the QD height. Theoretical calculations with nextnano++ could successfully verify the emission energy of single QD layers.

To investigate the coupling of stacked QDs, two QD layers with one layer of smaller QDs (LQDs) and one layer of bigger QDs (UQDs) on top are stacked on each other. The spacer layer thickness is 2 and 20 nm, respectively. PL measurements give a first hint of an increased carrier transfer probability for the sample with the thin spacer layer. For the sample with the thick spacer layer, two clear emission peaks are visible corresponding to the two QD sizes. Decreasing the spacer layer thickness leads to a single emission peak corresponding to the UQDs, which suggests a carrier transfer and an electrical coupling between the two layers. Additionally, the structural coupling is investigated by strain calculations with nextnano++. The QDs are compressively strained in growth direction, which influences the surrounding of the QDs and lead to a tensile strained c-AlN. By reducing the spacer layer thickness, the tensile strained area of the LQD influences the position of the UQD resulting in a vertical alignment of the QDs.

This vertical alignment is also examined with the help of a sample series with stacked QDs up to 13 layers. Cross-sectional TEM measurements show a vertical alignment of the QDs as long as no stacking faults are present. Stacking faults exist in the [111] plane in the cubic phase and lead to an accumulation of QDs at these line defects, because they act like elastic potential minima on the surface. Additionally, PL measurements are performed showing an increase of emission intensity with increasing number of stacked layers. The FWHM of all samples is almost regardless of the number of stacked layers leading to the assumption that no homogenization of the QD size and shape takes place. This is in contrast to the hexagonal phase and InAs QDs for example. Looking at the emission energy, a blueshift is observed with increasing number of stacked layers. This

shift is due to a decrease of the QD height. The samples with a large number of QDs are promising candidates for application in highly efficient UV light emitters.

The second part of this work contains the successful realization of PC membranes with one layer of QDs incorporated. The fabrication process contains a structuring step using electron-beam lithography and several wet- and dry-etching steps to realize a hexagonal lattice of air holes in the free-standing active layer. SEM measurements demonstrate the different fabrication steps and the successful undercut of the active layer. μ-PL measurements are performed on two different PC structures, including H1 and L3 cavities, showing fundamental modes with high quality factors. The H1 cavity has a quality factor of 4400. The fundamental mode of the L3 cavity is estimated to a quality factor 5000. Both values are comparable to literature.

The mode energies are simulated using the time domain solver of CST Microwave Studio to validate the experimental results. Mode energies of 3.51 eV for the H1 cavity and 3.45 eV and 3.7 eV for the L3 cavity are measured by μ-PL measurements. The simulated mode energies exhibit small differences of 10 meV for the fundamental modes, resulting in an excellent agreement between simulation and experiment. The small difference can be explained by imperfections of the PC. The air hole radius as well as the lattice constant are very sensitive parameters for the quality factor.

The results presented in this work show significant properties of c-GaN QDs and the successful integration of QDs in PC. The knowledge gained can be used for further studies to achieve applications in quantum information technology.

8 Outlook

In view of the subsequent fields of research based on these findings, a variety of possibilities remains. The high quality factor of the PCs presented in this work can be increased further by varying the design of the PC. By changing size and position of, for example, three air holes next to the cavity, the quality factor can be increased rapidly. First attempts have already been made in this work and can be seen in chapter 9.6. However, the quality of the sample is not as before and the optimized holes are not yet perfectly circular. Therefore, an optical characterization was refrained from so far. However, an adjustment of the parameters during EBL can lead to an optimal result.

Additionally, the samples with stacked QDs show an increased PL intensity. In consequence of the higher gain, an increased mode intensity is expected. This, in turn, leads to the possibility to obtain laser oscillations and to use it as a nanocavity laser.

To reach the long-wave range, which is interesting for telecommunication applications, the addition of indium is possible. First attempts to grow InN have already been made [92]. A band gap of 0.56 eV at room temperature was shown. A next step would be to realize the ternary semiconductor InAlN and to be able to control the band gap by the In percentage.

9 Appendix

9.1 List of Figures

Figure 2-1: Crystal structure of (a) h-GaN and (b) c-GaN. Green spheres indicate Ga atoms and blue spheres N atoms. 3

Figure 2-2: Schematic illustration of the band diagram for the cubic phase without internal electric field and for the hexagonal phase, which has an internal polarization field. The probability density for electrons (red) and holes (green) is sketched.. 4

Figure 2-3: Density of states for (a) bulk, (b) quantum well (one-dimensional confinement), (c) quantum wire (two-dimensional confinement) and (d) quantum dot (three-dimensional confinement) [23]. 5

Figure 2-4: µ-PL spectra of single c-GaN QDs at a temperature of 4 K. The grey area shows the emission of the QD ensemble [24]. 6

Figure 2-5: Shape (left), isosurfaces of the probability density $\psi e2 = \rho$ for the lowest electron and hole state (middle) and the piezoelectric potential of a QD with 3 nm height (right) for (a) h-GaN/AlN and (b) c-GaN/AlN [20]. 7

Figure 2-6: (a) Schematic illustration of the 2D air hole lattice of a square and a hexagonal lattice with lattice vectors a_1 and a_2, (b) reciprocal lattice with reciprocal lattice vectors G_1 and G_2 and the first Brillouin Zone (yellow), (c) first Brillouin Zone with irreducible BZ and high symmetry points Γ, M and K [28]. 11

Figure 2-7: Schematic illustration of the field distribution in a photonic crystal from [28]. (a) and (b) show the E-fields and (c) and (d) the intensities of the highest frequency of the first band or the lowest frequency of the second band. Blue indicates the region with higher dielectric constant.. 12

Figure 2-8: Schematic representation of typical cavity sizes. The L-cavities consist of missing holes in a row and the H-cavities of missing holes radially around the center. 13

Figure 2-9: Band diagram for photonic crystal slab. The blue part (light cone) shows the extended modes propagating in air, below the cone the guided modes are located. The blue bands show the TM-like and the red bands, the TE-like bands. The first BZ is shown in the inset with the irreducible BZ, marked blue [28]. . 15

Figure 2-10: Schematic illustration of a cavity design by Triviño et al. [38]. It shows the h-GaN layer on top of an h-AlN buffer layer with a hexagonal array of holes and three holes missing in a row in the center. The holes which were modified for the optimized Q are marked in red. 17

Figure 3-1: Growth on a lattice mismatched substrate (a) pseudomorphically strained growth, (b) partially relaxed layer and (c) island growth. The lattice constant of the substrate is smaller than that of the epilayer. 21

Figure 3-2 Schematic representation of the three different growth techniques: Frank-van der Merwe, Volmer-Weber and Stranski-Krastanov (after [43])....................... 23

Figure 3-3: Schematic drawing of the MBE Riber 32 system [58]..................................... 24

Figure 3-4: RHEED diffraction by means of the Ewald-sphere construction [60]. 25

Figure 3-5: (a) Basic principle of an AFM setup. (b) Lennard-Jones potential showing the inter-atomic force over the distance between two atoms. Additionally it is shown in which force regimes the three different AFM measurement techniques are operating [61]... 27

Figure 3-6: Illustration of the HRXRD setup [64]. From right to left: x-ray tube, mirror, monochromator, sample, analyzer and detector. The sample is mounted on an Euler cradle. The angles of the incoming (ω) and diffracted beam (2Θ) are shown, too.. 28

Figure 3-7: Schematic diagram of the several radiative transitions in a semiconductor: band to band transitions (e, h), free exciton transitions (FX), bound exciton transition (D^0, X/A^0, X) and donor acceptor transitions (D^0, A^0) (after [60]). 30

Figure 3-8: Schematic illustration of the μ-PL setup in the group of Prof. Dr. C. Meier. ...31

Figure 3-9: Basic setup of a TEM system (after [66])...33

Figure 3-10: Main imaging modi in a TEM. The general electron beam alignment (a), bright-field imaging (b) and dark-field imaging (c) (after [66]). 34

Figure 4-1: RHEED pattern of 3C-SiC measured at the [110] azimuth before Al flashes (a) and after 10 cycles of Al flashes (b). The Al flashes lead to a brighter and nicely streaky pattern with reconstruction reflexes in between the main reflexes. 37

Figure 4-2: RHEED intensity of the 3D part of the (-1,0) reflex during c-AlN growth. The growth is determined by 20 s of depositing Al and N on the surface and 30 s break afterwards with both shutters closed. The inset shows the RHEED intensity pattern during the growth. 38

Figure 4-3: AFM measurements on c-AlN layers. The sample with 60 nm (a) has a rms of 0.91 nm. After a thickness of 230 nm the rms increased by a factor of two and results in a rsm of 2.4 nm. 39

Figure 4-4: RHEED pattern measured at the [110] azimuth of AlN growth after 9 min (30 nm) (a), 33 min (117 nm) (b) and after 65 min (230 nm) (c). 40

Figure 4-5: Reciprocal space map around the (002) reflex of 3C-SiC and a thick layer of epitaxial grown c-AlN on 3C-SiC...41

Figure 4-6: Sample structure of sample series A with one layer of QDs embedded in a c-AlN matrix of 30 nm layer thickness each on top of a 10 μm thick 3C-SiC substrate grown on a 500 μm Si (001). By changing the growth time, the amount of deposited c-GaN is varied between 13 and 30 s, which corresponds to a c-GaN coverage of 3 to 5 ML. 42

Figure 4-7: RHEED intensity of the 3D part of the (-1,0) reflex during termination and QD growth. The inset shows the RHEED diffraction pattern containing a mark for the measured point. 44

Figure 4-8: RHEED pattern measured at the [110] azimuth after growth of the c-AlN buffer layer after 13 min (30 nm) (a), the QD growth (b) and the c-AlN top layer growth after 13 min (30 nm) (c). 45

Figure 4-9: AFM images of uncapped (a) and capped (b) QDs. The thickness of the c-AlN buffer layer and in (b) the top layer, respectively, is 30 nm. The QD density of the uncapped QDs is about 1.2·1011QDscm2 and the surface roughness of the c-AlN with the capped c-GaN QDs is 1.4 nm..46

Figure 4-10: Normalized room temperature PL spectra of one layer of c-GaN QDs with deposition times from 13 to 30 s. The peak energy is shifted from 3.73 eV to 3.59 eV...47

Figure 4-11: Sample structure of sample series B. The upper QD (UQD) layer is composed of bigger QDs and the lower QD (UQD) layer of smaller QDs. The c-AlN buffer and top layer have a thickness of 30 nm each, the spacer layer thickness is varied (2 and 20 nm thickness). 48

Figure 4-12: Room temperature PL measurements and corresponding fitting curve of asymmetric QD pairs with a spacer layer thickness of 20 nm (sample B1). The green line corresponds to the LQDs, the blue line to the UQDs. 49

Figure 4-13: Room temperature PL measurement and corresponding fitting curve of an asymmetric QD pair with a spacer layer thickness of 2 nm (sample B2). 50

Figure 4-14: Sample structure of the sample with five stacked layers of QDs and an additional uncapped c-GaN QD layer on top. The c-AlN buffer layer and the c-AlN spacer layers have a thickness of 10 nm each. 51

Figure 4-15: RHEED pattern measured at the [110] azimuth after the seventh c-AlN spacer layer. The pattern is still streaky and 2D. 52

Figure 4-16: Line scans of RHEED patterns after growth of the third, fifth and seventh spacer layer. The selected position is shown in Figure 4-15. The line scans are plotted with an offset in y-direction...53

Figure 4-17: A 10 x 10 µm² AFM measurement of the c-AlN layer after 10 stacked QD layers of QDs without a top QD layer. The rms is 2.7 nm. 54

Figure 4-18: 1x1 µm² AFM scans of the uncapped top layer of QDs of (a) a sample with five stacks of QDs and (b) a sample with 13 layers of QDs.............................55

Figure 4-19: HAADF image of the sample with eight layers of QDs and an additional top layer of QDs. The red dashed line indicates the interface between 3C-SiC and c-AlN. 56

Figure 4-20: EDX mapping of the sample with eight layers of QDs and an additional top layer of QDs of the red marked in Figure 4-19. (a) Al content is marked purple (a), the red marked area shows the existence of Ga (b), the light grey part represents the Si (c) and the grey part represents the C incorporation (d).........57

Figure 4-21: Contrast analysis of the TEM image to determine the c-AlN thickness. The upper region has been neglected, because of the low contrast ratio due to the smearing of the planes. 58

Figure 4-22: Cross-sectional TEM picture with atomic resolution in (110) direction. The GaN QD and the wetting layer appear dark, the c-AlN spacer layer brighter. No stacking fault is visible in this area. The yellow line indicates the truncated pyramidal shape...59

Figure 4-23: TEM picture of a sample region with stacking faults. The area framed by dashed red lines shows that the vertical alignment is tilted in (111) direction along the stacking fault...60

Figure 4-24: PL intensity (in logarithmic scale) versus the emission energy of the stacked QDs with 1, 5, 8, 10 and 13 layers of QDs. The measurements are done at room temperature. The emission energy and the intensity increase with increasing number of stacks...61

Figure 4-25: Emission energy and integrated intensity (semilogarithmic scale) as a function of the number of stacks. In both cases, an increase with increasing number of stacks is observable. 62

Figure 5-1: Shape of the QDs used for the simulations with nextnano++. The cross section of the bottom of the pyramid is a 10 x 10 nm² square in the x-y-coordinate system (a). In the y-z-direction the QD has a truncated pyramidal shape (b). The height of the QD is 2 nm. The wetting layer is also visible and the thickness amounts to 0.7 nm. 65

Figure 5-2: Results of the eight-band k·p model of the conduction band minimum and valence band maximum as a function of the QD height. The diameter of the QD is varied between 5 and 20 nm, because of the broadening of the size. 67

Figure 5-3: Results of the eight band k·p model of the transition energy as a function of the QD height. The diameter of the QD is varied between 5 and 20 nm, because of the broadening of the size...68

Figure 5-4: Emission energy as a function of the GaN coverage for the experimental results and the QD height for the simulations for a QD width of 10 and 20 nm...........69

Figure 5-5: Strain simulations in growth direction for QD pairs similar to chapter 5 with (a) a spacer layer thickness of 20 nm and (b) a spacer layer thickness of 4 nm. 70

Figure 6-1: First four steps of the fabrication process of the PC membrane. Each fabrication step is shown including the deposition of SiO_2 as hard mask with PECVD (a), spin coating of positive photoresist (b), patterning with electron-beam

lithography (c) and RIE etching of SiO_2 (d). ashing of the photoresist (e) and realization of the undercut by RIE (f). 73

Figure 6-2: Second four steps of the fabrication process of the PC membrane. Each fabrication step is shown including ashing of the photoresist (e), etching of the active layer (f), removing the hard mask (g) and realization of the undercut by RIE (h). 74

Figure 6-3: Mask for EBL of one element and a close-up of one PC out of this element. Nine PCs are arranged in one pattern. In this case L3 cavities with a radius of r = 59 nm, lattice constant of a = 169 nm and a dose factor of 1.26 are shown.75

Figure 6-4: SEM images of the last three steps of the fabrication process of the PC membranes, which correspond to images (f), (g) and (h) in Figure 6-1 and Figure 6-2. A top view of a L3-cavity is shown as well as a close-up of the defect of the PC in (a) and (b) and a cross-section of the free-standing membrane in (c). 79

Figure 6-5: Photonic band structure of TE-like modes with slab thicknesses h = 62 nm, lattice constant a = 170 nm and air hole radius r = 108.8 nm. The black line indicates the light cone. The resulting PBG is shaded in grey color. The emission of the QDs is assumed to lie in the middle of the PBG. 80

Figure 6-6: Photonic band structure of TM-like modes with slab thicknesses h = 62 nm, lattice constant a = 170 nm and air hole diameter d = 108.8 nm. The black line indicates the light cone. No PBG is observable. 81

Figure 6-7: Photonic band structure of TE-like modes with the following features of PC5 (a) with slab thickness h = 46.5 nm, lattice constant a = 186 nm, air hole diameter d = 149 nm and a PC with the active layer directly on top of the substrate (b) with lattice constant a = 344 nm, air hole diameter d = 276 nm and slab thickness h = 172 nm. 83

Figure 6-8: Spectrum of an H1 cavity with a r/a-ratio of 0.32 (a) and the electric field in y-direction (b). 84

Figure 6-9: Spectrum of an L3 cavity with an r/a-ratio of 0.32 (a) and the electric field distribution in y-direction of the mode at 3.68 eV. 85

Figure 6-10: Room temperature PL measurements of a H1 cavity and close-up of the mode. 86

Figure 6-11: Room-temperature µ-PL measurements of a L3 cavity and close-up of the fundamental mode. 87

Figure 9-1: Comparison of the displayed temperature on the Eurotherm controller with the actual temperature determined from the evaporation behavior of Al, In and Ga. XIX

Figure 9-2: SEM picture of an optimized L3 cavity. The adjacent three holes next to the cavity have been optimized in diameter and position. XX

9.2 List of Tables

Table 1: Parameters for 3C-SiC. 20
Table 2: Parameters for c-AlN and c-GaN used in this work. 20
Table 3: List of sample series A with one layer of QDs. The c-GaN deposition time is varied from 13 to 30 s. The GaN coverage is calculated for a layer-by-layer growth and increases from 3 to 5 ML. 43
Table 4: List of sample series B with two layers of QDs. The deposition time of the LQD and the UQD is specified. The thickness of the spacer layer varies between 2 and 20 nm. 48
Table 5: QD densities for a different number of stacked QD layers. The density slightly decreases with increasing number of QD layers. 55
Table 6: Optimized parameters for different PC cavities. The values are determined using SEM images. The criteria are as round holes as possible, no undesirable defects and a constant air hole radius. 76
Table 7: Results of the simulations for different PCs. The lattice constant a, hole diameter d and slab thickness t are varied. The minimum and maximum of the bandgap are calculated with the help of CST Microwave Studio to determine the resulting photonic band gap thickness. 82
Table 8: Energetic mode positions for the experimental and simulated results of chapter 6.2. 88

9.3 Bibliography

1.1 Motivation

[1] H. Saito, K. Nishi, I. Ogura, S. Sugou, and Y. Sugimoto, Appl. Phys. Lett. **69**, 3140 (1996).

[2] G. S. Solomon, J. A. Trezza, A. F. Marshall, and J. S. Harris, Phys. Rev. Lett. **76**, 952 (1996).

[3] N. N. Ledentsov, V. A. Shchukin, M. Grundmann, N. Kirstaedter, J. Böhrer, O. Schmidt, D. Bimberg, V. M. Ustinov, A. Y. Egorov, A. E. Zhukov, P. S. Kop'ev, S. V Zaitsev, N. Y. Gordeev, Z. I. Alferov, A. I. Borovkov, A. O. Kosogov, S. S. Ruvimov, P. Werner, U. Gösele, and J. Heydenreich, Phys. Rev. B **54**, 8743 (1996).

[4] H. Heidemeyer, S. Kiravittaya, C. Muller, N. Y. Jin Phillipp, and O. G. Schmidt, Appl. Phys. Lett. **80**, 1544 (2002).

[5] M. O. Lipinski, H. Schuler, O. G. Schmidt, K. Eberl, and N. Y. Jin-Phillipp, Appl. Phys. Lett. **77**, 1789 (2000).

[6] H. Shoji, Y. Nakata, K. Mukai, Y. Sugiyama, M. Sugawara, N. Yokoyama, and H. Ishikawa, Japan. Jour. of Appl. Phys. **35**, L903 (1996).

[7] K. Hoshino, S. Kako, and Y. Arakawa, Phys. Stat. Sol. **240**, 322 (2003).

[8] C. Santori, S. Götzinger, Y. Yamamoto, S. Kako, K. Hoshino, and Y. Arakawa, Appl. Phys. Lett. **87**, 8 (2005).

[9] T. Schupp, T. Meisch, B. Neuschl, M. Feneberg, K. Thonke, K. Lischka, and D. J. As, Phys. Status Solidi Curr. Top. Solid State Phys. **8**, 1495 (2011).

[10] T. Schupp, T. Meisch, B. Neuschl, M. Feneberg, K. Thonke, K. Lischka, and D. J. As, J. Cryst. Growth **312**, 3235 (2010).

[11] M. Bürger, J. K. N. Lindner, D. Reuter, and D. J. As, Phys. Status Solidi **12**, 452 (2015).

[12] S. Kako, M. Holmes, S. Sergent, M. Bürger, D. J. As, and Y. Arakawa, Appl. Phys. Lett. **104**, 011101 (2014).

[13] S. Kako, M. Miyamura, K. Tachibana, K. Hoshino, and Y. Arakawa, Appl. Phys. Lett. **83**, 984 (2003).

[14] N. Li, M. Arita, S. Kako, M. Kitamura, S. Iwamoto, and Y. Arakawa, Phys. Status Solidi **4**, 90 (2007).

[15] T. Yoshie, O. B. Shchekin, H. Chen, D. G. Deppe, and A. Scherer, Electron. Lett. **38**, 967 (2002).

[16] E. Yablonovitch, Phys. Rev. Lett. **58**, 2059 (1986).

[17] M. Bürger, M. Ruth, S. Declair, J. Förstner, C. Meier, and D. J. As, Appl. Phys. Lett. **102**, 100 (2013).

[18] S. Sergent, S. Kako, M. Bürger, S. Blumenthal, S. Iwamoto, D. J. As, and Y. Arakawa, Appl. Phys. Express **9**, 9 (2016).

2.1 Physical Properties of Cubic Group III-Nitrides

[19] C. Kittel, *Einführung in Die Festkörperphysik* (Oldenbourg Wissenschaftsverlag, 2013).

[20] V. A. Fonoberov and A. A. Balandin, J. Appl. Phys. **94**, 7178 (2003).

[21] K. Kim, W. Lambrecht, and B. Segall, Phys. Rev. B **56**, 7018 (1997).

2.2 Quantum Dots

[22] Y. Arakawa and H. Sakaki, Appl. Phys. Lett. **40**, 939 (1982).

[23] R. A. Hogg and Z. Zhang, Phys. Eng. Compact Quantum Dot-Based Lasers Biophotonics 7 (2014).

[24] M. Bürger, Diss. Univ. Paderborn (2014).

[25] D. Bimberg, *Semiconductor Nanostructures* (Springer, 2008).

[26] J. Ramsden, *Nanotechnology: An Introduction* (Elsevier, 2011).

2.3 Photonic Crystals

[27] D. Bouwmeester, A. K. Ekert, and A. Zeilinger, *The Physics of Quantum Information* (Springer Science & Business Media, 2013).

[28] J. J. D. Joannopoulos, S. Johnson, J. N. J. Winn, and R. R. D. Meade, *Photonic Crystals: Molding the Flow of Light* (Princeton University Press, 2008).

[29] B. E. A. Saleh and M. C. Teich, *Grundlagen Der Photonik*, 2., vollst (Wiley-VCH, 2003).

[30] O. Painter, J. Vučkovič, and A. Scherer, J. Opt. Soc. Am. B **16**, 275 (1999).

[31] Y. Akahane, T. Asano, B. S. Song, and S. Noda, Appl. Phys. Lett. **83**, 1512 (2003).

[32] Y. S. Choi, M. T. Rakher, K. Hennessy, S. Strauf, A. Badolato, P. M. Petroff, D. Bouwmeester, and E. L. Hu, Appl. Phys. Lett. **91**, 2005 (2007).

[33] K. J. Vahala, Nature **424**, 839 (2004).

[34] T. F. Krauss, R. M. De La Rue, and S. Brand, Nature **383**, 699 (1996).

[35] E. M. Purcell, Phys. Rev. **69**, 681 (1946).

[36] Y. S. Choi, K. Hennessy, R. Sharma, E. Haberer, Y. Gao, S. P. Denbaars, S. Nakamura, E. L. Hu, and C. Meier, Appl. Phys. Lett. **87**, 1 (2005).

[37] N. Vico Triviño, G. Rossbach, U. Dharanipathy, J. Levrat, A. Castiglia, J. F. Carlin, K. A. Atlasov, R. Butté, R. Houdré, and N. Grandjean, Appl. Phys. Lett. **100**, 071103 (2012).

[38] N. V. Triviño, M. Minkov, G. Urbinati, M. Galli, J. F. Carlin, R. Butt??, V. Savona, and N. Grandjean, Appl. Phys. Lett. **105**, 231119 (2014).

[39] H. Ryu, J. Hwang, and Y. Lee, Phys. Rev. B **59**, 5463 (1999).

[40] A. Fiore, J. X. Chen, and M. Ilegems, Appl. Phys. Lett. **81**, 1756 (2002).

[41] D. J. P. Ellis, A. J. Bennett, A. J. Shields, P. Atkinson, and D. A. Ritchie, Appl. Phys. Lett. **90**, 233514 (2007).

[42] P. Michler, A. Kiraz, L. Zhang, C. Becher, E. Hu, A. Imamoglu, P. Michler, A. Kiraz, L. Zhang, C. Becher, E. Hu, and A. Imamoglu, Appl. Phys. Lett. **77**, 184

(2000).

3.1 Growth

[43] H. Herman, Marian A., Sitter, *Molcular Beam Epitaxy: Fundamentals and Current Status*, Band 7 (Springer, Berlin, 1989).

[44] A. Taylor and R. M. Jones, *Silicon Carbide - A High Temperature Semiconductor* (Pergamon Press, Oxford, London, New York, Paris, 1960).

[45] M. E. Levinshtein, S. L. Rumyantsev, and M. S. Shur, *Properties of Advanced Semiconductor Materials GaN, AlN, InN, BN, SiC, SiGe* (John Wiley and Sons, 2001).

[46] T. Schupp, K. Lischka, and D. J. As, J. Cryst. Growth **312**, 1500 (2010).

[47] M. Röppischer, R. Goldhahn, G. Rossbach, P. Schley, C. Cobet, N. Esser, T. Schupp, K. Lischka, and D. J. As, J. Appl. Phys. **106**, 7 (2009).

[48] M. Feneberg, M. Röppischer, C. Cobet, N. Esser, J. Schörmann, T. Schupp, D. J. As, F. Hörich, J. Bläsing, A. Krost, and R. Goldhahn, Phys. Rev. B **85**, 155207 (2012).

[49] L. C. de Carvalho, A. Schleife, and F. Bechstedt, Phys. Rev. B **84**, 195105 (2011).

[50] C. G. Van De Walle, Mater. Res. **70**, 2577 (1997).

[51] S.-H. Park and S.-L. Chuang, J. Appl. Phys. **87**, 353 (2000).

[52] J. E. Ayers, *Heteroepitaxy of Semiconductors: Theory, Growth and Characterization* (Taylor&Francis Group, 2007).

[53] L. Dong, J. Schnitker, R. W. Smith, and D. J. Srolovitz, J. Appl. Phys. **83**, 217 (1998).

[54] E. Pehlke, N. Moll, A. Kley, and M. Scheffler, Appl. Phys. A Mater. Sci. Process. **65**, 525 (1997).

[55] J. W. Matthews and A. E. Blakeslee, J. Cryst. Growth **27**, 118 (1974).

[56] D. J. Hull, D., Bacon, *Introduction to Dislocations*, 5th ed. (Elsevier Ltd., 2011).

[57] T. J. Sherwin, M.E., Drummond, **69**, 8423 (1991).

[58] *Riber Instruction Manual (608 26G 52 DOCTEPAO OCT/92)* (1992).

[59] W. Braun, *Applied RHEED* (Springer, 1999).

[60] R. M. Kemper, Diss. Univ. Paderborn (2014).

3.2 Characterization

[61] D. Johnson, N. Hilal, and W. R. Bowen, *Atomic Force Microscopy in Process Engineering* (Elsevier Ltd., Oxford, 2009).

[62] W. L. Bragg, Proc. Cambridge Phil. Soc. **17**, (1913).

[63] M. Birkholz, *Thin Film Analysis by X-Ray Scattering* (Wiley-VCH Verlag GmbH & Co. KG, Weinheim, 2006).

[64] P. Kidd, *XRD of Gallium Nitride and Related Compounds: Strain, Composition and Layer Thickness* (The Analytical X-ray Company, 2009).

[65] S. Perkowitz, *Optical Characterization of Semiconductors: Infrared, Raman, and Photoluminescence Spectroscopy* (Academic Press, 1993).

[66] B. Fultz and J. M. Howe, *Transmission Electron Microscopy and Diffractometry of Materials* (Springer, Berlin, 2008).

4.2 Thick c-AlN Layers

[67] J. Schörmann, S. Potthast, D. J. As, and K. Lischka, Appl. Phys. Lett. **90**, 041918 (2007).

[68] D. J. As, Microelectronics J. **40**, 204 (2009).

[69] T. Schupp, G. Rossbach, P. Schley, R. Goldhahn, M. Röppischer, N. Esser, C. Cobet, K. Lischka, and D. J. As, Phys. Status Solidi Appl. Mater. Sci. **207**, 1365 (2010).

4.3 Single QD Layers

[70] D. J. As, S. Potthast, U. Köhler, A. Khartchenko, and K. Lischka, MRS Symp. Proc. **743**, (2003).

[71] S. Kako, M. Holmes, S. Sergent, M. Bürger, D. J. As, and Y. Arakawa, Appl. Phys. Lett. **104**, 011101 (2014).

4.4 Asymmetric QD Pair

[72] R. Heitz, I. Mukhametzhanov, P. Chen, and a. Madhukar, Phys. Rev. B **58**, R10151 (1998).

4.5 Stacked QD Layers

[73] N. Gogneau, F. Fossard, E. Monroy, S. Monnoye, H. Mank, and B. Daudin, Appl. Phys. Lett. **84**, 4224 (2004).

[74] J. Tersoff, C. Teichert, and M. G. Lagally, Phys. Rev. Lett. **76**, 1675 (1996).

[75] M. Luysberg, M. Heggen, and K. Tillmann, J. Large-Scale Res. Facil. **2**, 138 (2016).

[76] M. Kruth, D. Meertens, and K. Tillmann, J. Large-Scale Res. Facil. **2**, 105 (2016).

[77] B. Daudin, G. Feuillet, H. Mariette, G. Mula, N. Pelekanos, E. Molva, J.-L. Rouvière, C. Adelmann, - Guerrero, J. Barjon, F. Chabuel, B. Bataillou, and J. Simon, Jpn. J. Appl. Phys. **40**, 1892 (2001).

[78] S. Sergent, S. Kako, M. Bürger, D. J. As, and Y. Arakawa, Appl. Phys. Lett. **103**, 151109 (2013).

[79] K. Hoshino, S. Kako, and Y. Arakawa, Appl. Phys. Lett. **85**, 1262 (2004).

5 Nextnano++ Simulations of c-GaN QDs

[80] S. Birner, S. Hackenbuchner, M. Sabathil, G. Zandler, J. A. Majewski, T. Andlauer, T. Zibold, R. Morschl, A. Trellakis, and P. Vogl, Acta Phys. Pol. A **110**, 111 (2006).

[81] I. Vurgaftman and J. R. Meyer, J. Appl. Phys. **94**, 3675 (2003).

[82] T. Wecker, F. Hörich, M. Feneberg, R. Goldhahn, D. Reuter, and D. J. As, Phys. Status Solidi **252**, 873 (2015).

6 Photonic Crystal Membranes

[83] R. Windisch, P. Heremans, A. Knobloch, P. Kiesel, G. H. Döhler, B. Dutta, and G. Borghs, Appl. Phys. Lett. **74**, 2256 (1999).

[84] S. Sergent, M. Arita, S. Kako, K. Tanabe, S. Iwamoto, and Y. Arakawa, Appl.

Phys. Lett. **101**, 101106 (2012).

[85] R. Padjen, J. M. Gerard, and J. Y. Marzin, J. Mod. Opt. **41**, 295 (1994).

[86] J. D. Joannopoulos, R. D. Meade, and J. N. Winn, Photonic Cryst. (1995).

[87] D. Cassagne, C. Jouanin, and D. Bertho, Phys. Rev. B **52**, R22217 (1995).

[88] T. F. Krauss and R. M. De La Rue, Appl. Phys. Lett. **68**, 1613 (1996).

6.2 CST-Simulations of Modes

[89] I. Inoue and K. Ohtaka, *Photonic Crystals* (Springer, 2004).

[90] Y. Akahane, T. Asano, B.-S. Song, and S. Noda, Opt. Express **13**, 1202 (2005).

6.3 µ-PL Measurements of PC Membranes

[91] D. Néel, S. Sergent, M. Mexis, D. Sam-Giao, T. Guillet, C. Brimont, T. Bretagnon, F. Semond, B. Gayral, S. David, X. Checoury, and P. Boucaud, Appl. Phys. Lett. **98**, 261106 (2011).

8 Outlook

[92] J. Schörmann, D. J. As, K. Lischka, P. Schley, R. Goldhahn, S. F. Li, W. Löffler, M. Hetterich, H. Kalt, J. Schörmann, D. J. As, and K. Lischka, Appl. Phys. Lett. **89**, 261903 (2006).

9.7 Parameter List

[93] A. F. Wright, J. Appl. Phys. **82**, 2833 (1997).

[94] M. Landmann, E. Rauls, W. G. Schmidt, M. Röppischer, C. Cobet, N. Esser, T. Schupp, D. J. As, M. Feneberg, and R. Goldhahn, Phys. Rev. B **87**, 195210 (2013).

[95] M. Feneberg, M. F. Romero, M. Röppischer, C. Cobet, N. Esser, B. Neuschl, K. Thonke, M. Bickermann, and R. Goldhahn, Phys. Rev. B **87**, 235209 (2013).

9.4 List of Abbreviations

AQDP	Asymmetric Quantum Dot Pair
BEP	Beam Equivalent Pressure
BG	Band Gap
BOE	Buffered Oxide Etch
BZ	Brillouin Zone
c-AlN	Cubic Aluminumnitride
c-GaN	Cubic Galliumnitride
DI	Deionized
DOS	Density of States
EBL	Electron-Beam Lithography
EDX	Energy Dispersive X-Ray Spectroscopy
FIB	Focused Ion Beam
FM	Frank-van der Merwe
FWHM	Full Width Half Maximum
HAADF	High-Angle Annular Dark-Field
HF	Hydrofluoric Acid
HRTEM	High Resolution Transmission Electron Microscopy
LED	Light Emitting Diode
LQD	Lower Quantum Dot
MBE	Molecular Beam Epitaxy
ML	Monolayer
PAMBE	Plasma-Assisted Molecular Beam Epitaxy
PBG	Photonic Band Gap
PECVD	Plasma-Enhanced Chemical Vapor Deposition
PC	Photonic Crystal
PL	Photoluminescence
RF	Radiofrequency

RHEED	Reflective High Energy Electron Diffraction
rms	Root Mean Square
SEM	Scanning Electron Microscopy
sccm	Standard Cubic Centimeter
SE	Secondary Electrons
Si	Silicon
SK	Stranski-Krastanov
STEM	Scanning Transmission Electron Microscopy
TE	Transversal Electric
TEM	Transmission Electron Microscopy
TM	Transversal Magnetic
UQD	Upper Quantum Dot
Q factor	Quality factor
QD	Quantum Dot
VW	Volmer-Weber
WL	Wetting Layer
3D	Three-dimensional
2D	Two-dimensional
1D	One-dimensional
0D	Zero-dimensional
μ-PL	Micro-Photoluminescence

9.5 Temperature Calibration

This calibration has not yet been published and was carried out by Michael Deppe.

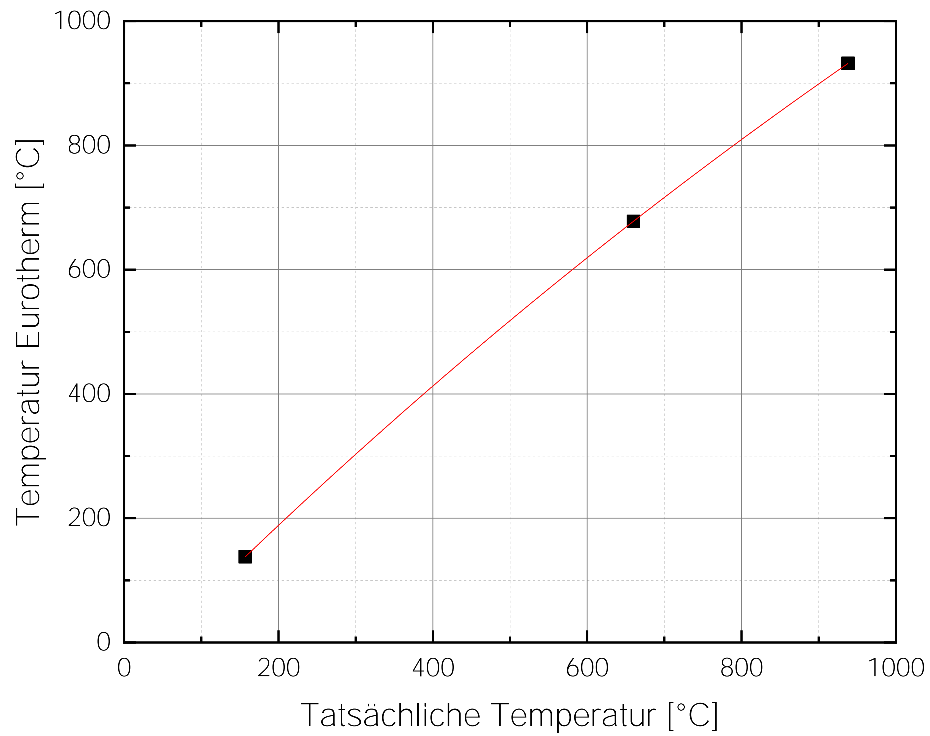

Figure 9-1: Comparison of the displayed temperature on the Eurotherm controller with the actual temperature determined from the evaporation behavior of Al, In and Ga.

9.6 Optimized PC Membranes

In the following the first results for the optimization of the PC membranes can be seen. Figure 9-2 shows an example of a L3 cavity. Other cavity designs were also used. The L3 cavity consists of three missing holes in the center. The three adjacent holes on both sides were modified. The optimization was carried out after Triviño et al. [38]. The publication shows a 65-fold increase in the Q factor by reducing the radius by $dr_{1\text{-}3}$ = [-0.0980, -0.0882, 0.0927]a and shifting the holes outwards by $S_{1\text{-}3}$ = [0.3482, 0.2476, 0.0573]a.

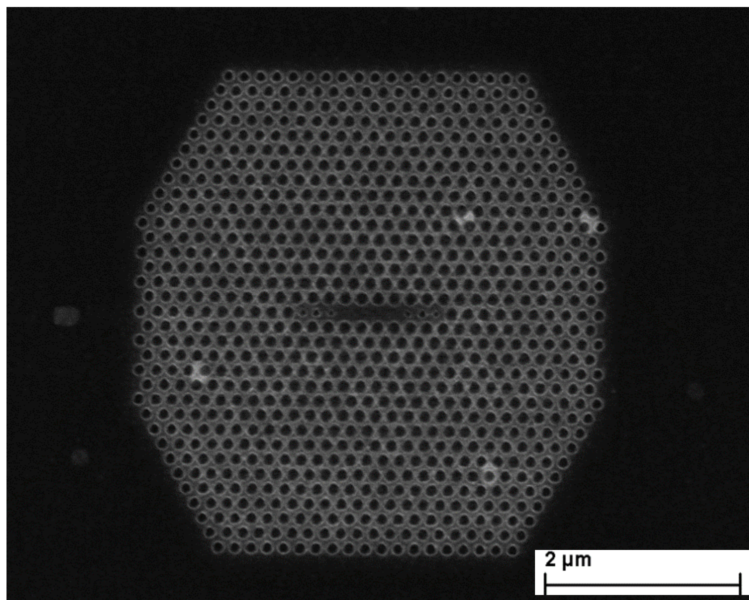

Figure 9-2: SEM picture of an optimized L3 cavity. The adjacent three holes next to the cavity have been optimized in diameter and position.

9.7 Parameter List

Parameter	c-AlN	c-GaN
$E_{gap,0K}$ [eV]	5.997[1]	3.293 [48]
$E_{gap,300K}$ [eV]	5.93 [47]	3.23 [48]
$E_{exciton}$ [meV]	-	24 [48]
a [Å]	4.373 [46]	4.503 [21]
m_e^*/m_0	0.3 [49]	0.19 [49]
m_{hh}^*/m_0	1.32 [49]	0.83 [49]
m_{lh}^*/m_0	0.44 [49]	0.28 [49]
m_{so}^*/m_0	0.55 [49]	0.34 [49]
Δ_{so} [meV]	19 [49]	15 [48]
ϵ_r	8.07 [47]	9.44 [48]
ϵ_∞	4.25 [47]	5.31 [48]
c_{11} [GPa]	304 [93]	293 [93]
c_{12} [GPa]	160 [93]	159 [93]
c_{44} [GPa]	193 [93]	155 [93]
a_g [eV]	-9.1 [50]	-8.0 [50]
$a_c=a_g+a_v$ [eV]	-6.8	-6.0
a_v [eV]	2.3 [50]	2.0 [50]
b_{uniax} [eV]	-1.5 [50]	-1.7 [50]
$b_{Bowing-direct}$ [eV]	0.85 [94]	
$b_{Bowing-indirect}$ [eV]	0.01 [94]	

[1] In h-AlN the difference in the energy gap from 0 K to 300 K is about 67 meV [81,95]. A similar value for c-AlN is assumed leading to $E_{gap,0K} = E_{gap,300K} + 67$ meV.

9.8 Nextnano++ Script

Script for transition calculations

```
$wl=1.0                          # Thickness of the wetting layer for the quantum dot
(DisplayUnit:nm)
$dotwidth=20.0                   # Width of the quantum dot (DisplayUnit:nm)
$dotwidthtop=$dotwidth/100*20                  # Width of the quantum dot
(DisplayUnit:nm)
$dotheight=1.5                  # Height of the quantum dot (DisplayUnit:nm)
$gatevoltage=-0.0                # Applied voltage at the gate contact (DisplayUnit:V)
$zspacing=1.0                    # Grid spacing in z-direction (DisplayUnit:nm)
$xspacing=2.0*$zspacing          # Grid spacing in x-direction
(DisplayUnit:nm)(DoNotShowInUserInterface)
$yspacing=2.0*$zspacing          # Grid spacing in y-direction
(DisplayUnit:nm)(DoNotShowInUserInterface)
$spacing=0.5                     # Grid spacing for the each direction if globally
uniform grid (DisplayUnit:nm)(DoNotShowInUserInterface)
$addSpace=15.0                   # Distance from the QD-boundaries to the boundary of the
quantum region (DisplayUnit:nm)
$safetyDistTop=30.0              # Safety distance from the top/bottom QR-boundary to the
CN-contacts (DisplayUnit:nm) Overwrite 30
$safetyDistXY=15                 # Safety distance from the x-/y-QR-boundary to the x-/y-
boundary of the simulation space (DisplayUnit:nm)

##################################################################
#                                                                #
#      Derived Parameters for the computational domain           #
#                                                                #
##################################################################
$qrxwidth=$dotwidth+2.0*$addSpace      # Width of the quantum region in x-direction
(DisplayUnit:nm)(DoNotShowInUserInterface)
$qrywidth=$dotwidth+2.0*$addSpace      # Width of the quantum region in y-direction
(DisplayUnit:nm)(DoNotShowInUserInterface)
$qrzwidth=$wl+$dotheight+2.0*$addSpace # Width of the quantum region in z-direction
(DisplayUnit:nm)(DoNotShowInUserInterface)

$lowerqrx=-$qrxwidth/2.0  # Lower x-boundary of the quantum region
(DoNotShowInUserInterface)
$upperqrx=$qrxwidth/2.0   # Upper x-boundary of the quantum region
(DoNotShowInUserInterface)
$lowerqry=-$qrywidth/2.0  # Lower y-boundary of the quantum region
(DoNotShowInUserInterface)
$upperqry=$qrywidth/2.0   # Upper y-boundary of the quantum region
(DoNotShowInUserInterface)
$lowerqrz=-$qrzwidth/2.0  # Lower z-boundary of the quantum region
(DoNotShowInUserInterface)
$upperqrz=$qrzwidth/2.0   # Upper z-boundary of the quantum region
(DoNotShowInUserInterface)

$xwidth=$qrxwidth+2.0*$safetyDistXY  # Total width of the simulation space in x-
direction (DisplayUnit:nm) (DoNotShowInUserInterface)
$ywidth=$qrywidth+2.0*$safetyDistXY  # Total width of the simulation space in y-
direction (DisplayUnit:nm) (DoNotShowInUserInterface)
$zwidth=$qrzwidth+2.0*$safetyDistTop # Total width of the simulation space in z-
direction (DisplayUnit:nm) (DoNotShowInUserInterface)

##################################################################
#                                                                #
# Position the QD in the middle of the simulation domain         #
#                                                                #
##################################################################
$xcenter=0.0                      # x-coordinate of the center of the simulation space
(DisplayUnit:nm) (DoNotShowInUserInterface)
$ycenter=0.0                      # y-coordinate of the center of the simulation space
(DisplayUnit:nm) (DoNotShowInUserInterface)
$zcenter=0.0                      # z-coordinate of the center of the simulation space
(DisplayUnit:nm) (DoNotShowInUserInterface)

$ztop=$zcenter+0.5*$dotheight     # Top z-coordinate of the QD (DisplayUnit:nm)
(DoNotShowInUserInterface)
$zbottom=$ztop-$dotheight         # Bottom z-coordinate of the QD (DisplayUnit:nm)
(DoNotShowInUserInterface)
```

```
$lowerx=$xcenter-$dotwidth/2.0   # Lower x-coordinate of the QD (DisplayUnit:nm)
(DoNotShowInUserInterface)
$upperx=$xcenter+$dotwidth/2.0   # Upper x-coordinate of the QD (DisplayUnit:nm)
(DoNotShowInUserInterface)
$lowery=$ycenter-$dotwidth/2.0   # Lower y-coordinate of the QD (DisplayUnit:nm)
(DoNotShowInUserInterface)
$uppery=$ycenter+$dotwidth/2.0   # Upper y-coordinate of the QD (DisplayUnit:nm)
(DoNotShowInUserInterface)

$lowerxt=$xcenter-$dotwidthtop/2.0   # Lower x-coordinate of the QD (DisplayUnit:nm)
(DoNotShowInUserInterface)
$upperxt=$xcenter+$dotwidthtop/2.0   # Upper x-coordinate of the QD (DisplayUnit:nm)
(DoNotShowInUserInterface)
$loweryt=$ycenter-$dotwidthtop/2.0   # Lower y-coordinate of the QD (DisplayUnit:nm)
(DoNotShowInUserInterface)
$upperyt=$ycenter+$dotwidthtop/2.0   # Upper y-coordinate of the QD (DisplayUnit:nm)
(DoNotShowInUserInterface)


#################################################################
#                                                               #
# Setting fixed coordinates which are used for generation of the #
# grid.                                                         #
#                                                               #
#################################################################
$firstx=$lowerqrx-$safetyDistXY          #(DisplayUnit:nm)(DoNotShowInUserInterface)
$secondx=$lowerx                         #(DisplayUnit:nm)(DoNotShowInUserInterface)
$thirdx=$xcenter                         #(DisplayUnit:nm)(DoNotShowInUserInterface)
$fourthx=$upperx                         #(DisplayUnit:nm)(DoNotShowInUserInterface)
$fifthx=$upperqrx+$safetyDistXY          #(DisplayUnit:nm)(DoNotShowInUserInterface)
$lastx=$fifthx                           #(DisplayUnit:nm)(DoNotShowInUserInterface)

$firsty=$lowerqry-$safetyDistXY          #(DisplayUnit:nm)(DoNotShowInUserInterface)
$secondy=$lowery                         #(DisplayUnit:nm)(DoNotShowInUserInterface)
$thirdy=$ycenter                         #(DisplayUnit:nm)(DoNotShowInUserInterface)
$fourthy=$uppery                         #(DisplayUnit:nm)(DoNotShowInUserInterface)
$fifthy=$upperqry+$safetyDistXY          #(DisplayUnit:nm)(DoNotShowInUserInterface)
$lasty=$fifthy                           #(DisplayUnit:nm)(DoNotShowInUserInterface)

$firstz=$lowerqrz-$safetyDistTop         #(DisplayUnit:nm)(DoNotShowInUserInterface)
$secondz=$firstz+1.0                     #(DisplayUnit:nm)(DoNotShowInUserInterface)
$thirdz=$zbottom-$wl                     #(DisplayUnit:nm)(DoNotShowInUserInterface)
$fourthz=$zbottom                        #(DisplayUnit:nm)(DoNotShowInUserInterface)
$fifthz=$zcenter                         #(DisplayUnit:nm)(DoNotShowInUserInterface)
$sixthz=$ztop                            #(DisplayUnit:nm)(DoNotShowInUserInterface)
$seventhz=$upperqrz+$safetyDistTop-1.0   #(DisplayUnit:nm)(DoNotShowInUserInterface)
$eighthz=$upperqrz+$safetyDistTop        #(DisplayUnit:nm)(DoNotShowInUserInterface)
$lastz=$eighthz                          #(DisplayUnit:nm)(DoNotShowInUserInterface)

#################################################################
#                                                               #
# Setup of global parameters making the crystal cs coincide with #
# the computational cs (pretty crucial for postprocessing)      #
#                                                               #
#################################################################
global{
    simulate3D{}
    crystal_zb{
            x_hkl = [1,0,0]
            y_hkl = [0,1,0]
    }
    substrate{
        name="AlN_zb"
    }
    temperature = 300
}

#################################################################
#                                                               #
#  Specification of the structure and structure related output  #
#                                                               #
#################################################################
structure{
    region{ #1
        cuboid{
            x = [ $firstx , $lastx ]
            y = [ $firsty , $lasty ]
            z = [ $firstz , $lastz ]
```

```
        }
        binary{
            name = "AlN_zb"
        }
    }
      region{ #2 Wetting layer of the QD
            cuboid{
                  x = [$firstx,$lastx]
                  y = [$firsty, $lasty ]
                  z = [$thirdz, $fourthz ]
            }
            binary{
                  name = "GaN_zb"
            }
      }
    region{ #3 The QD
        obelisk{
            base_x = [ $lowerxt,$upperxt ]
            base_y = [ $loweryt,$upperyt ]
                   base_z = [ $dotheight, $dotheight]
            top_x = [ $lowerx,$upperx ]
            top_y = [ $lowery, $uppery ]
                   top_z = [$fourthz,$fourthz]
         }
           binary{
                   name = "GaN_zb"
           }
    }
      region{ #4 AlN
         cuboid{
            x = [$firstx, $lastx ]
            y = [$firsty, $lasty ]
            z = [$firstz, $secondz]
         }
         binary{
            name = AlN_zb
         }
         contact{name="AlN"}
      }
      region{ #7 g
         cuboid{
            x=[$firstx,$lastx]
            y=[$firsty,$lasty]
            z=[$seventhz,$lastz]
         }
         contact{name="g"}
      }
}

##################################################################
#                                                                #
# Specification of the computational grid and boundary conditions#
#                                                                #
##################################################################
grid{
    xgrid{
             line{ pos=$firstx spacing = $xspacing}
             line{ pos=$secondx spacing = $xspacing}
             line{ pos=$thirdx spacing = $xspacing}
             line{ pos=$fourthx spacing = $xspacing}
             line{ pos=$fifthx spacing = $xspacing}
    }
    ygrid{
             line{ pos = $firsty spacing = $yspacing}
             line{ pos = $secondy spacing = $yspacing}
             line{ pos = $thirdy spacing = $yspacing }
             line{ pos = $fourthy spacing = $yspacing }
             line{ pos = $fifthy spacing = $yspacing }
    }
    zgrid{
             line{ pos = $firstz spacing = $zspacing }
             line{ pos = $secondz spacing = $zspacing }
             line{ pos = $thirdz spacing = $zspacing }
             line{ pos = $fourthz spacing = $zspacing }
             line{ pos = $fifthz spacing = $zspacing }
             line{ pos = $sixthz spacing = $zspacing }
             line{ pos = $seventhz spacing = $zspacing }
             line{ pos = $eighthz spacing = $zspacing }
```

```
    }
      periodic{
         x=yes
         y=yes
         z=no
      }
}

##################################################################
#                                                                #
# Specifications for the solution of classical Poisson equation  #
#                                                                #
##################################################################
classical{
    Gamma{}
    L{}
    X{}
    HH{}
    LH{}
    SO{}
      output_bandedges{
         averaged=no
      }
}

##################################################################
#                                                                #
# Specifications for strain calculation                          #
#                                                                #
##################################################################
strain{
    minimized_strain{}
    growth_direction=[0,0,1]

    linear_solver{
        iterations = 1000
        abs_accuracy = 1e-8
        rel_accuracy = 1e-12
        use_cscg = yes
    }
}

##################################################################
#                                                                #
# Specifications for solution of the nonlinear Poisson equation  #
#                                                                #
##################################################################
poisson{
    newton_solver{
        iterations=1000
        search_steps=100
        residual=1e-4
    }
    linear_solver{
        iterations = 1000
        abs_accuracy = 1e-8
        rel_accuracy = 1e-13
        use_cscg = no
    }
    bisection{
        delta=5
        iterations=20
        residual=1e18
    }
}

##################################################################
#                                                                #
# Specification of the used quantum model                        #
#                                                                #
##################################################################
quantum{
    region{
        name="qr1"
        no_density=no
        x=[ $lowerqrx , $upperqrx ]
        y=[ $lowerqry , $upperqry ]
        z=[ $lowerqrz , $upperqrz ]
```

```
        output_wavefunctions{
            max_num = 100
            probabilities=yes
                   amplitudes=no
        }
        kp_8band{
            num_electrons=2
            num_holes=2
            accuracy=1e-9
            iterations=1000
            arpack_inv{}
            linear_solver{
                iterations=1000
                abs_accuracy=1e-8
                rel_accuracy=1e-8
            }
        }
    }
}

##################################################################
#                                                                #
#   Specification of contacts, i.e. boundary conditions for the  #
#   solution of the nonlinear Poisson equation                   #
#   (Try ohmic for BC and Schottky for gate)                     #
#                                                                #
##################################################################
contacts{
   charge_neutral{
      name="Backcontact"
      bias=0.0
   }
   charge_neutral{
      name="Gate"
      bias=$gatevoltage
      #bias=[-$gatevoltage,$gatevoltage]
      #steps=10
   }
}



database{
     ######### gallium nitride (zincblende) ################################
binary_zb {
    name     = GaN_zb
    valence = III_V

    lattice_consts{
        a           = 4.50                                  # Vurgaftman1/Vurgaftman2
(300 K)
        a_expansion = 0                                     # ?
    }

    dielectric_consts{
        static_a   = 9.7                                    #
http://www.ioffe.rssi.ru/SVA/NSM/Semicond/GaN/optic.html  Bougrov et al. (2001)  (300 K)
        optical_a = 5.3                                     # high frequency (300 K)
    }

    elastic_consts{
        c11 = 293    c12 = 159    c44 = 155                 # Vurgaftman1/Vurgaftman2
    }

    piezoelectric_consts{
        e14 = 0.56                                          # taken from M. Shur
http://nina.ecse.rpi.edu/shur/Tutorial/GaNtutorial1/sld038.htm
    }

    conduction_bands{
       Gamma{
          mass                  = 0.15                      # Vurgaftman1/Vurgaftman2
          bandgap               = 3.299                     # Vurgaftman2 (0 K)
          bandgap_alpha         = 0.593e-3                  # Vurgaftman2
          bandgap_beta          = 600                       # Vurgaftman2
        # defpot_absolute       = -6.71                     # Vurgaftman2
```

```
         defpot_absolute        = -6.68                       # A. Zunger: a_c = a_v +
a_gap = 0.69 - 7.37 = -6.68
       }
       L{
          mass_l               = 0.2                          # ?
          mass_t               = 0.2                          # ?
          bandgap              = 5.59                         # Vurgaftman2 (0 K)
          bandgap_alpha        = 0.593e-3                     # Vurgaftman2
          bandgap_beta         = 600                          # Vurgaftman2
          defpot_absolute      = -7.46                        # A. Zunger: a_c = a_v +
a_gap = 0.69 - 8.15 = -7.46
          defpot_uniaxial      = 14.26                        # GaAs value
       }
       X{
          mass_l               = 0.5                          # Vurgaftman1/Vurgaftman2
          mass_t               = 0.3                          # Vurgaftman1/Vurgaftman2
          bandgap              = 4.52                         # Vurgaftman2 (0 K)
          bandgap_alpha        = 0.593e-3                     # Vurgaftman2
          bandgap_beta         = 600                          # Vurgaftman2
          defpot_absolute      = -0.52                        # A. Zunger: a_c = a_v +
a_gap = 0.69 - 1.21 = -0.52
          defpot_uniaxial      = 6.5                          # GaAs value
       }
    }

    valence_bands{
        bandoffset          = -0.726                          # A. Zunger

        HH{ mass            = 1.3   }                         #
http://www.ioffe.rssi.ru/SVA/NSM/Semicond/GaN/bandstr.html Leszczynski et al. (1996),
Fan et al. (1996)
        LH{ mass            = 0.19  }                         #
http://www.ioffe.rssi.ru/SVA/NSM/Semicond/GaN/bandstr.html Leszczynski et al. (1996),
Fan et al. (1996)
        SO{ mass            = 0.29  }                         # Vurgaftman1/Vurgaftman2

        defpot_absolute   =  0.69                             # A. Zunger/Vurgaftman2:
a_v  -  Note that Vurgaftman1/Vurgaftman2 has different sign convention. => -0.69
        defpot_uniaxial_b = -2.0   defpot_uniaxial_d = -3.7   # Vurgaftman2

        delta_SO            = 0.017                           # Vurgaftman1/Vurgaftman2

    }

    kp_6_bands{
      # gamma1 = 2.70   gamma2 = 0.76   gamma3 = 1.11         # Vurgaftman2
        L = -6.74       M = -2.18       N = -6.66
    }

    kp_8_bands{                                               # bandgap(Gamma) = 3.299
        S = -0.90                                             # S = 1 + 2F = 1 + 2 (-
0.95) = -0.90 (Vurgaftman2)
        E_P = 25.0                                            # Vurgaftman1/Vurgaftman2
        B =   0
        L =   0.825    M = -2.18    N = 0.905
    }

    mobility_constant{
        electrons{  mumax = 100      exponent = 1.0  }        #
        holes{      mumax = 100      exponent = 1.0  }        #
    }

    recombination{
        SRH{        tau_n = 1.0e-9      nref_n = 1.0e19       # InP value !!!
                    tau_p = 1.0e-9      nref_p = 1.0e18       # InP value !!!
        }
        Auger{      c_n = 0             c_p = 0               # InP value !!!
        }
        radiative{  c = 0                                     # ?
        }
    }
}

######### aluminum nitride (zincblende) ###############################
binary_zb {
    name     = AlN_zb
    valence = III_V
```

```
    lattice_consts{
        a           = 4.38                                  # Vurgaftman1/Vurgaftman2
(300 K)
        a_expansion = 0                                     # ?
    }

     dielectric_consts{
        static_a  = 9.14                                    # ? Landolt-Boernstein
epsilon(0) wurtzite, Collins et al. (1967)
        optical_a = 4.84                                    # ? Landolt-Boernstein
epsilon(infinity) wurtzite, Collins et al. (1967)
    }

    elastic_consts{
        c11 = 304   c12 = 160   c44 = 193                   # Vurgaftman1/Vurgaftman2
    }

    piezoelectric_consts{
        e14 = 0.92                                          # ? taken from M. Shur
http://nina.ecse.rpi.edu/shur/Tutorial/GaNtutorial1/sld038.htm (wurtzite)
    }

    conduction_bands{
       Gamma{
          mass                  = 0.25                      # Vurgaftman1/Vurgaftman2
          bandgap               = 5.4                       # Vurgaftman2 (0 K)
          bandgap_alpha         = 0.593e-3                  # Vurgaftman2
          bandgap_beta          = 600                       # Vurgaftman2
        # defpot_absolute       = -4.5                      # Vurgaftman2
          defpot_absolute       = -5.22                     # A. Zunger: a_c = a_v +
a_gap = 4.94 - 10.16 = -5.22
       }
       L{
          mass_l                = 0.2                       # ?
          mass_t                = 0.2                       # ?
          bandgap               = 9.3                       # Vurgaftman2 (0 K)
          bandgap_alpha         = 0.593e-3                  # Vurgaftman2
          bandgap_beta          = 600                       # Vurgaftman2
          defpot_absolute       = -4.95                     # A. Zunger: a_c = a_v +
a_gap = 4.94 - 9.89 = -4.95
          defpot_uniaxial       = 14.26                     # GaAs value
       }
       X{
          mass_l                = 0.53                      # Vurgaftman1/Vurgaftman2
          mass_t                = 0.31                      # Vurgaftman1/Vurgaftman2
          bandgap               = 4.9                       # Vurgaftman2 (0 K)
          bandgap_alpha         = 0.593e-3                  # Vurgaftman2
          bandgap_beta          = 600                       # Vurgaftman2
          defpot_absolute       = 3.81                      # A. Zunger: a_c = a_v +
a_gap = 4.94 - 1.13 = -3.81
          defpot_uniaxial       = 6.5                       # GaAs value
       }
    }

    valence_bands{
        bandoffset        = -1.526                          # A. Zunger

        HH{ mass          = 0.3   }                         # ?
        LH{ mass          = 0.3   }                         # ?
        SO{ mass          = 0.47  }                         # Vurgaftman1/Vurgaftman2

        defpot_absolute   =  4.94                           # A. Zunger: a_v
      # defpot_absolute   =  4.9                            # Vurgaftman2 - Note that
Vurgaftman1/Vurgaftman2 has different sign convention. => -4.9
        defpot_uniaxial_b = -1.7   defpot_uniaxial_d = -5.5     # Vurgaftman2

        delta_SO          = 0.019                           # Vurgaftman1/Vurgaftman2

    }

    kp_6_bands{
      # gamma1 = 1.92    gamma2 = 0.47    gamma3 = 0.85        # Vurgaftman1/Vurgaftman2
        L = -4.80        M = -1.98        N = -5.10
    }

    kp_8_bands{                                             # bandgap(Gamma) = 5.4
(Vurgaftman2)
```

```
        S = -1.02                                                 # S = 1 + 2F = 1 + 2 (-
1.01) = -1.02 (Vurgaftman2)
        E_P = 27.1                                                # Vurgaftman1/Vurgaftman2
        B =  0
        L =  0.213   M = -1.98   N = -0.087
    }

    mobility_constant{
        electrons{  mumax = 100      exponent = 1.0  }            #
        holes{      mumax = 100      exponent = 1.0  }            #
    }

    recombination{
        SRH{       tau_n = 1.0e-9      nref_n = 1.0e19            # InP value !!!
                   tau_p = 1.0e-9      nref_p = 1.0e18            # InP value !!!
        }
        Auger{     c_n = 0             c_p = 0                    # InP value !!!
        }
        radiative{ c = 0                                          # ?
        }
    }
}
}


   output{
      format3D=VTKAscii
   }
run{
    solve_strain{}
      solve_poisson{}
      solve_quantum{}
      outer_iteration{}
}
```

9.9 List of Samples

Sample No.	Date	Substrate	Layer	Measurements	Patter-ning	Comments
2433	14.04.2014	12CO-056	30 nm AlN, 20s GaN QDs, 30 nm AlN	Pl: 3.59 eV	MD, PC3, PC4, PC6	¼ Thomas Czerniuk
2434	15.04.2014	12CO-056	50 nm AlN, 20 s GaN QDs, 50 nm AlN	Pl: 3.64 eV		Japan (8x10mm)
2435	15.04.2014	12CO-056	30 nm AlN, uncapped GaN QDs 15 s	AFM		
2436	16.04.2014	12CO-056	50 nm AlN, 20 s GaN QDs, 50 nm AlN	Pl: 3.83 eV		BA Falco (10x10mm)
2437	22.04.2014	12CO-056	30 nm AlN, 15s GaN QDs, 30 nm AlN	Pl: 4.1 eV	PC1-break, PC2	¼ Shovon Pal (Bochum), ¼ M. Rüsing
2438	28.04.2014	12CO-056	50 nm AlN, 25 s GaN QDs, 50 nm AlN	Pl: 3.54 eV		Japan (8x10mm)
2439	30.04.2014	12CO-056	Stacked QDs, AlN: 4x15 nm, QDs 20s	Pl: 3.67 eV		
2471	24.07.2014	12CO-056	30 nm AlN, 20s GaN QDs, 30 nm AlN			Michael Rüsing (10x10mm)
2472	07.08.2014	12CO-056	30 nm AlN, 20s GaN QDs, 30 nm AlN			
2473	11.08.2014	12CO-056	30 nm AlN, 20s GaN QDs, 30 nm AlN	Pl: 3.86 eV		BA Falco
2474	12.08.2014	12CO-056	30 nm AlN, 20s GaN QDs, 30 nm AlN	Pl: 4.26 eV (I: 600 cps)		
2475	13.08.2014	12CO-056	50 nm AlN, 20 s GaN QDs, 50 nm AlN	Pl: 4.04 eV		BA Falco
2476	19.08.2014	12CO-056	30 nm AlN, 25s GaN QDs, 30 nm AlN	Pl: no signal		
2477	21.08.2014	12CO-056	30 nm AlN, 25s GaN QDs, 30 nm AlN	Pl: 3.71 eV (low intensity)		
2478	21.08.2014	12CO-056	100 nm AlN	AFM		New Zeeland (5x10mm)
2479	02.09.2014	12CO-056	30 nm AlN, 25s GaN QDs, 30 nm AlN	Pl: 3.82 eV		¼ Shovon Pal (Bochum)

2480	02.09.2014	12CO-056	30 nm AlN, 25s GaN QDs, 30 nm AlN	Pl: no signal		
2481	03.09.2014	12CO-056	Waveguide: 150 nm AlN, 175 nm GaN, 100 nm AlN	Pl: 3.24 eV, XRD: (002), (113)		Dortmund (5x10mm)
2482	04.09.2014	12CO-056	30 nm AlN, 25s GaN QDs, 30 nm AlN	Pl: 3.82 eV		C. Rothfuchs (Bochum) (10x10mm)
2483	09.09.2014	12CO-056	Waveguide: 150 nm AlN, 175 nm GaN, 100 nm AlN	Pl: 3.24 eV, XRD: (002), (113)		Dortmund, AlN low Temp (5x10mm)(T= 790°C)
2484	11.09.2014	12CO-056	30 nm AlN, 30s GaN QDs, 30 nm AlN	Pl: 3.69 eV	PC7, PC8	¼ R. Grothemeyer, ¼ M. Rüsing
2485	18.09.2014	12CO-056	Waveguide: 250 nm AlGaN, 175 nm GaN, 100 nm AlGaN	XRD: (002), (113)		Dortmund (5x10mm)
2495	20.11.2014	12CO-056	50 nm AlN, 20 s GaN QDs, 50 nm AlN	Pl: no signal		
2496	20.11.2014	12CO-056	50 nm AlN, 25 s GaN QDs, 50 nm AlN	Pl: no signal	PC-test-groß	
2497	25.11.2014	12CO-056	30 nm AlN, 25s GaN QDs, 30 nm AlN	Pl: 3.71 eV		
2498	26.11.2014	12CO-056	30 nm AlN, 25s GaN QDs, 30 nm AlN	Pl: 3.85 eV		BA Falco
2499	01.12.2014	12CO-056	50 nm AlN, 25 s GaN QDs, 50 nm AlN	Pl: 3.8 eV (low I)		
2500	03.12.2014	12CO-056	50 nm AlN, 25 s GaN QDs, 50 nm AlN	Pl: no signal		
2501	05.12.2014	12CO-056	50 nm AlN, 25 s GaN QDs, 50 nm AlN	Pl: 3.63 eV		Sylvain Sergent (8x10mm)
2505	07.01.2015	12CO-056	30 nm AlN, 25s GaN QDs, 30 nm AlN		PC9, Pi1, PC10	
2506	09.01.2015	12CO-056	60 nm AlN	AFM		¼ Shovon Pal (Bochum)

2507	12.01.2015	12CO-056	30 nm AlN, 25s GaN QDs, 30 nm AlN	Pl: low I		Test
2508	12.01.2015	12CO-056	30 nm AlN, 25s GaN QDs, 30 nm AlN	Pl: low I		Test
2509	13.01.2015	12CO-056	30 nm AlN, 25s GaN QDs, 30 nm AlN	Pl: low I		Test
2526	19.05.2015	12CO-056	3 nm AlN			Test
2527	26.05.2015	12CO-056	10 nm AlN			Test
2528	10.06.2015	12CO-056	2 nm AlN			Test
2529	12.06.2015	12CO-056	60 nm GaN, 10 nm AlGaN (x=0.3)			
2530	15.06.2015	12CO-056	30 nm AlN, 25s GaN QDs, 30 nm AlN			
2531	16.06.2015	12CO-056	Stacked QDs: 10x GaN QDs 20s, je 10 nm AlN	AFM		
2532	17.06.2015	12CO-056	Stacked QDs: 6x GaN QDs 20s, je 10 nm AlN	AFM		
2533	18.06.2015	12CO-056	30 nm AlN, 25s GaN QDs, 30 nm AlN			
2537	03.07.2015	12CO-056	30 nm AlN, uncapped GaN QDs 25 s	AFM		
2538	09.07.2015	12CO-056	30 nm AlN, uncapped GaN QDs 25 s	AFM		
2539	09.07.2015	12CO-056	100 nm AlN			New Zeeland (10x10mm)
2540	09.07.2015	12CO-056	30 nm AlN, uncapped GaN QDs 25 s	AFM		Mahesh Kumar (10x10mm)
2541	13.07.2015	12CO-056	Stacked QDs: 6x GaN QDs 20s, je 10 nm AlN	Pl: 3.68 eV, AFM	PC11	
2546	21.08.2015	UniPad10-04	7 nm AlN			Test
2547	21.08.2015	UniPad10-04	7 nm AlN			Test
2555	09.09.2015	UniPad10-04	100 nm AlN	AFM		
2558	14.09.2015	11CO-063	100 nm AlN	AFM		New Zeeland (10x10mm)

2563	25.09.2015	11CO-063	100 nm AlN	AFM		New Zeeland (10x10mm)
2575	20.10.2015	11CO-063	50 nm AlN, 25 s GaN QDs, 50 nm AlN	Pl: no signal		
2576	20.10.2015	11CO-063	50 nm AlN, 25 s GaN QDs, 50 nm AlN	Pl: no signal		
2577	21.10.2015	11CO-063	Stacked QDs: 3x GaN QDs 25s, je 25 nm AlN	Pl: no signal		
2578	21.10.2015	11CO-063	Stacked QDs: 3x GaN QDs (1: 25s (high Al T), 2. 25s (low Al T), 3. 35 s), je 16 nm AlN	Pl: Peaks at 4.21 eV, 4.06 eV, 3.75 eV, AFM		
2579	21.10.2015	11CO-063	30 nm AlN, 25s GaN QDs, 30 nm AlN	Pl: 3.71 eV (low I)		
2580	21.10.2015	11CO-063	Stacked QDs: 3x GaN QDs 25s, je 16 nm AlN	Pl: 3.82 eV, AFM		
2581	21.10.2015	11CO-063	Stacked QDs: 6x GaN QDs 25s, je 14.5 nm AlN	Pl: 3.70 eV		
2582	29.10.2015	11CO-063	50 nm AlN, 25 s GaN QDs, 50 nm AlN	Pl: 3.68 eV	Waveguide	¼ Attolight
2583	08.12.2015	11CO-063	10 nm AlN			Test
2584	09.12.2015	11CO-063	10 nm AlN			Test
2585	09.12.2015	11CO-063	10 nm AlN			Test
2586	10.12.2015	11CO-063	10 nm AlN			Test
2592	14.01.2016	11CO-063	30 nm AlN, 25s GaN QDs, 30 nm AlN	Pl: 3.56 eV (low I)		¼ Si3N4
2593	15.01.2016	11CO-063	30 nm AlN, 25s GaN QDs, 30 nm AlN	Pl: 3.62 eV		
2595	19.01.2016	11CO-063	Stacked QDs: 10x GaN QDs 25s+ Top QDs, je 15 nm AlN	Pl: 3.63 eV, AFM		
2596	19.01.2016	11CO-063	Stacked QDs: 5x GaN QDs 25s+ Top QDs, je 15 nm AlN	Pl: 3.66 eV, AFM		
2598	21.01.2016	11CO-063	Stacked QDs: 7x GaN QDs 25s+ Top QDs, je 15 nm AlN	Pl: 3.68 eV, AFM		

2601	29.01.2016	11CO-063	Stacked QDs: 3x GaN QDs 20s+ Top QDs, je 15 nm AlN	Pl: weak I		
2602	02.02.2016	11CO-063	Stacked QDs: 5x GaN QDs 25s+ Top QDs, je 15 nm AlN	Pl: 6.65 eV, AFM		
2605	10.02.2016	11CO-063	Stacked QDs: 7x GaN QDs 25s+ Top QDs, je 15 nm AlN	Pl: no signal		
2606	11.02.2016	11CO-063	Stacked QDs: 4x GaN QDs 25s+ Top QDs, je 15 nm AlN	Pl: no signal		
2607	12.02.2016	11CO-063	Stacked QDs: 7x GaN QDs 25s+ Top QDs, je 15 nm AlN	Pl: no signal		
2609	16.02.2016	11CO-063	100 AlN			
2611	23.02.2016	11CO-063	Stacked QDs: 8x GaN QDs 25s+ Top QDs, je 15 nm AlN	Pl: 3.73 eV (I: 100,000 cps), TEM		
2615	01.03.2016	11CO-063	Stacked QDs: 5x GaN QDs 25s+ Top QDs, je 15 nm AlN	Pl: 3.64 eV (I: 50,000 cps)		
2616	02.03.2016	11CO-063	Stacked QDs: 3x GaN QDs 25s+ Top QDs, je 15 nm AlN	Pl: 3.71 eV (low I)		
2617	03.03.2016	11CO-063	15 nm AlN, 25 s GaN QDs, 15 nm AlN, 25 s GaN TOP QDs	Pl: no signal		
2622	06.04.2016	11CO-063	160 nm AlN	AFM		¼ Ulm
2623	06.04.2016	11CO-063	230 nm AlN	AFM, XRD (002)		¼ Ulm
2624	07.04.2016	11CO-063	22 nm AlN, 25s GaN QDs, 18 nm AlN	AFM		
2626	13.04.2016	11CO-063	Stacked QDs: 6x GaN QDs 25s+ Top QDs, je 15 nm AlN	Pl: 3.63 eV		
2627	14.04.2016	11CO-063	Stacked QDs: 7x GaN QDs 25s+ Top QDs, je 15 nm AlN	Pl: 3.61 eV, AFM		

2628	15.04.2016	11CO-063	Stacked QDs: 13x GaN QDs 25s+ Top QDs, je 15 nm AlN	Pl: 3.71 eV, Power dependent PL 5-40 mW, AFM, TEM		
2629	19.04.2016	11CO-063	Stacked QDs: 10x GaN QDs 25s+ Top QDs, je 15 nm AlN			destroyed
2632	25.04.2016	11CO-063	Stacked QDs: 10x GaN QDs 25s+ Top QDs, je 15 nm AlN	Pl: 3.69 eV (I:230,000 cps)	PC20	
2647	21.06.2016	11CO-063	50 nm AlN, 15 s GaN QDs, 50 nm AlN			
2648	22.06.2016	11CO-063	30 nm AlN, 15 s GaN QDs, 20 nm AlN			
2657	26.07.2016	14CO-050	QW: 30 nm AlN, 41 s GaN QW, 30 nm AlN	Pl: 3.68 eV, AFM		
2658	27.07.2016	14CO-050	Uncoupled MQW: 30 nm AlN buffer, 5 nm AlN spacer, 30 nm AlN toplayer, 2x41 s GaN QW	Pl: 3.61 eV, AFM		
2659	28.07.2016	14CO-050	Coupled MQW: 30 nm AlN buffer, 2 nm AlN spacer, 30 nm AlN toplayer, 2x41 s GaN QW	Pl: 3.52 eV, AFM		
2660	29.07.2016	14CO-050	Coupled DQDs: 30 nm AlN buffer, 2 nm AlN spacer, 30 nm AlN top, 2x20 s GaN QDs	Pl: 3.72 eV, AFM		
2661	02.08.2016	14CO-050	Stacked QDs: 5x GaN QDs 20s+ Top QDs, 30 nm AlN buffer, 4 nm AlN spacer, 30 nm AlN top	Pl: 3.69 eV (I:60,000 cps)	PC12, 13, 14, 14, 16, 17, 18, 19	
2662	04.08.2016	14CO-050	Stacked QDs: 5x GaN QDs 20s+ Top QDs, 30 nm AlN buffer, 10 nm AlN spacer, 30 nm AlN top	Pl: no signal		

2663	09.08.2016	14CO-050	Stacked QDs: 5x GaN QDs 20s+ Top QDs, 30 nm AlN buffer, 10 nm AlN spacer, 30 nm AlN top	Pl: 3.68 eV (I:30,000 cps)		
2664	14.09.2016	14CO-050	30 nm AlN, 20 s GaN QDs, 30 nm AlN	Pl: no signal		
2676	09.11.2016	14CO-050	Coupled ADQDs: 30 nm AlN buffer, 2 nm AlN spacer, 30 nm AlN top, 20 s+30 s GaN QDs	Pl: 3.59 (I:16,000 cps)		
2677	09.11.2016	14CO-050	Uncoupled ADQDs: 30 nm AlN buffer, 20 nm AlN spacer, 30 nm AlN top, 20 s+30 s GaN QDs	Pl: 3.58 eV (I:45,000 cps)		
2681	16.11.2016	14CO-050	30 nm AlN, 20 s GaN QDs, 30 nm AlN	Pl: 3.66 eV (I: 1440 cps)		
2682	16.11.2016	14CO-050	30 nm AlN, 30 s GaN QDs, 30 nm AlN	Pl: 3.59 eV		
2688	24.11.2016	14CO-050	30 nm AlN, 15 s GaN QDs, 30 nm AlN	Pl: 2.53 eV		
2689	24.11.2016	14CO-050	30 nm AlN, 15 s GaN QDs, 30 nm AlN	Pl: no signal		
2702	15.12.2016	14CO-050	Stacked QDs: 20x GaN QDs 20s, 30 nm AlN buffer, 4 nm AlN spacer, 30 nm AlN top	Pl: 3.83 Ev		
2705	22.12.2016	14CO-050	Stacked QDs: 2x GaN QDs 20s, 18 nm AlN buffer, 4 nm AlN spacer, 18 nm AlN top	Pl: 3.79 Ev		
2711	19.01.2017	14CO-050	Coupled ADQDs: 30 nm AlN buffer, 2 nm AlN spacer, 30 nm AlN top, 20 s+40 s GaN QDs	Pl: 3.69 eV		
2713	25.01.2017	14CO-050	Uncoupled ADQDs: 30 nm AlN buffer, 30 nm AlN spacer, 30 nm AlN top, 20 s+40 s GaN QDs	Pl: 3.51 Ev		
2717	01.02.2017	14CO-050	Uncoupled ADQDs: 30 nm AlN buffer, 30 nm	Pl: 3.53 eV		

			AlN spacer, 30 nm AlN top, 13 s+40 s GaN QDs			
2719	08.02.2017	14CO-050	Uncoupled ADQDs: 30 nm AlN buffer, 30 nm AlN spacer, 30 nm AlN top, 13 s+40 s GaN QDs	Pl: 3.57 eV, 3.29 eV		
2725	21.02.2017	14CO-050	30 nm AlN, 13 s GaN QDs, 30 nm AlN	Pl: 3.66 eV		
2726	22.02.2017	14CO-050	30 nm AlN, 13 s uncapped GaN QDs	AFM		
2737	05.04.2017	14CO-050	15 nm AlN, 25 s uncapped GaN QDs	AFM		
2738	05.04.2017	14CO-050	30 nm AlN, 17 s GaN QDs, 30 nm AlN	Pl: 2.75 eV		
2739	06.04.2017	14CO-050	42 nm AlN, 25 s GaN QDs, 42 nm AlN	Pl: 2.7 eV		
2740	07.04.2017	14CO-050	30 nm AlN, 25 s GaN QDs, 30 nm AlN	Pl: 4.0 eV		
2747	02.05.2017	14CO-050	30 nm AlN, 40 s GaN QDs, 30 nm AlN	Pl: no signal		
2750	08.05.2017	14CO-050	30 nm AlN, 13 s GaN QDs, 30 nm AlN	Pl: no signal		First 3 nm: AlGaN
2751	09.05.2017	14CO-050	30 nm AlN, 35 s GaN QDs, 30 nm AlN			
2754	13.06.2017	14CO-050	10 nm AlN			Test
2755	13.06.2017	14CO-050	10 nm AlN			Test
2757	20.06.2017	14CO-050	10 nm AlN			Test
2758	20.06.2017	14CO-050	25 nm AlN, 35 s GaN QDs, 25 nm AlN			Test
2761	27.06.2017	14CO-050	25 nm AlN, 35 s GaN QDs, 25 nm AlN	Pl: no signal		Test
2762	27.06.2017	14CO-050	17.4 nm AlN, 35 s GaN QDs, 27.8 nm AlN	Pl: 3.66 eV (I:1935 cps)		
2763	28.06.2017	14CO-050	20 nm AlN, 17s uncapped GaN QDs	AFM		
2767	05.07.2017	11CO-194	120 nm GaN			MA Rebeccah
2771	17.07.2017	11CO-194	159 nm GaN			MA Rebeccah
2776	28.08.2017	14CO-050	5 nm AlN			Test

2777	29.08.2017	14CO-050	15 nm AlN			Test
2778	30.08.2017	14CO-050	160 nm GaN			Test
2779		11CO-194	200 nm GaN			MA Rebeccah
2780	04.09.2017	11CO-194	200 nm GaN			MA Rebeccah
2782	15.09.2017	14CO-050	20 nm AlN			Test
2783	19.09.2017	11CO-194	400 nm GaN			MA Rebeccah
2784	21.09.2017	11CO-194	1µm GaN			MA Rebeccah
2785	25.09.2017	11CO-194	380 nm GaN			MA Rebeccah
2786	26.09.2017	11CO-194	600 nm GaN			MA Rebeccah
2787	27.09.2017	11CO-194	600 nm GaN			MA Rebeccah
2790	24.10.2017	14CO-050	20 nm AlN			Test
2809	10.01.2018	16CO-174	20 nm AlN, 25 s GaN QDs, 20 nm AlN			

10 List of Publications

(1) R. Koester, D. Sager, W.-A. Quitsch, O. Pfingsten, A. Poloczek, S. Blumenthal, G. Keller, W. Prost, G. Bacher, F.-J. Tegude, *High-Speed GaN/GaInN nanowire array LED on Silicon (111),* Nano Lett. **15**, 2318-2323 (2014).

(2) S. Sergent, S. Kako, M. Bürger, S. Blumenthal, S. Iwamoto, D.J. As, Y. Arakawa, *Active zinc-blende III-nitride photonic structures on silicon,* App. Phys. Express **9**, 012002 (2016).

(3) S. Blumenthal, M. Bürger, A. Hildebrandt, J. Förstner, N. Weber, C. Meier, D. Reuter, D.J. As, *Fabrication and characterization of two-dimensional cubic AlN photonic crystal membranes containing zincblende GaN quantum dots*, Phys. Stat. Sol. (c) **13**, 292 (2016).

(4) C. Rothfuchs, N. Kukharchyk, T. Koppe, F. Semond, S. Blumenthal, H.-W. Becker, D.J. As, H.C. Hofsäss, A.D. Wieck, A. Ludwig, *Photoluminescence of gallium ion irradiated hexagonal and cubic GaN quantum dots*, Nuclear Instruments and Methods in Physics Research B **383**, 1-5 (2016).

(5) S. Blumenthal, T. Rieger, D. Meertens, A. Pawlis, D. Reuter, D.J. As, *Stacked self-assembled cubic GaN quantum dots grown by molecular beam epitaxy,* Phys. Stat. Sol. (b) **255**, 1600729 (2018).

(6) S. Blumenthal, D. Reuter, D. J. As, *Optical properties of cubic GaN quantum dots grown by molecular beam epitaxy,* Phys. Stat. Sol. (b) **255**, 1700457 (2018).

11 Conference Contributions

12/2011	Participant, Winterschool for Nanomaterials, Duisburg (Germany)
06/2012	Participant, Photovoltaik-Tag NRW, Duisburg (Germany)
12/2013	Oral presentation, 28th Workshop of DGKK: Epitaxy of semiconductors, Ilmenau (Germany)
11/2014	Participant, 1st international workshop SFB/TRR 142, Bad Sassendorf (Germany)
12/2014	Poster presentation, 11th GRK Convention, Paderborn (Germany)
03/2015	Oral presentation, Frühjahrstagung der Deutschen Physikalischen Gesellschaft (DPG), Berlin (Germany)
04/2015	Poster presentation, 4th Europhotonics Spring School 2015, Paderborn (Germany)
05/2015	Participant, 2nd international workshop SFB/TRR142, Bad Sassendorf (Germany)
08/2015	Oral presentation, ICNS-11, Beijing (China)
09/2015	Participant, DMBE, Paderborn (Germany)
11/2015	Oral presentation, 13th GRK Convention, Paderborn (Germany)
11/2015	Participant, 3rd international workshop for Masterstudents, PhDs and Postdocs SFB/TRR 142, Dortmund (Germany)
03/2016	Oral presentation, Frühjahrstagung der Deutschen Physikalischen Gesellschaft (DPG), Regensburg (Germany)
04/2016	Poster presentation, 5th Europhotonics Spring School 2016, Porquerolles (Germany)
10/2016	Oral presentation, International Workshop on Nitride Semiconductors (IWN) 2016, Orlando, Florida (USA)
12/2016	Oral presentation, 31th Workshop of DGKK: Epitaxy of semiconductors, Duisburg (Germany)
03/2017	Poster presentation, 6th Europhotonics Spring School 2017, Sitges (Spain)
07/2017	Poster presentation, ICNS-12, Strasbourg (France)
12/2017	Oral presentation, 23th Workshop of DGKK: Epitaxy of semiconductors, Freiburg im Breisgau (Germany)

Invited Talks

03/2014	Oral presentation, University of Bochum, Group meeting of AG Professor Dr. Andreas D. Wieck
07/2016	Oral presentation, TU Berlin, Group seminar of AG Professor Dr. Axel Hoffmann

12 Cooperation Partners

- Ernst Ruska-Centre for Microscopy and Spectroscopy with Electrons, Forschungszentrum Jülich
- Otto-von-Guericke University Magdeburg, Institute of Experimental Physics, Group of Prof. Dr. Jürgen Christen
- Technical University Berlin, Institute of Solid State Physics, Group of Prof. Dr. Axel Hoffmann
- Universität Paderborn, Department of Physics, Group of. Prof. Dr. Cedrik Meier
- Universität Paderborn, Department of Theoretical Electrical Engineering, Prof. Dr. Jens Förstner

13 Acknowledgment

I would like to take this opportunity to thank everyone who supported and accompanied me during my dissertation. Special thanks go to:

- apl. Prof. Dr. Donat J. As for the support and the possibility to realize this interesting work. His experience, his commitment and the many helpful discussions have helped me a lot on my way to this work.
- Prof. Dr. Cedrik Meier for his work as second assessor and for the access to electron-beam lithography, plasma etching and photoluminescence spectroscopy.

- Prof Dr. Dirk Reuter for many scientific discussions and support.
- Dr. Andre Hildebrandt for the numerical simulations.
- Anja Blank, Siegfried Igges for administrative and technical support.

- My office mates Dr. Matthias Bürger and Dr. Tobias Wecker for the pleasant atmosphere and the great teamwork.
- My other colleagues Michael Deppe, Alexander Trapp, Viktoryia Zolatanosha, Stepan Shvarkov, Nandlal Sharma and all members of our group meetings for their teamwork, support and relaxed working atmosphere.
- The colleagues of GRK 1464 especially Christian Schlickriede, Michael Rüsing, Christoph Eigner, Thomas Hett, Nils Weber, Christoph Brodehl, Joachim Vollbrecht and Dominik Breddermann for many critical questions, good discussions and nice evenings.

- I would especially like to thank my family and friends from home for their support and encouragement.
- And last but not least I would like to thank Markus for his love, understanding and support in my life.

14 Erklärung der Selbstständigkeit

Hiermit versichere ich die vorliegende Arbeit selbstständig verfasst und keine anderen als die angegebenen Quellen und Hilfsmittel verwendet, sowie Zitate deutlich kenntlich gemacht zu haben.

Paderborn, den ______________________________

Sarah Blumenthal